Politecnico di Torino

M.Sc. Environmental and Land Engineering Climate Change
Graduation Session October 2024

Managed Aquifer Recharge for sustainable groundwater use in the Cuneo Plain

From data analysis to numerical modelling

Supervisors:

    Prof. Tiziana TOSCO
    Prof. Rajandrea SETHI
    Prof. Alessandro CASASSO

Candidate:

    Alessia AMENDOLA

Abstract

The Cuneo Plain (Piedmont, NW Italy), like all the Po Plain, is characterized by intense agricultural activities that heavily rely on seasonal water availability, which is now challenged by the climate crisis. In particular, the increased vulnerability to frequent drought emergencies is demonstrated by losses in agricultural yields. Consequently, groundwater resources have been a great tool to buffer temporary water scarcity and mitigate the drought risk. Groundwater irrigation, however, can prove to be a maladaptation practice if local aquifers are overexploited. For this reason, the assessment of the groundwater stress in the Cuneo Plain was carried out with innovative methodologies. As a result, a significant depletion was recognized, therefore, Managed Aquifer Recharge (MAR) is presented as possible solution, as it allows to convey into the subsoil, during winter times, the water in excess coming from the surrounding streams and recover it downstream through the historical drainage trenches present on site, known as *fontanili*, during summertime, when the irrigation demand peaks.

The objective of this work is that of estimating the temporal anomaly of the saturated thickness, by means of satellite measurements of gravimetric anomalies (from GRACE Missions) combined with hydrological models (GLDAS), as well as modelling the agricultural drainage trenches and evaluating the possible benefits coming from pilot MAR sites. This innovative practice is gaining a foothold in those territories highly vulnerable to drought risk, as is allows to store a significant amount of water underground, for its use during the periods of the year characterized by higher stress and irrigation demand. In order to evaluate the advantages of this solution, numerical modelling has been exploited to understand the connections between a drainage trench and a MAR site with the unconfined aquifer system. On one hand, the *fontanili* were constructed starting from the XI century with the aim of reclaiming swamps through the lowering of the water table and to provide water for irrigation and drinking purposes. Nowadays, they still own a central role in the supply of irrigation water to the vast agricultural lands. By means of a conceptual model, the relationship between the depth to groundwater and their discharge was established, as well as the contribution of a peculiar configuration including screened boreholes, known as *tubi calandra*, along the furrows. On the other hand, a pilot MAR site is being planned in the town of Tetti Pesio (CN), a few hundred meters upstream the *fontanili*. Therefore, the simulation was expanded to evaluate the effect of MAR on the water table and on the discharge of the *fontanili* located downstream.

This work of thesis is part of the *SeTe* project, funded by the European Union cross-border cooperation program *Interreg ALCOTRA*, which aims at mitigating the drought risk by means of "sustainable blue infrastructures".

Table of Contents

List of Figures

6

List of Tables

1 Introduction

This work of thesis focuses of the sustainable management of groundwater resources for agricultural applications. The attention is set on the assessment of the current water stress and on numerical modelling as a tool to evaluate the benefits of a technologically improved water network, able to satisfy the irrigation water demand also in periods of limited availability of this resource. As a matter of fact, the Province of Cuneo, is characterized by intense agricultural and zootechnical activities that are rooted in the economic and cultural heritage of the area. In particular, many businesses rely on the seasonal water availability, which is nowadays being challenged by the changing climate. Indeed, the water precipitated in the surrounding valleys turns into runoff and is conveyed, by means of several temporary streams, to the main plain, crossed by the river Stura di Demonte. Here, a vast network of channels, managed by the local irrigation consortia, distributes the water around the agricultural fields. Despite this, the climate-induced alteration of the precipitation pattern is exposing the agricultural sector to higher drought risk. Consequently, to buffer the lack of the resource, part of the water supply now relies onto the groundwater system, adding a higher anthropic pressure on the shallow unconfined aquifer and exposing it to possible overexploitation. Hence, the reason to investigate the state of groundwater resources in the area and propose modern practices for their sustainable management.

Firstly, the work will provide a general assessment of the state of water resources, and their connection to agriculture, in the Mediterranean area, based on the local monitoring agencies and the up-to-date research carried out by the Intergovernmental Panel on Climate Change. Furthermore, the spatial scale will be reduced up to the Cuneo Plain to analyze the temporal evolution of the saturated thickness in the period 2003-2023. More in detail, the GRACE and GRACE-FO satellite missions, conducted by NASA starting from 2002, were planned to investigate the Earth's gravitational field and analyze its evolution in terms of mass distribution, which is connected mainly to the movement of water across the globe. These measurements of gravimetric anomalies, made available as estimates of the Water Equivalent Thickness (WET), can be combined with hydrological models, such as GLDAS, to retrieve the groundwater storage anomaly (GWSA) and identify drought periods. On this topic, a step-by-step guideline will be developed.

Secondly, a deeper analysis of the hydrogeological context of the area will be presented, as well as the peculiar configuration of the historical drainage channels, known as *fontanili*. They are a network of ponds and furrows where the groundwater naturally resurfaces. They were constructed starting from the XI century to reclaim the swamps and convey water to the agricultural fields, and they still hold, nowadays, a key role in the distribution of irrigation water. By means of numerical modelling, their connection to the depth to groundwater will be studied under different scenarios. Moreover, Manager Aquifer Recharge (MAR) will be proposed as a blue infrastructure allowing to stock water during winter times and recover it through the *fontanili* downstream, during summertime. As a matter of fact, a pilot site is being planned in Tetti Pesio (in the municipality of Cuneo) to virtually transpose water availability from seasons of abundance to those characterized by scarcity and, simultaneously, higher demand, thus, enhancing the resilience of the territory to drought events. Also in this case, numerical

modelling will serve as the tool to evaluate the effects of the injection onto the shallow unconfined aquifer and its contribution to the groundwater feeding the *fontanili*.

The topic of the thesis is inspired by the *SeTe* project, which aims at mitigating the drought risk by means of blue infrastructures and nature-based solutions. This is involved into the European program *Interreg ALCOTRA: Alpi Latine Cooperazione TRAnsfrontaliera*, which consists in an active international cooperation, in this case between Italy and France, to overcome environmental, social and economic challenges

2 Case study

2.1 The study area

The Monregalese is part of the Province of Cuneo, which lies within Piemonte Region, in north-western Italy. The study area is characterized by a vast flood plain (about 3000 km^2), originated from a series of overlapped alluvial fans from the Quaternary activity of rivers draining the Alps. These deposits have a variable thickness that is overall greater, up to 100 m, in the foothills of the mountains and they get to just a few meters in thickness in the plain. They hold several unconfined aquifers that are not hydrodynamically connected with one another, due to the deep fluvial incisions that reach the Tertiary series that is found underneath. The depth to groundwater ranges from 60 m in the foothills to just a few meters in the plain, where several natural springs are found as well. In general the sediments have high porosity, as well as permeability, and the water availability is generous (Ansaldi & Maffeo, 1979). Therefore, these aquifers are usually very productive, guaranteeing a reliable source of water for the agricultural and livestock activities in the area (Civita et al., 2011). As a matter of fact, groundwater in Piemonte has a central role: it supplies 85% of the drinking water in the region, it feeds multiple river networks and is exploited by many industrial and agricultural activities (Lasagna et al., 2020).

The main plain covers an area of about 1790 km^2 and is surrounded by the Langhe-Roero hills in the NE direction, by the mountains, at the borders with Liguria and France, and it is connected to the plain of the Province of Torino in the North. The plain was generated from the sandy and loamy alluvial depositions of the multiple streams that drained the Alps. The area is geomorphologically divided in two portions, separated by the river Stura di Demonte, a tributary of the Tanaro river. The Quaternary succession comes to surface over the entire main plain, both on the right and on the left side of the Stura di Demonte, but some tectonic factors influenced the stratigraphy, enhancing its complexity. Consequently, portions of the stratigraphy appear to be partly eroded, but still the layers are recognizable by their altitude and granulometry. The stratigraphy is divided, from a geological point of view, into three alluvial units (see Figure 1, modified from (Civita et al., 2011)):

i.   Alluvial Unit of Conoids and Terraces: high terraces come to surface close to the Alps (e.g. in the area of Beinette) and the material is part of the Pleistocene deposits. The unit is composed of heterogeneous gravel in a silty-clayey matrix. Close to the foothills the pebbles show a diameter up to 1 m large, but the granulometry gets smaller the further one goes from the mountains. The terraces are connected to the plain through sharp slopes, from 5 to 30 m in elevation.

ii. Alluvial Unit of the Fundamental Level of the Plain: the unit comes to surface in the whole area of the plain, on both sides of the Stura di Demonte, until the confluence with the Tanaro river. The plain originated from the vast conoids of the water streams present in the area: Stura, Gesso, Pesio, Grana, Maira, Varaita and Tanaro. The granulometry is composed of coarse gravel, with a diameter up to 20-30 cm, immersed in a sandy-silty matrix. Most of the unit lies above the Plio-Pleistocene Succession.

iii. Alluvial Unit of the Valley Floors: this unit comes to surface over the slopes and valley floors of the streams Stura di Demonte, Gesso and Pesio. These deposits are the result of the deepening of the river network and of a small deposition, due to the diversion of the Tanaro river. The granulometry is made of coarse gravel in a sandy matrix.

In the Province of Cuneo three main hydrogeological series have been identified. The study area of this work is located in the hydrogeological Quaternary series, which characterizes most of the plain. This series hosts many unconfined aquifers, that provide the main source of water for drinking and irrigation purposes. The series is made of three main complexes (Figure 2, modified from (Civita et al., 2011)), from the oldest to the most recent:

i. Alluvial Complex of the Ancient Gravels: it consists of the conoids located at the foothills and of the isolated highlands. The thickness of the complex is always in the order of 10 m and the permeability is intermediate. Usually, impermeable silty-clayey layers, of about 2 to 4 m in thickness, are found above the coarse gravel immersed in a silty matrix. Shallow and isolated unconfined aquifers can be found at some of the borders of the terraces, their only source of recharge is precipitation or, occasionally, water drainage from irrigation. For these reasons, not many wells are active in these areas.

ii. Main Alluvial Complex: the thickness of the complex ranges from 80 to 90 m in the foothills to just a few meters in the eastern part, at the boundary with the Langhe and Roero Hills. The permeability is high, but there are sparse locations where the sediments are more cemented, such as in Borgo San Dalmazzo. The complex hosts many unconfined aquifers, recharged by precipitation and losses from the river network. During the dry seasons, winter and summer, the streams dry out completely in the alpine segment, although some water is present once they reach the plain due to the hydrodynamic connection to groundwater. On the left side of Stura di Demonte one wide unconfined aquifer is present, whereas, on the right side the incisions of the multiple streams led to the creation of several small and isolated unconfined aquifers. Over the plain multiple natural springs come to surface. Starting from the XI century, in these areas, an artificial drainage network was realized using trenches, called "*Fontanili*". This allowed to remediate large parts of the plain which were subject to flooding, due to the shallow piezometry. The water drained from the springs is used as a source for irrigation (GEAM, 2000). Here the abstractions for drinking purposes must undergo purification due to the scarce quality of the water. More in detail, the area surrounding Morozzo is the widest homogeneous area in the right side of the Stura di Demonte as it covers 211 km^2. The boundaries of the area are the Alps, the highlands and the streams Stura di Demonte and Pesio. The thickness of the superficial groundwater body ranges from 90 m, close to Borgo San Dalmazzo, to 10-20 m in the plain, except for the areas close to valley floors, here the thickness reaches 5 m. The stream Gesso strongly recharges the aquifer close to Borgo San Dalmazzo. Other than that, the recharge is attributed to precipitation, losses in the irrigation network and drainage from flooding irrigation during summer. Wherever the piezometry intercepts the ground level, multiple springs are found, for this reason most of the drainage trenches are located here, as it can be seen from Figure 2.

iii.   Alluvial Complex of the Valley Floors: this complex comes to surface just in the areas surrounding the water flows. Along the stream Stura di Demonte and its tributaries. It is composed of coarse gravel in a sandy matrix, therefore, it is characterized by high permeability and the thickness of the aquifer is very low.

The piezometric map of the study area is reported in Figure 3, modified from (Civita et al., 2011). The hydraulic gradients range from 27‰ in the foothills to 5‰ close to Beinette. The depth to groundwater ranges from 30 m to less than 5 m and the water flow is directed along with the Stura di Demonte valley. In the site of Morozzo, the groundwater flow direction is overall from South-West to North-East, but, other than the Stura di Demonte, another creek is present, called Brobbio, which flows almost parallel to the Stura di Demonte. From the piezometric map, it is evident that the equipotential lines of hydraulic head are tilted towards the two rivers, meaning that the groundwater is feeding them(Sethi & Di Molfetta, 2019). In Bene Vagienna the presence of the highlands strongly influences the flow direction and the piezometric map. Here the thickness of the aquifer is very small, same for the depth to groundwater and, in general, for the water availability. The main groundwater withdrawals are due to the fed streams, the springs with their drainage trenches and the artificial wells.

Figure 1. From "Carta delle Successioni Geologico-stratigrafiche"(Civita et al., 2011)

Figure 2. From "Carta della Serie Idrologica Quaternaria"(Civita et al., 2011)

Figure 3. From "Carta del Campo di Moto dell'Acquifero Libero" (Civita et al., 2011)

"LE ACQUE SOTTERANEE DELLA PIANURA E DELLA COLLINA CUNEESE"

CARTA DEL CAMPO DI MOTO DELL'ACQUIFERO LIBERO
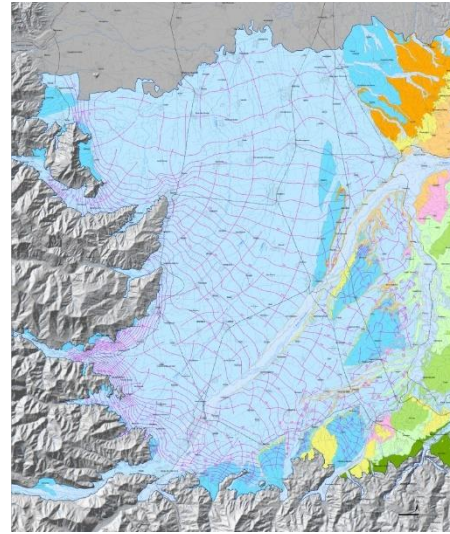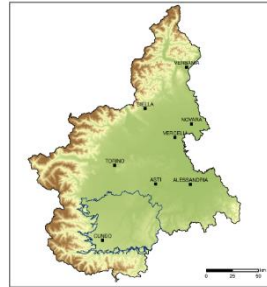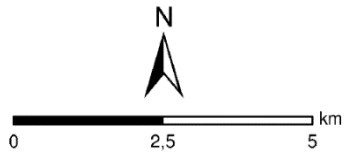
LEGENDA

Serie idrogeologica Quaternaria
- Complesso Alluvionale dei fondovalle e dei terrazzi annessi
- Complesso Alluvionale principale
- Complesso Alluvionale delle Ghiaie antiche

Serie idrogeologica Plio-Pleistocenica
- Complesso delle Alternanze
- Complesso delle Ghiaie alterate, delle Ghiaie sabbiose e delle Sabbie
- Complesso Argilloso-Sabbioso

Serie idrogeologica Oligo-Miocenica
- Complesso Argilloso-Ghiaioso-Gessoso
- Complesso Arenaceo-Marnoso
- Complesso Argilloso-Marnoso
- Complesso Arenaceo-Conglomeratico

- Curve isopiezometriche
- Linee di flusso
- Area di studio
- Aree edificate
- Strade
- Autostrade
- Ferrovie
- Idrografia

16
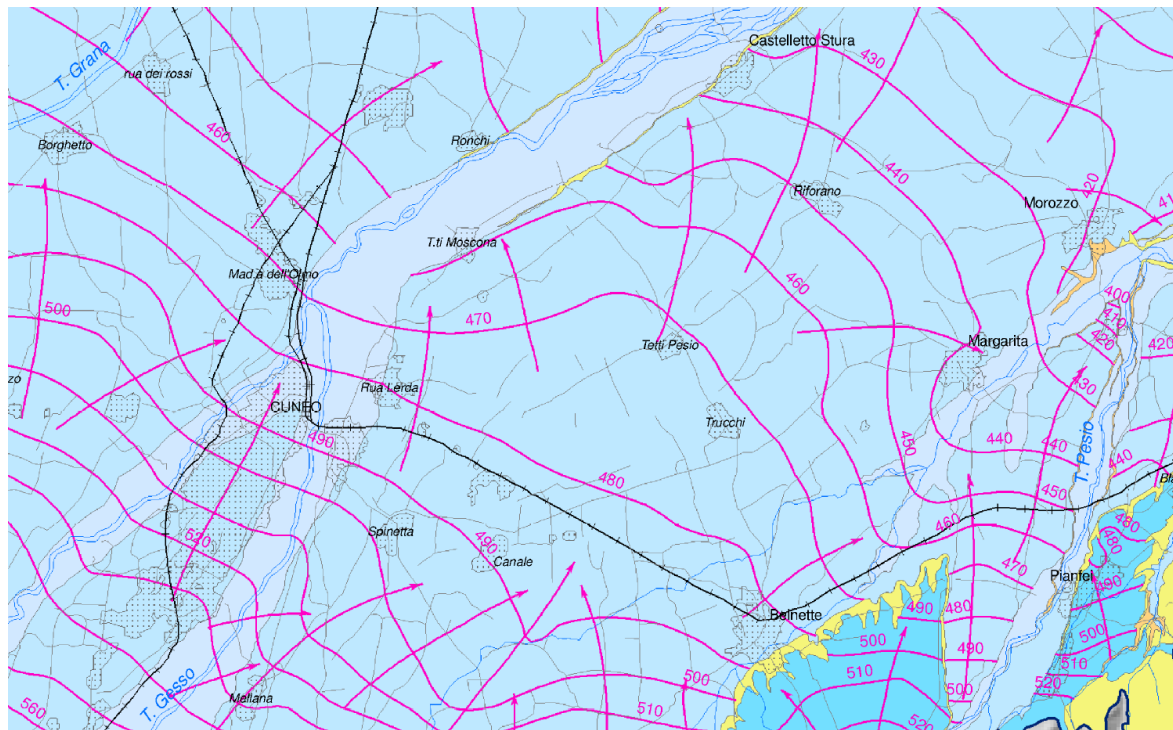
As far as the chemical status is concerned, the groundwater has high electrical conductivity and hardness, due to the long paths within the formations (Civita et al., 2011). But the high permeability, that characterizes most deposits, increases the vulnerability to contamination, especially in those cases where deep aquifers are not protected by an impermeable capping, or they are hydrodynamically connected to the unconfined ones (Ansaldi & Maffeo, 1979). Indeed, a first preliminary analysis (following D.Lgs. 152/99) is conducted using only the basic monitoring parameters: conductivity [mS/cm], chlorides [mg/l], nitrates [mg/l], sulphates [mg/l], ammonium ion [mg/l], iron [mg/l], manganese [mg/l]. Based on the observations for these parameters (Table 1, from (Civita et al., 2011)), the area is divided into quality classes:

a) Anthropic impact is none or negligible;
b) Small anthropic impact and good hydro-chemical properties;
c) Significative anthropic impact and good hydro-chemical properties, but with evidence of deterioration;
d) Important anthropic impact and bad hydro-chemical properties.

Consequently, Beinette is classified as *(d)* due to ammonium ion contamination from livestock activities; Bene Vagienna is, again, class *(d)* due to the high concentrations of Manganese; instead, Morozzo belongs to class *(c)* since its parameters are slightly better (Civita et al., 2011).

Table 1. Observation of chemical parameters in Beinette, Morozzo and Bene Vagienna, according to D.Lgs. 152/99. Source: (Civita et al., 2011)

Chemical Parameter	Beinette	Morozzo	Bene Vagienna
pH	7.91	6.93	6.98
EC 20°C [µS/cm]	439.83	364.75	983.75
TH [°f]	20.62	16.33	41.74
Ca^{2+} [mg/l]	49.74	50.55	91.82
Mg^{2+} [mg/l]	19.90	9.01	45.64
Na^+ [mg/l]	9.65	9.83	43.55
K^+ [mg/l]	13.90	4.73	45.58
Cl^- [mg/l]	20.37	8.80	46.30
SO_4^{2-} [mg/l]	44.67	32.32	92.38
HCO_3^- [mg/l]	181.07	144.31	416.57
NO_3^- [mg/l]	24.85	30.82	71.92
NH_4^+ [mg/l]	0.75	0.07	0.03
Mn^{2+} [mg/l]	0.13	<0.01	0.16
Fe_{tot} [mg/l]	0.04	0.01	0.02

2.1.1 Hydrological analysis

To have a better understanding of the seasonal patterns of water availability in the area of interest, a hydrological analysis has been carried out. More in detail, several creeks have been involved to understand the spatiotemporal distribution of discharges, which are crucial for water availability for irrigation.

As highlighted in Figure 4, the study area is part of the Stura di Demonte water basin, which can be subdivided, at a deeper level, into three watersheds: Stura di Demonte itself, that of its tributary Gesso and that of the Pesio stream, a tributary of the Tanaro river. The regional agency for environmental protection (Arpa Piemonte) has made available timeseries of water level (m) and discharge (m^3/s) for several cross-sections around the area, refer to Figure 4. In particular, three were chosen for the Stura di Demonte (in Vinadio, Gaiola and Fossano) following the water course; two stations were considered for the Gesso watershed, one in Andonno and the other in Robilante, monitoring its tributary Vermenagna; finally, concerning the Pesio watershed, one station was taken into account, in San Bartolomeo and the other, monitoring the tributary Brobbio, in Margarita.
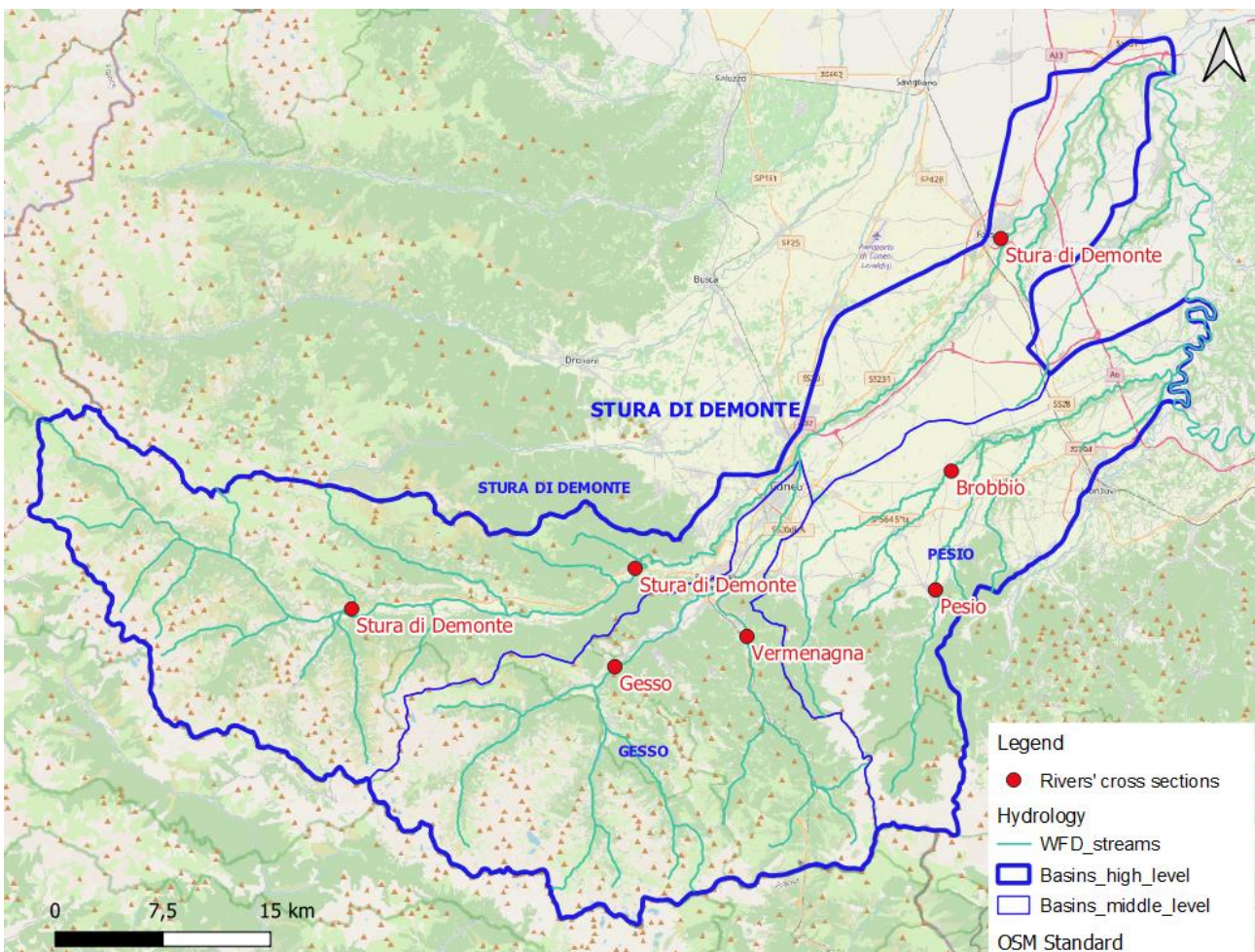
Figure 4. Hydrological map of the study area. In blue are the watersheds, the red dots represent the cross-sections where measurements were taken.

18

The timeseries of the discharges were averaged to obtain the mean monthly water volumes flowing through the cross-sections, see the boxplots of this variable over the years in the Figures below. The patterns obtained are perfectly reflected in the seasonality of the precipitation in Cuneo (Figure 12), as in both cases two peaks are present: one in spring and one during fall. Instead, the season interested by highest water demand for irrigation, summer, is characterized by lower surface water availability. From here, the concern for a reliable and alternative water source rises, as well as the interest in artificially modifying these patterns using Managed Aquifer Recharge (MAR).
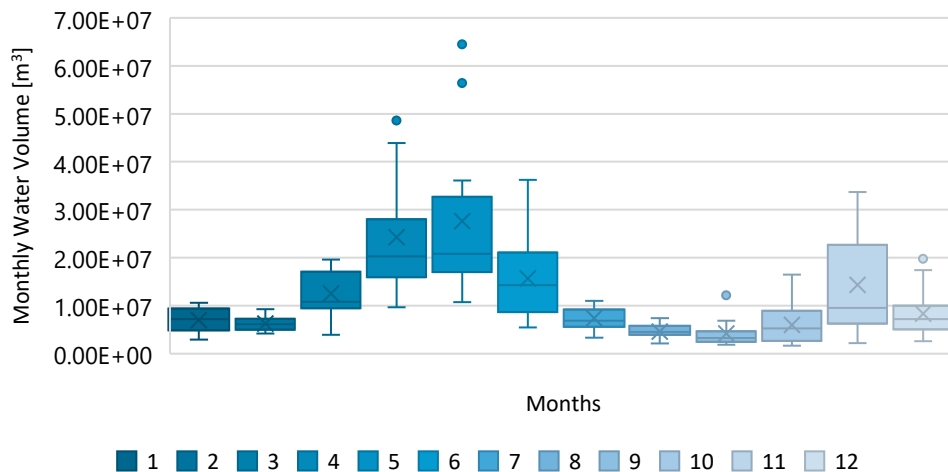
Figure 5. Gesso watershed – monthly water volume flowing at the cross-section in Robilante.
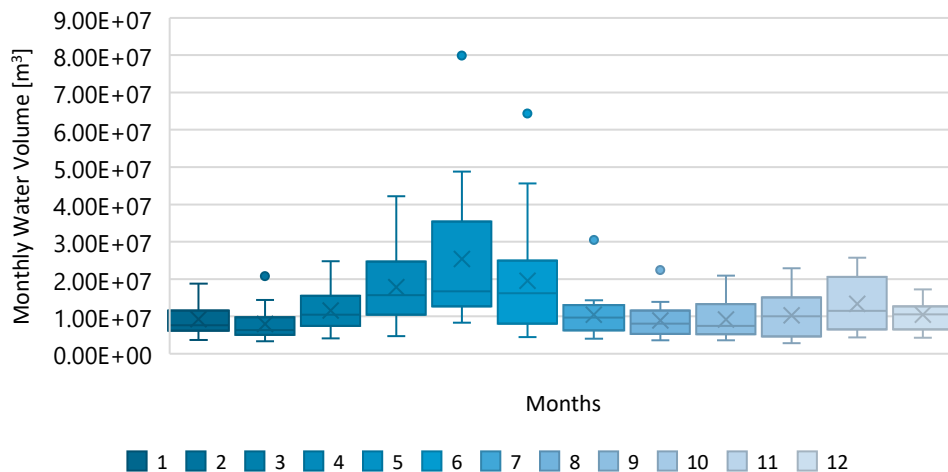
Figure 6. Gesso watershed – monthly water volume flowing at the cross-section in Andonno.
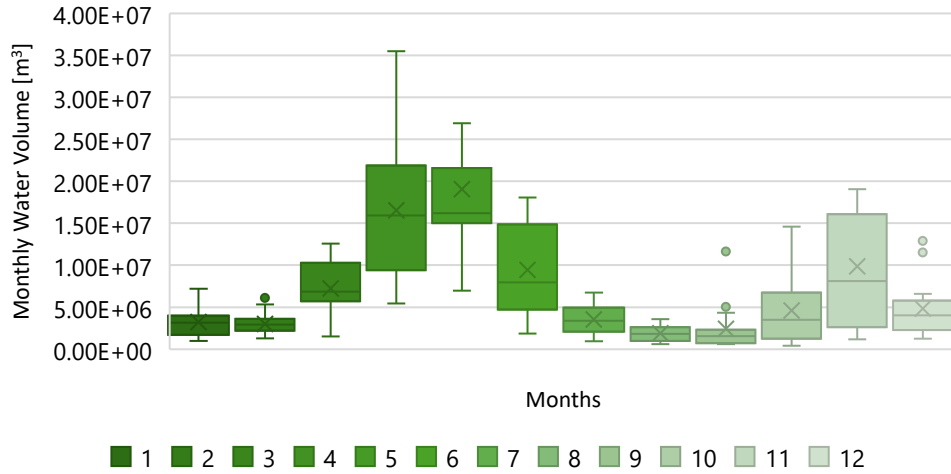
Figure 7. Pesio watershed - monthly water volume flowing at the cross-section in San Bartolomeo.
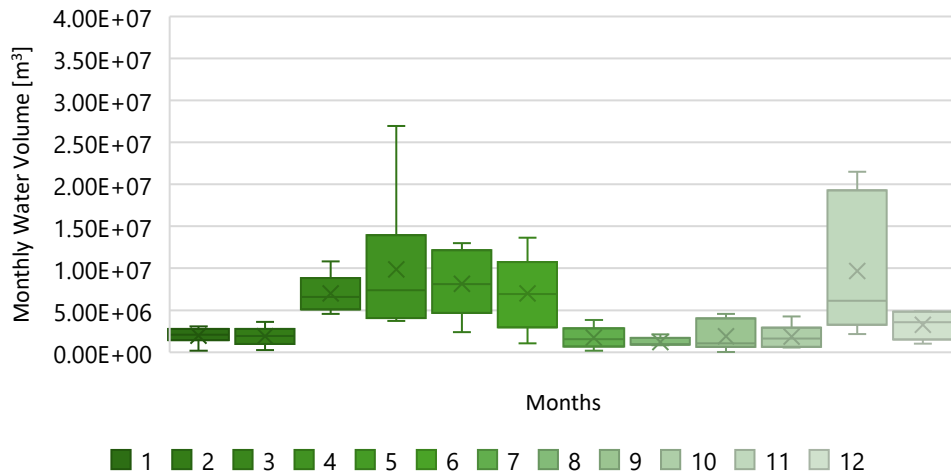
Figure 8. Pesio watershed - monthly water volume flowing at the cross-section in Margarita.
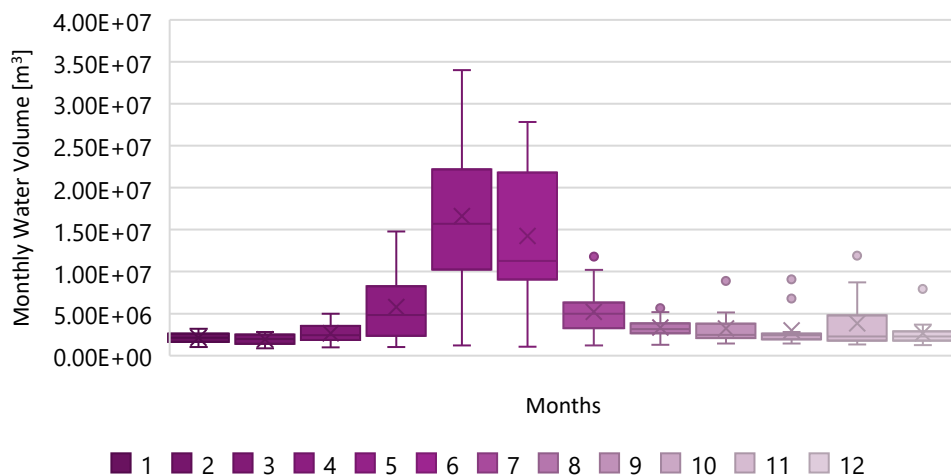
Figure 9. Stura di Demonte watershed - monthly water volume flowing at the cross-section in Vinadio.
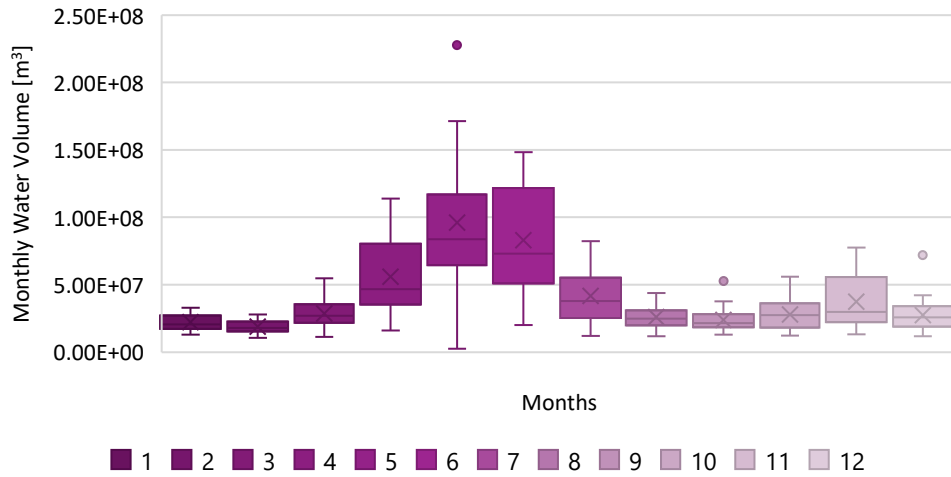
Figure 10. Stura di Demonte watershed - monthly water volume flowing at the cross-section in Gaiola.
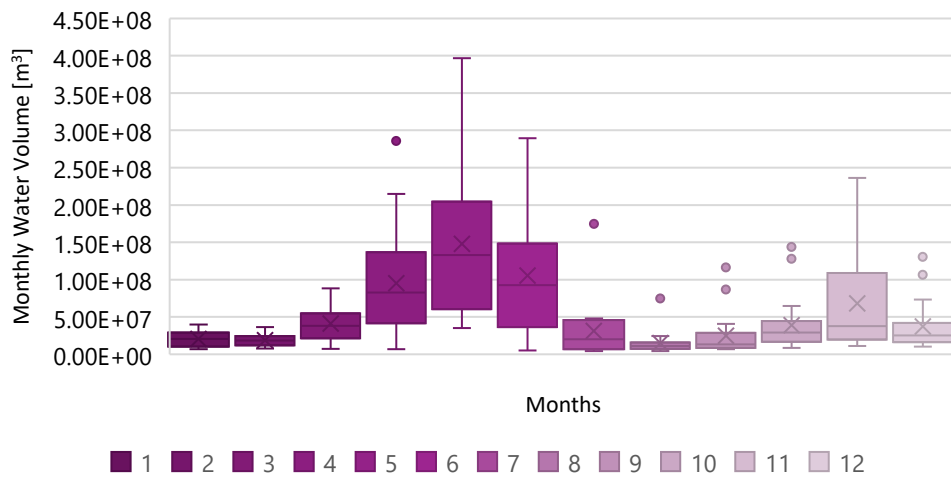
Figure 11. Stura di Demonte watershed - monthly water volume flowing at the cross-section in Fossano.
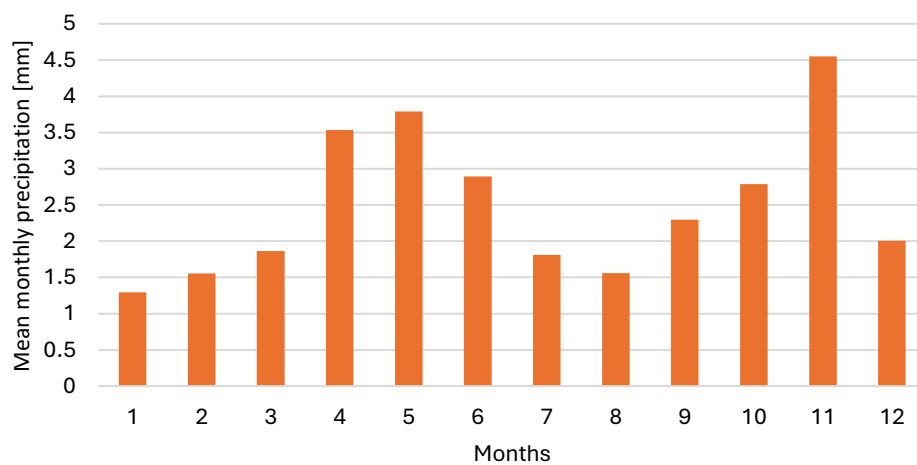
Figure 12. Mean monthly precipitation in Cuneo.

2.2 The SeTe - ALCOTRA project

As previously mentioned, the project connected to this work of thesis is *SeTe* – ALCOTRA and it involves several regions located along the Alpine border between Italy and France, from Haute-Savoie and Valle d'Aosta down to Les Alpes Maritimes and Liguria. The goal is to find shared solutions to environmental, social and economic challenges. In particular, *SeTe* aims at mitigating the drought risk and protect biodiversity, while providing support for the ecological transition, as wells as a coordinated management of the natural resources. The main actions to be developed are soil conservation, water harvesting systems and water stocking through nature-based solutions. The ultimate objective is to improve the resilience of the territory to droughts, water use competition, wildfires and biodiversity threats. On top of this, the re-established equilibrium in the aquifers will not only provide a reliable water source, but will also reduce the saltwater intrusion in coastal areas. Meanwhile, local communities and stakeholders will be involved, and the program will offer the chance to put in place pilot projects (*SeTe: Siccità e Territorio*, n.d.). For this reason, a further, and more local, investigation of the aquifer is presented below, see Figure 13.
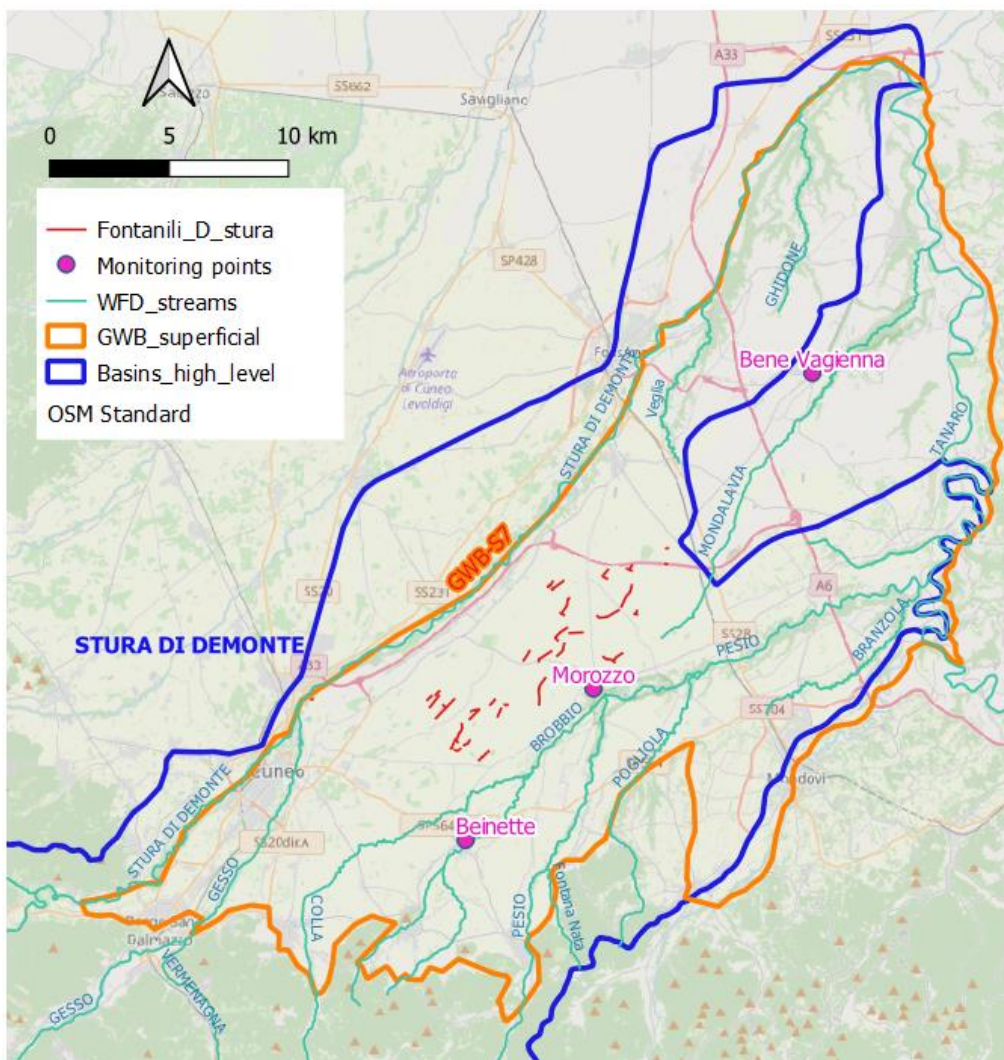
Figure 13. Groundwater basin in the study area (orange) along with its monitoring wells (purple). In red are represented the drainage trenches ("Fontanili").

The area of interest is located over the superficial unconfined aquifer GWB-S7, which is about 600 km² wide and, as stated previously, it feeds the water streams in the surroundings. For the monitoring activities three wells equipped with leveloggers and located along the main flow direction, South-West to North-East, were used: one in Beinette, close to the foothills, another in Morozzo and the last one in Bene Vagienna, where the thickness of the aquifer is the lowest. The leveloggers in Beinette and Morozzo are located respectively at 489 m a.s.l. and 429 m a.s.l., and are 30 m and 20 m deep (Civita et al., 2011). The timeseries of the depth to groundwater allows to evaluate the availability of the resource and its evolution. In the specific, for the case of Morozzo the variable is displayed together with the timeseries of precipitation collected by ARPA Piemonte at the meteorological station of Morozzo (44.41778 N 7.69222 E) at 440 m a.s.l.. Indeed, a direct relationship can be identified, as peak of meteorological events correspond to a sudden rise of the water table, as reported in the following Figure.
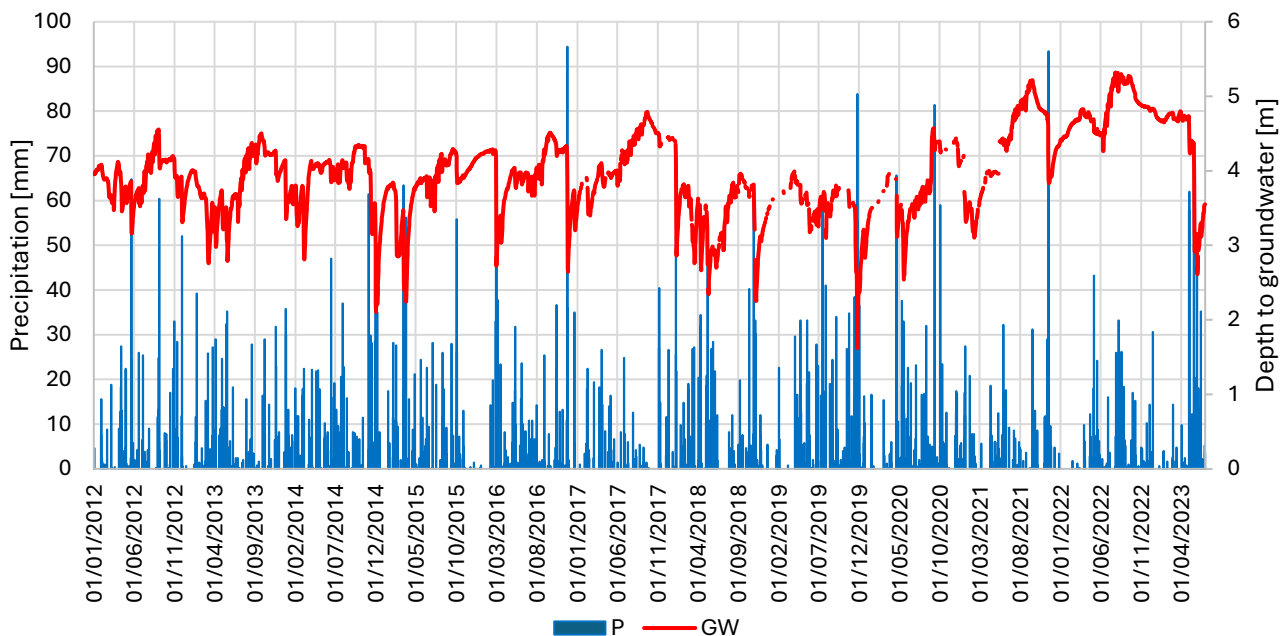
Figure 14. Precipitation and depth to GW in Morozzo (2012-2023), Source: ARPA Piemonte.

On the contrary, Figure 15 confirms that the depth to groundwater in Beinette doesn't show a direct response to the precipitation events. Instead, in Morozzo and Bene Vagienna a strict relationship is recognized in between the two variables. Moreover, the amplitude of the fluctuations in the depth to groundwater is more pronounced in the foothills (e.g. Beinette), whereas it gets smoother moving downstream the Stura di Demonte (e.g. Bene Vagienna) (Civita et al., 2011). Furthermore, in the municipality of Morozzo, the depth to groundwater is on average at about 4 m, but a significant increase can be noticed for the most recent years, especially 2022, when the water table was almost stable at 5 m below ground level. This confirms the strong connection of the aquifer to the meteorological events, as a matter of fact this year is remembered as a particularly dry one, see Figure 16 (Arpa Piemonte, 2023).
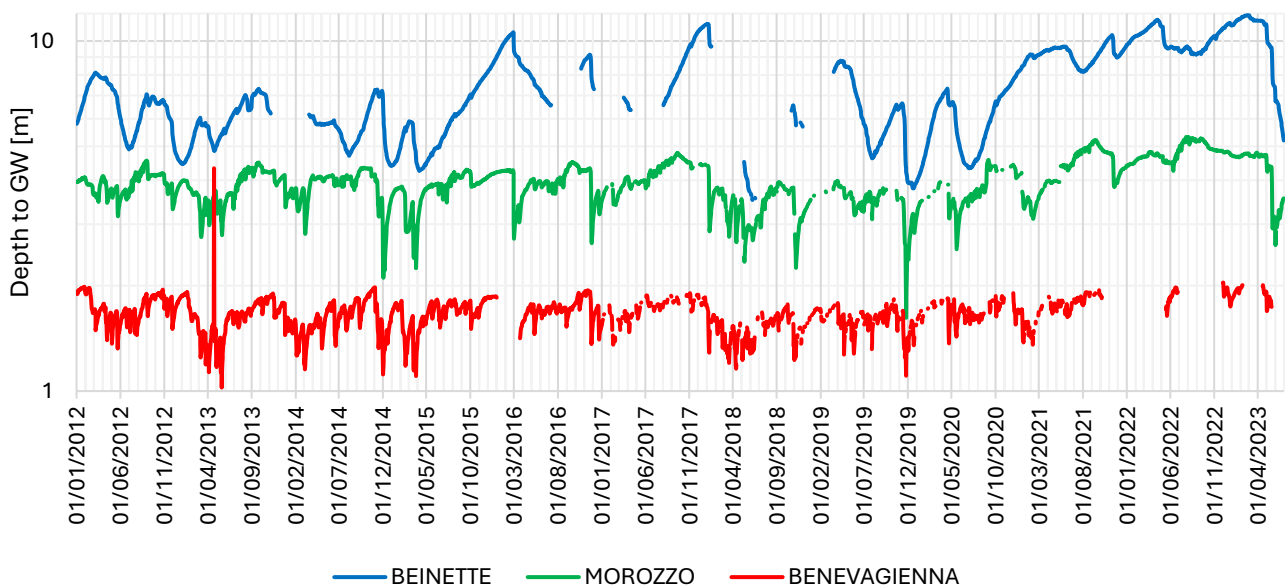
Figure 15. Depth to GW in Beinette, Morozzo and Bene Vagienna.
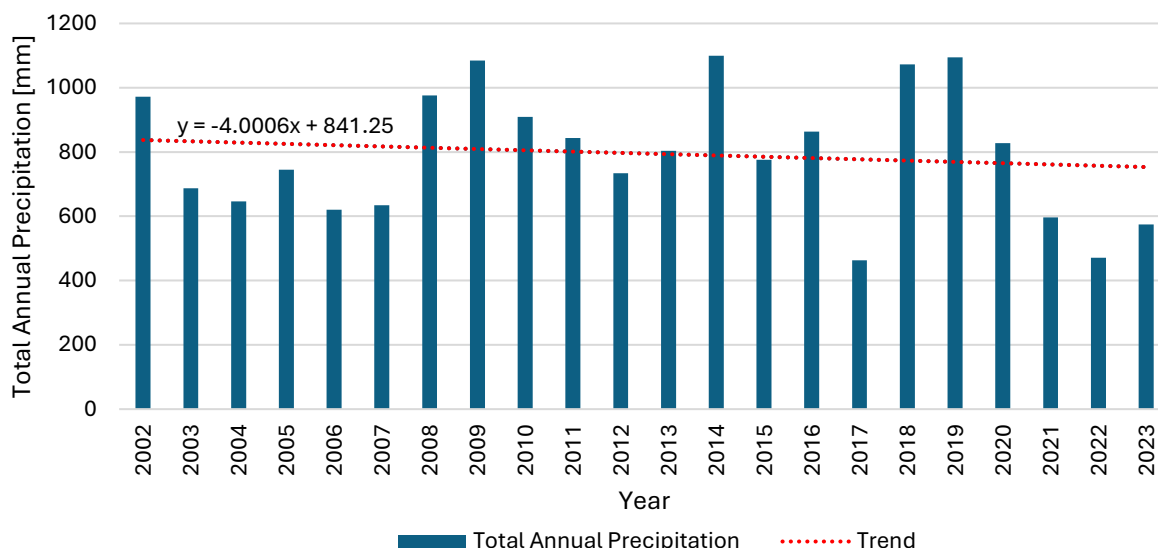
Figure 16. Total annual precipitation in Morozzo (2002-2023), Source: ARPA Piemonte.

Under this framework, three pilot MAR infrastructures are being planned: in Tetti Pesio, Beinette and Centallo. This work will focus only on the first location. Here, the project foresees several field campaigns to retrieve more detailed hydrogeological information, as well as the installation of new monitoring wells that will allow to perform aquifer tests in order to gain a deeper understanding of the working mechanisms of the *fontanili* located downstream, in the municipality of Morozzo. Moreover, the MAR site, located a few hundreds of meters upstream, will consist of an injection trench, made of a screened pipe, immersed in a layer of gravel. The goal is to perform several tests to evaluate the effects on the water table and on the discharge of the *fontanili*, before the installation of the other two sites.

3 Background and Methodology

3.1 Assessment of the current water stress

The United Nations (UN) define water security as "*the capacity of a population to safeguard sustainable access to adequate quantities of acceptable quality water for sustaining livelihoods, human well-being, and socio-economic development, for ensuring protection against water-borne pollution and water-related disasters, and for preserving ecosystems in a climate of peace and political stability*" (UN-Water, 2013).

3.1.1 The global scale

At the current state, water security is not guaranteed all over the world due to both climatic and anthropogenic drivers: the UN estimate that nowadays 2.2 billion people still do not have access to safely managed drinking water (UNESCO & Koncagül, Engin , Connor, Richard , Abete, 2024). Besides, the IPCC states that human-induced climate change is enhancing the likelihood and the severity of drought events in many regions around the world. As a matter of fact, under RCP 6.0 and SSP2 it is forecasted that the population exposed to extreme-to-exceptional Total Water Storage (TWS) drought will grow from 3% to 8% over the XXI century (IPCC, 2022). The IPCC Sixth Assessment Report (AR6) estimates the current global drought risk as a composition of hazard, vulnerability and exposure, see Figure 17. Note that, southern Europe is classified as *high,* in the first two indicators, and as moderate, in the third, resulting in having an overall high drought risk.
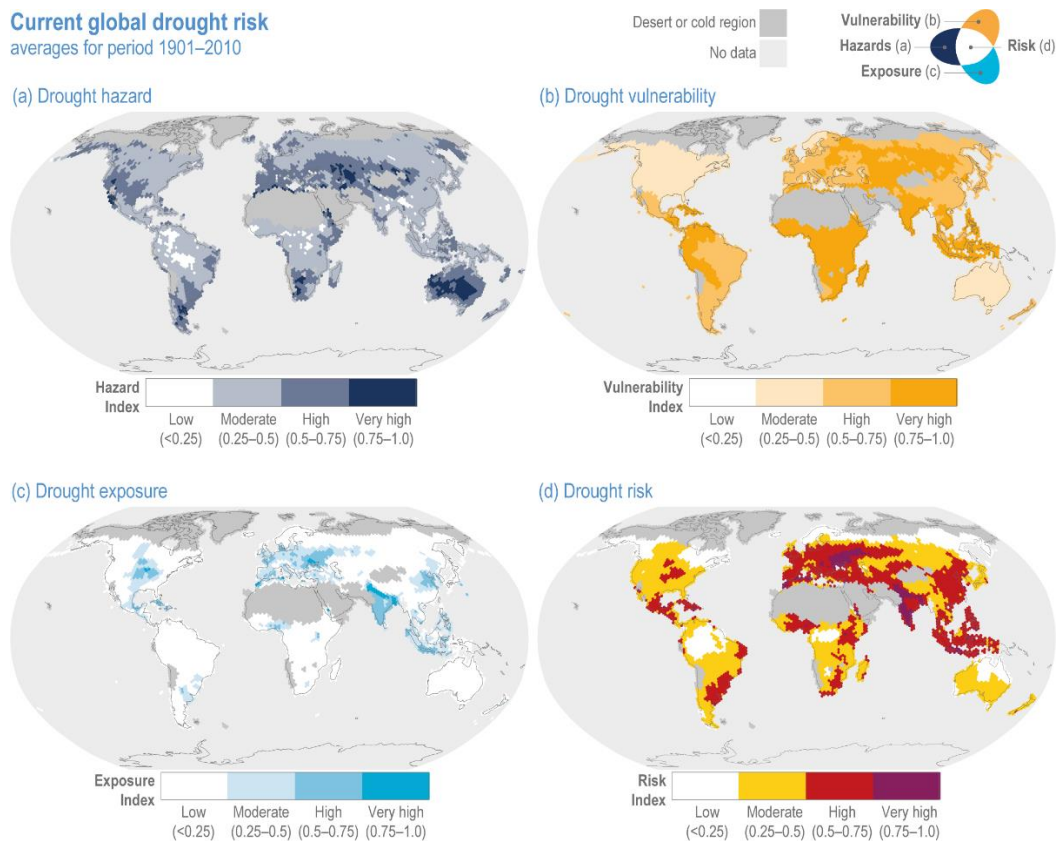
Figure 17. Current global drought risk. Source: Figure 4.9 in (IPCC, 2022)

To mitigate this risk, communities are leaning towards more reliable water resources, such as groundwater as it provides socio-economic benefits thanks to its buffering action to the changing patterns of precipitation events. Indeed, groundwater can often guarantee a continuous drinking water supply, as well as the minimization of agricultural yield losses, having a key role as 23% of global croplands are irrigated (IPCC, 2022). For instance, as of 2017, in Europe groundwater contributed to nearly 25% of freshwater abstractions, whose 60% was dedicated to agricultural activities (WISE, 2024). The discouraging side effect of relying on groundwater is the tendency to over-extraction. Accordingly, even though global abstractions account for only 6% of annual recharge, some hotspots of groundwater depletion due to over-exploitation for irrigation have been identified. For instance, global models are projecting anthropogenic depletion at rates higher than 20 mm/y in major aquifers, such as High Plains and California Central Valley aquifers (USA), Arabian aquifer (Middle East), North-Western Sahara Aquifer System (North Africa), Indo-Gangetic Basin (India) and North China Plain (China). Besides, the AR6 concludes that Groundwater Storage (GWS) has declined in many regions, especially since the beginning of the XXI century, due to the intensification of groundwater-fed irrigation (IPCC, 2022).

As far as future projections are concerned, climatic models forced with different Global Warming Levels (GWLs), under the CMIP6 experiment, allow to predict changes in the probability distribution of agricultural droughts. Figure 18 shows that in the Mediterranean area the likelihood of an extreme single-year drought event will be nearly +100% (meaning it will double) at +1.5°C GWL, at around +150-200% at +2°C GWL and above +200% at +4°C GWL.
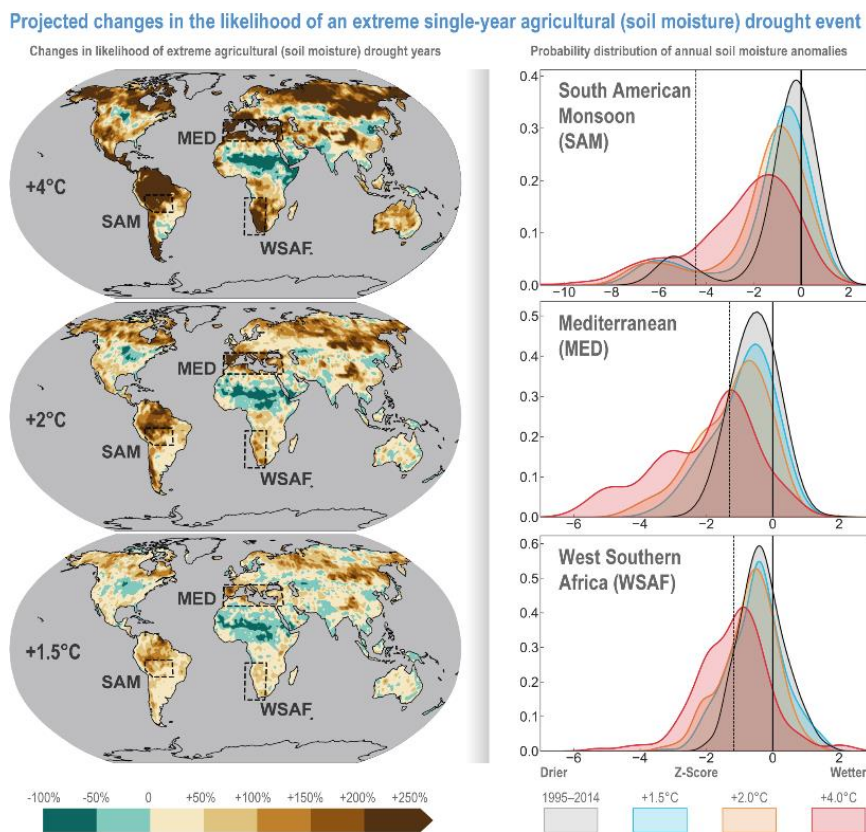
Figure 18. Projected changes in the likelihood of an extreme single-year agricultural drought event (on the left); pdf curve of annual soil moisture anomalies (on the right). Source: Figure 4.18 in (IPCC, 2022)

On top of this, climate models estimate that groundwater abstractions and depletion will grow as a response to increased evapotranspiration (ET) in the warmer climate; whereas groundwater quality will be challenged by anthropogenic pollution (often connected to agricultural activities) and salt-water intrusion due to sea-level rise. (IPCC, 2022)

Finally, the importance of adaptation must be stressed, especially in the agricultural sector where water-related actions currently represent the majority of the already implemented solutions, along with new cultural practices.

3.1.2 The regional scale: Europe

On average, in the years 2000 to 2019, almost 30% of the EU territory was annually affected by water scarcity for at least one season. Despite the reduction in freshwater abstractions, the conditions have worsened and climate change is expected to further enhance the frequency, intensity and impacts of drought events in the area (EEA, 2023). The European Environment Agency (EEA) states that the water scarcity is more pronounced in southern Europe: 30% of the population lives in areas with permanent water stress and, instead, up to 70% experiences seasonal water stress during summer. Therefore, immediate and effective action is strongly required by all Member States.

Accordingly, the (*Water Framework Directive (WFD) 2000/60/EC*, 2000) regulates the management of freshwater quality, along with requiring reports about the ecological status of water bodies and providing guidelines for international River Basin Management Plans (RBMP). One of the indicators widely used to assess the status of water bodies and provide comparable results in reports, under the WFD requirements, is the Water Exploitation Index (WEI) or its georeferenced version WEI+ (ISPRA et al., 2023). The WEI compares the water consumption, computed as the difference between abstractions and returns, to the renewable freshwater resources available in the study-area in a given time frame. The Directive gives two thresholds: values of WEI above 20% represent resources under stress, but values above 40% correspond to severe stress and unsustainable water use.

The EEA published the results of a study that compares the current situation with what could happen under a scenario in which no action against climate change is implemented. It is evident that an overall increase in water stress would diffuse around Europe, especially in the Italian peninsula and in the Po basin which would go from *mild* to *severe* water stress, see Figure 19. Similarly, Istituto Superiore per la Protezione e la Ricerca Ambientale (ISPRA) published the results of the WEI computation for the seven Italian basin districts in the summer of 2019; Figure 20 highlights the severe water stress in a wide portion of the territory: river Po district, southern Italy and the islands.

Water stress indicator WEI for annual average on river basin level for the a) baseline, b) 2050 under 'economy comes first' scenario, and c) compared with urban population numbers

Withdrawals-to-availability ratio
- 0–0.2 (low water stress)
- 0.2–0.4 (mid water stress)
- > 0.4 (high water stress)
- No data
- Outside data coverage

Total population in cities, 2004
- < 100 000
- 100 000–250 000
- 250 000–500 000
- 500 000–1 000 000
- > 1 000 000

Figure 19. WEI over Europe under current conditions (a) and Economy Comes First scenario (b). Source: (EEA, 2017)
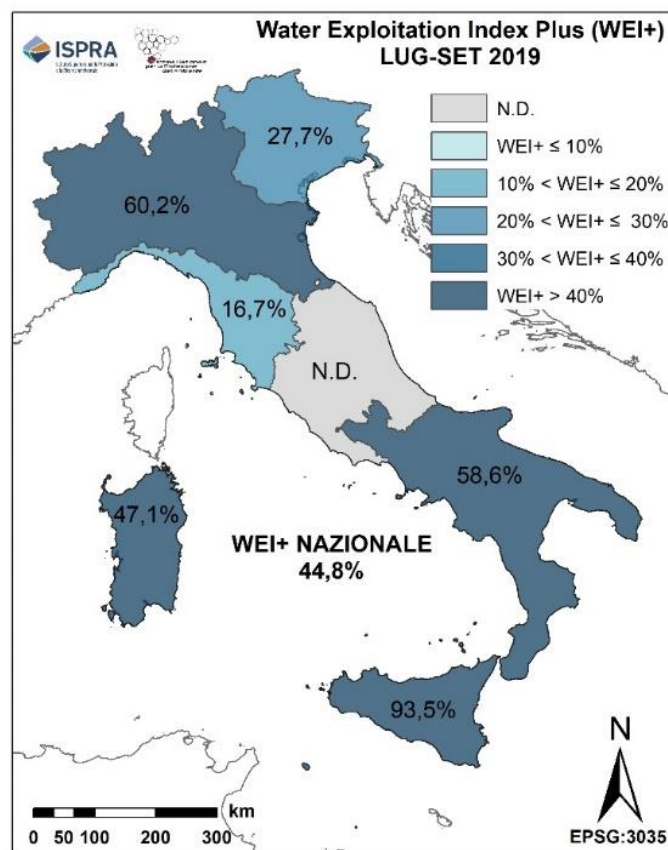
Figure 20. WEI+ in Italy over the summer 2019. Source:(ISPRA et al., 2023)

3.2 Groundwater monitoring via satellites

As highlighted in the previous paragraph, groundwater often plays a key role in the mitigation of climate change consequences, especially for the agricultural sector. Instead, evidence of climate change impacts directly on groundwater is still limited due to the small spatio-temporal coverage of the available data (IPCC, 2022). For this reason, there has been a growing interest into monitoring and modelling groundwater resources, not only to investigate their quality and abundance, but also to allow their just and sustainable management, in line with the UN Agenda 2030 Sustainable Development Goals.

Over the last few decades, the technological evolution has been fundamental to improve the capabilities and the efficiency of groundwater inspection. Indeed, other than ground-data, the revolution in this research field was the introduction of gravimetric data acquired from satellites. To put it in a nutshell, it consists of measuring the Earth's gravitational field in order to estimate the mass changes around the planet, which are often connected to changes in the Total Water Storage (TWS) (Segobye et al., 2023). In other words, gravimetry is used to study the evolution of the hydrological cycle, as it allows to reconstruct the transport of water masses across the globe.

The state of the art for this technology is the Gravity Recovery And Climate Experiment (GRACE) Mission conducted by NASA, in cooperation with Potsdams's GeoForschungs Zentrum (ESA), from 2002 to 2017 and followed by the GRACE-FO Mission, which is still ongoing (ESA, 2020). Both missions are based on the same working mechanism: they require two twin satellites orbiting around the Earth at close distance between one another. The payload is a microwave satellite-to-satellite tracking technology, which monitors the distance in between the pair of satellites (NASA JPL | Podaac, 2017). Figure 21 represents the functioning mechanism: in presence of a positive gravimetric anomaly, the first satellite is subject to an acceleration which causes a mismatch in the constant distance between the two satellites, typical of the undisturbed conditions; later, also the second satellite will be subject to the same acceleration and finally the usual distance will be established again, once the anomaly has passed by. The microwave tracking, along with accelerometers and GPS, allows to reconstruct the position of the satellites and, therefore, to georeference the data (Amendola, 2022). The raw data retrieved from the satellites is processed by researchers, such as those belonging to the Jet Propulsion Laboratory (JPL) of the California Institute of Technology and is made available on the Physical Oceanography Distributed Active Archive Center (PODAAC). The estimated TWS is actually expressed as centimeters of Water Equivalent Thickness (WET); in particular the timeseries, with monthly resolution (NASA, 2020), is an anomaly referred to the mean value of the period 2004-2010.

Plenty of research is based on the datasets provided by the GRACE Missions, as it allows to investigate the TWS and monitor changes in the water distribution in glaciers, icesheets, land water storage, sea level and ocean currents (ESA, 2020). Moreover, the TWS derived by GRACE is compatible with other types of models, such as the hydrological ones. For instance, having a clear picture of surface water and TWS estimates leads to the deduction of the Groundwater Storage Anomaly (GWSA), as it will be explained later on.
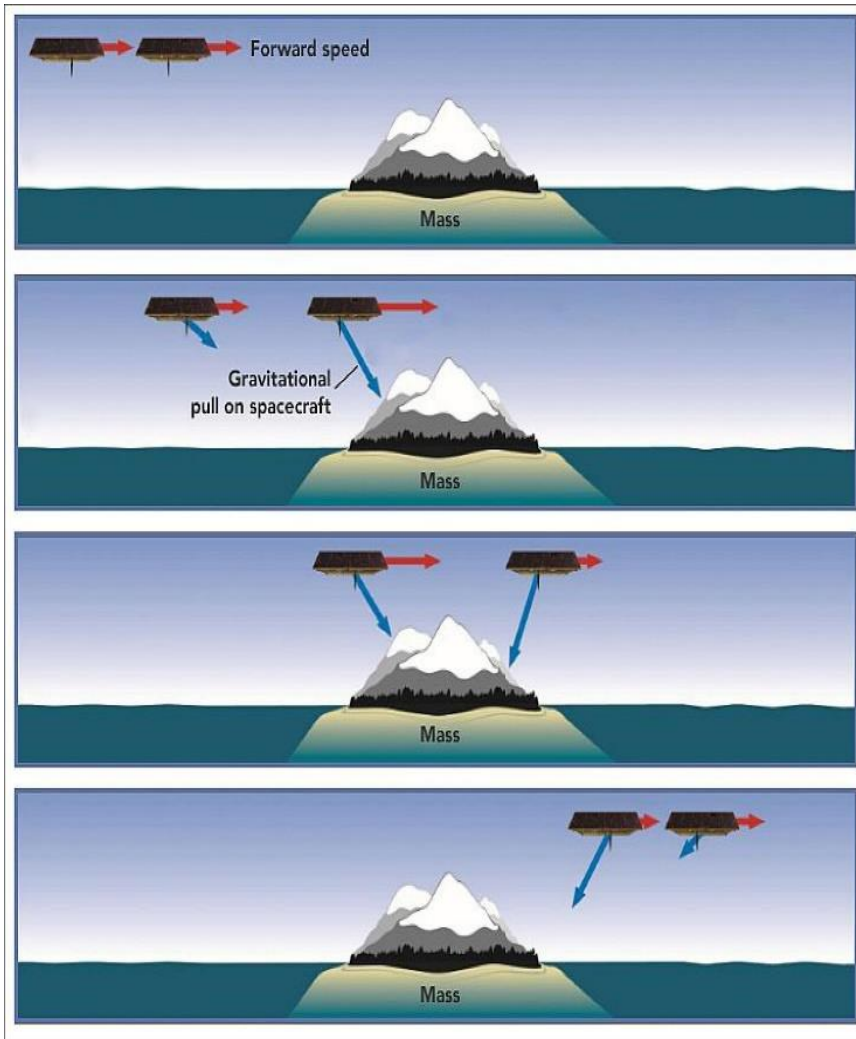
Figure 21. GRACE working mechanism infographic. Source:(EO Portal, 2013)

3.2.1 The regional scale: Mediterranean Area

The procedure mentioned above to estimate the GWSA was applied by Xanke & Liesch (2022) over Europe, northern Africa and Middle East. Figure 22 shows that, for the period 2003-2020, 82% of the investigated area had a very significant trend in GWSA, with p values lower than 0.01, and another 5% had still a significant trend, with p values lower than 0.05. Out of this total 87%, only 20% had positive values, meaning that recharge exceeded abstractions and there was an ongoing recovery of the resource, whereas most of the area, 80%, shows signs of depletion. The most important hot spots were identified in the Persian peninsula, continental Europe and northern Algeria. Note that across north-western Italy a significant trend in the range -3 to -6 mm/year, with p value < 0.05, was recognized.
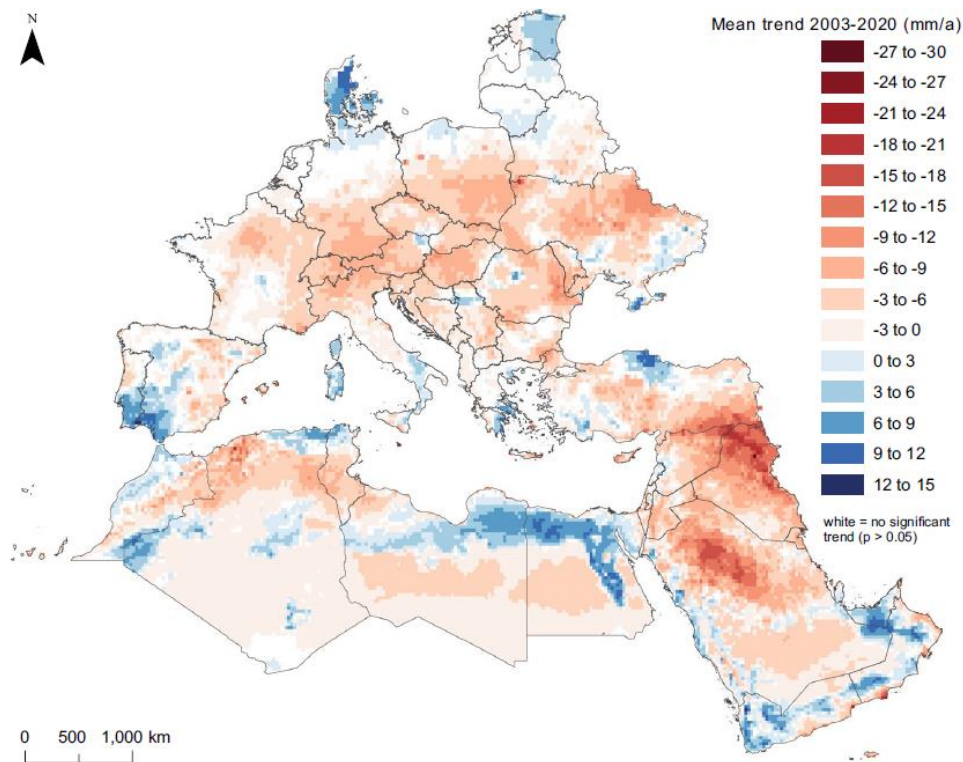
Figure 22. Mean annual trend of GRACE-derived GWSA in the Euro-Mediterranean region (2003-2020). Source: (Xanke & Liesch, 2022)

3.3 Application of satellite groundwater monitoring to the Cuneo Province

As mentioned previously, the morphology of the study area is characterized by a vast alluvial plain with several aquifers. For this reason, as wells as for the fact that agriculture is one of the main activities in this location, the area is particularly suitable for this type of analysis, especially since there has been growing interest into managing the resource in a way to improve resilience to climate change. For reference, the location of the Monregalese is represented in Figure 23 along with the geographical coordinates that will be used to define the cells of interest from the global models.
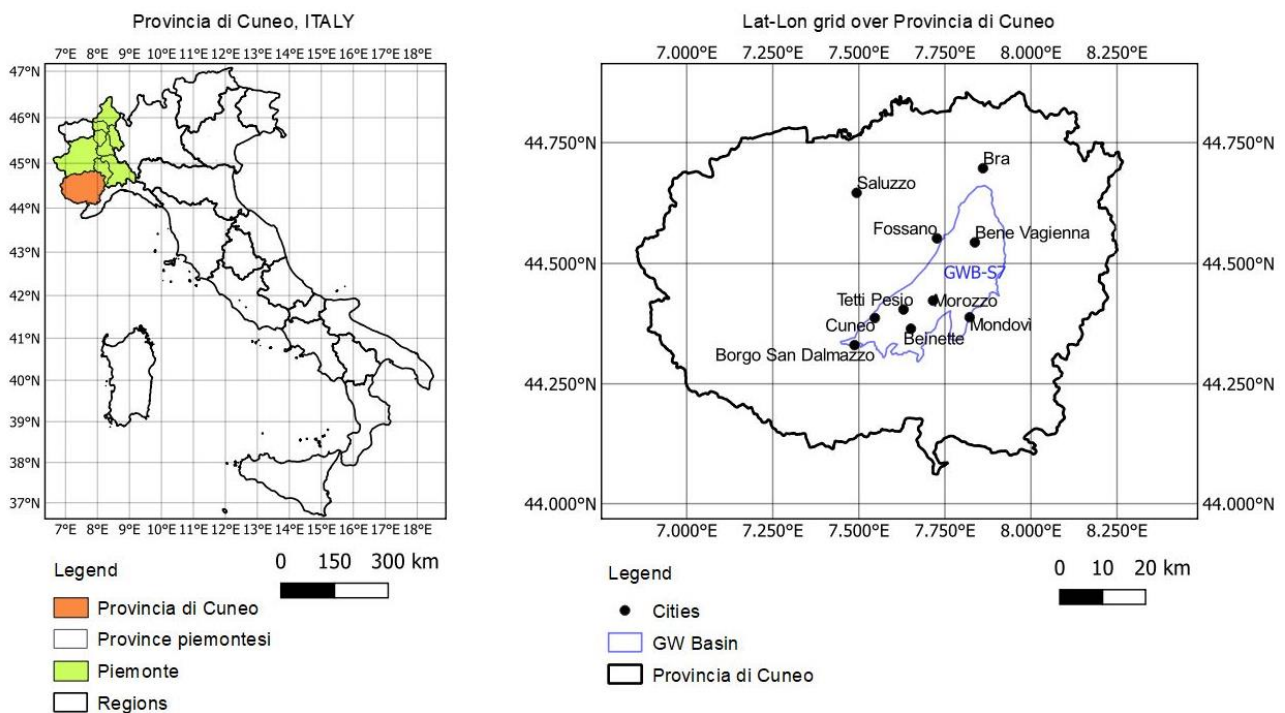
Figure 23. Location of the study area. View of the Piemonte Region (left) and the Cuneo Province (right). The geographical coordinates are expressed in decimal degrees (°).

To begin with, a first analysis of the GRACE Water Equivalent Thickness (WET) at a 1° resolution, retrieved from the GRACE Data Analysis Tool (refer to Data Source 1), was carried out. The selected grid cell has coordinates 44-45°N and 7-8°E. Figure 24 highlights an evident trend over time: it accounts for about -7.7 mm/y. But taking a closer look at the plot, it is possible to notice much lower values of WET towards the end of the timeseries. Consequently, following a visual interpretation, the dataset was divided into two subsamples, the first one going from 2002 to 2014 and the second one from 2015 to 2023. Then, a statistical test was carried out, in particular the *paired sample t-test*, to check whether they belonged to the same distribution. The null hypothesis H_0 stated that the samples belonged to normal distributions with equal means and unknown, but equal, variances; the alternative was H_1, stating that they come from populations with different means. The significance level was set at 5%. The procedure, implemented on Matlab Simulink, showed that the null hypothesis could be rejected at the 5% significance level and the p-value in the order of magnitude of 10^{-18} suggested that there was

high confidence, since it represents the probability of observing the given result, or one more extreme, by chance if the null hypothesis was true. The computation of the GWSA at higher resolution has been carried out from scratch and will be presented in the next paragraph.
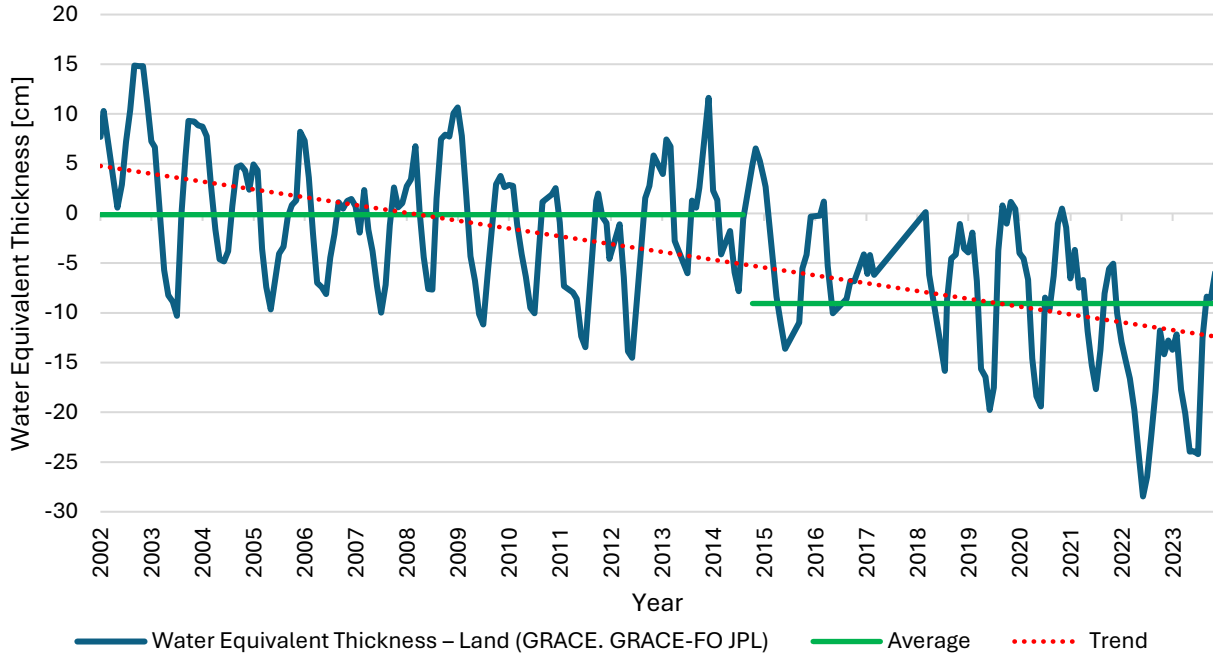
Figure 24. TWS Anomaly (GRACE / GRACE-FO, JPL); referred to the 2004-2010 baseline. In red the trend over the whole time period (-7.7 mm/y) and in green the means of the two subsamples tested.

3.3.1 Methodology to estimate GWSA

The methodology is based on the assumption that the Total Water Storage anomaly (ΔTWS) is made out of the contribution of several components of storage changes: snow-melted water equivalent (SWE), surface water storage (SWS), groundwater storage (GWS), plant canopy (CA) and, finally, soil moisture (SM) (Daqiq et al., 2023). The monthly evolution of each storage variable is indicated by means of the Greek letter "Δ" in the following equations.

$Eq.\,1$: $\Delta TWS = \Delta SWE + \Delta SWS + \Delta GWS + \Delta CA + \Delta SM$ (Thomas & Famiglietti, 2019)

The most direct source of TWS timeseries are GRACE data, since hydrological models estimate them from the water balance, therefore amplifying possible errors. With this being said, all the other hydrological variables can be retrieved from the simulations of global models, such as the Global Land Data Assimilation System (GLDAS) which is recommended in the GRACE Level 3 User Handbook (Cooley & Landerer, 2020). As a matter of fact, these models combine observations of meteorological timeseries and land surface models, including soil type, vegetation and land-use, which manifest different hydrological responses. Consequently, rearranging Eq. 1 and assuming that surface reservoir storage is negligible in the area of interest, GWSA can be derived as follows.

$Eq.\,2$: $GWSA = \Delta TWS - (\Delta SM + \Delta SWE + \Delta CA)$ (Rzepecka & Birylo, 2020)

33

Furthermore, the timeseries of GWSA can be analyzed to evaluate trends or seasonality features (Lin et al., 2022). A step-by-step guide to the computation of GWSA is provided below.

Step 1 – WET (GRACE/GRACE FO)

Firstly, the monthly timeseries of the WET at a 0.5° resolution was retrieved from the Podaac platform (refer to Data Source 2): the selected grid cell has coordinates 44-44.5°N and 7.5-8°E. Note that some data is missing due to satellites' unavailability or due to the interchange period between the two missions. Following several attempts and validation procedures, it was decided to neglect the Scale Factor provided along with the WET tables. As a matter of fact, this factor was responsible for a strong attenuation of the signal and caused an underestimation of the trend of the WET over the whole period in this specific study area, see Figure 25. The trend turns out to be equal to -7.8576 mm/y, in agreement with that of Figure 24 computed for the wider cell.
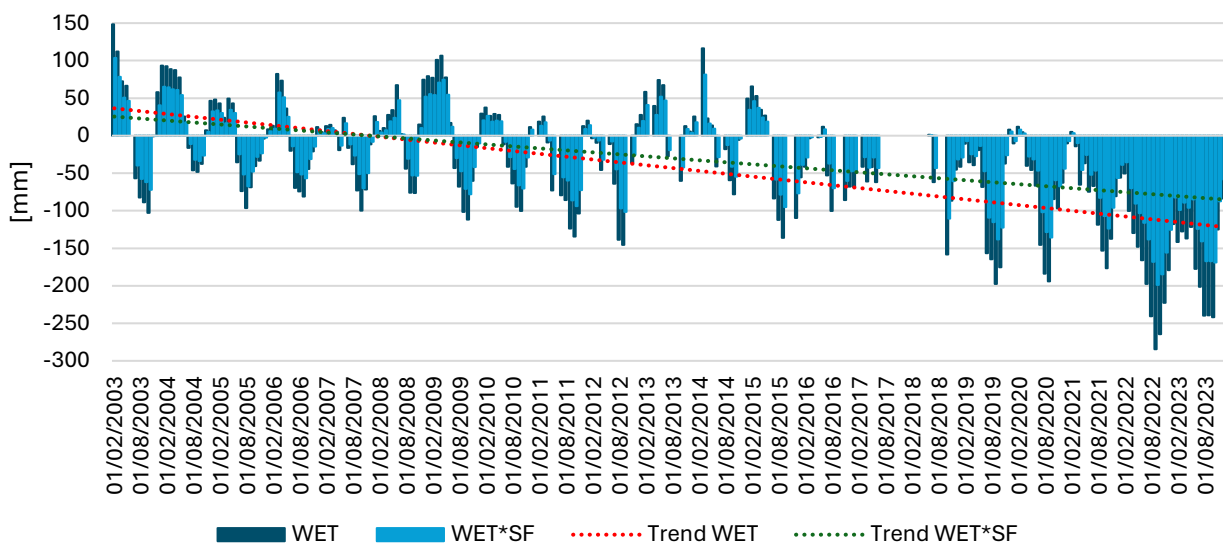
Figure 25. GRACE Water Equivalent Thickness for the grid cell 44-44.5°N 7.5-8° E. WET with and without SF are represented respectively in light and dark blue. The dotted lines are the trends over the whole time period.

Step 2 – Hydrological model (GLDAS)

For the present study the reference hydrological model chosen is the GLDAS v2.2. The GLDAS is a hydrological model forced with meteorological data, but this particular version, instead, also involves an archive with GRACE Data Assimilation of TWS and meteorological analysis fields from the European Centre for Medium-Range Weather Forecasts (ECMWF). As far as the Land Surface Model (LSM) is concerned, the Catchment LSM (CLSM) was chosen. Its bands involve variables such as: soil moisture, snow depth, snow melt, runoff, terrestrial water storage, groundwater storage, canopy water, evapotranspiration, temperature, heat and radiation fluxes. In agreement with (Hussain et al., 2021) and (Rui & Beaudoing, 2020) the layers downloaded were:

1. *SWE_tavg*: Snow depth water equivalent
2. *CanopInt_tavg*: Plant canopy surface water
3. *SoilMoist_RZ_tavg*: Root Zone Soil moisture

34

As a matter of fact, the CLSM definition of soil moisture (SM) obligates to readjust Eq.2, as the GLDAS manual states that the TWS includes the GWS, but also SM includes GWS. In particular, the Surface SM refers to the shallowest 2 cm of soil, instead, Root Zone reaches 1 m in depth and includes the Surface SM (Rui & Beaudoing, 2020). Whatever is below 1 m is considered as groundwater and is included in Profile SM, which is as thick as the whole subsoil given in the LSM, see Figure 26. For this reason, the GWS is computed as follows:

$$Eq.\,3: \quad GWS \,=\, TWS - (RZ_{SM} + SWE + CA) \qquad \text{(Rui \& Beaudoing, 2020)}$$
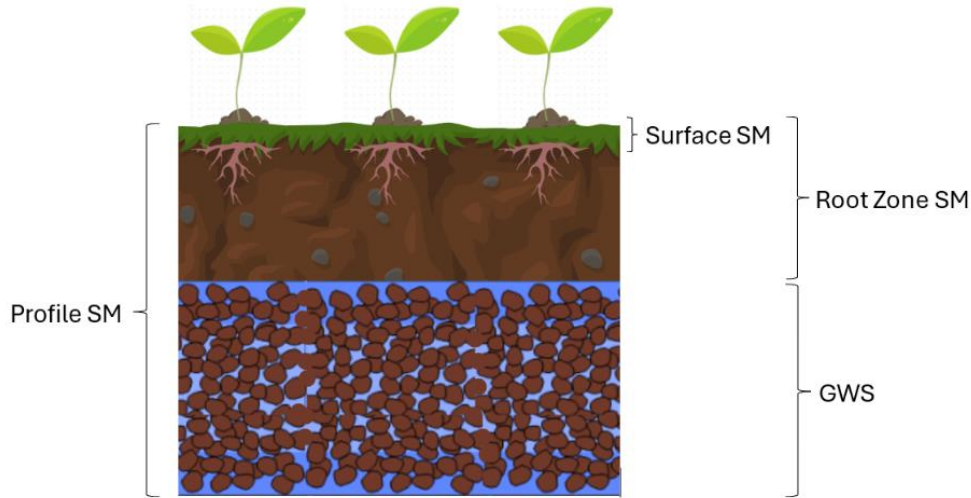
Figure 26. Representation of the SM and GWS layers in the CLSM.

Consequently, to apply Eq.2 the layer of SM chosen is the Root Zone and the estimated TWS is substituted by the WET given by GRACE:

$$Eq.\,4: \quad GWSA \,=\, \Delta WET - (\Delta RZ_{SM} + \Delta SWE + \Delta CA)$$

The GLDAS grid is made available at a resolution of 0.25° (Data Source 3). Therefore, the cell covering the area of interest is the one centered in Morozzo, having coordinates: 44.25-44.50°N 7.50-7.75°E; but, also the adjacent ones, still lying within the cell from GRACE, are taken into account, see Figure 23. In order to have a dataset comparable with the WET from GRACE, all units were brought to millimeters and the daily timescale was converted into monthly. For the same reason, the timeseries from GLDAS, made out of absolute numbers, had to be converted into anomalies by subtracting, also in this case, the average GLDAS value calculated over the reference period 2004-2010.

The sum of the anomalies coming from the GLDAS layers is represented in Figure 27, the greatest contribution is to be attributed, counterintuitively, to the soil moisture. Overall, the trend is about -0.5148 mm/y, corresponding to approximately 6.6% of the trend from GRACE, if the values corresponding those missing in the WET are denied.
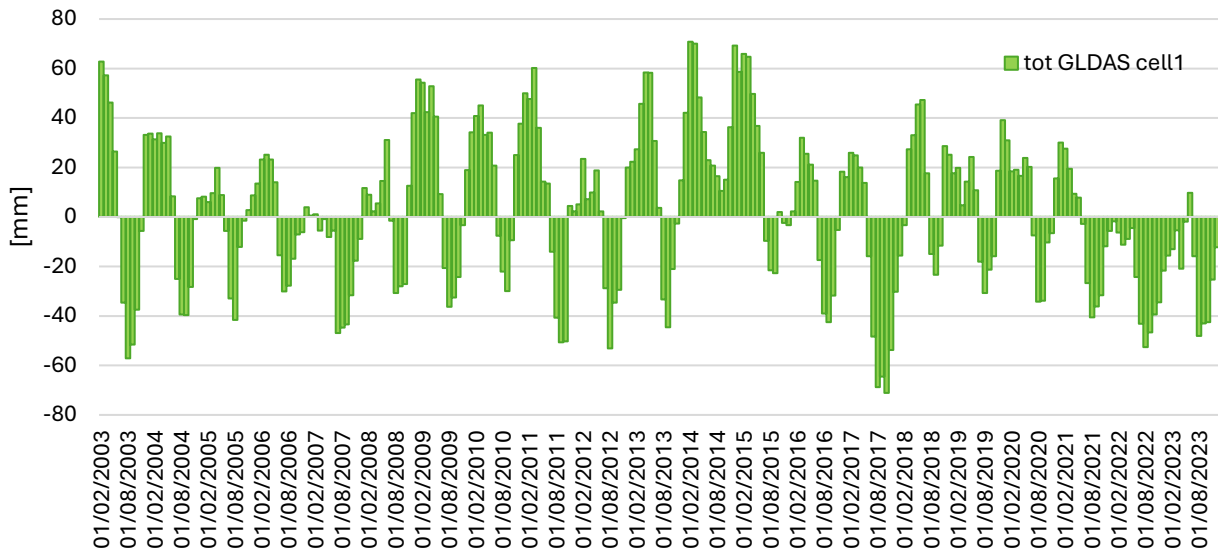
Figure 27. Total contribution of the GLDAS layers as the sum of the Root Zone SM, SWE and CP anomalies in the cell centered in Morozzo (cell 1).

Step 3 – GWSA

At this point, implementing Eq. 4, the computation of the GWSA is immediate. The results, reported in Figure 28 are analyzed and the trend is found to be equal to -7.0728 mm/year, contributing for the 90% of the WET trend evaluated before. The comparison with the adjacent cells can be found in Figure 29. As a matter of fact, over the analyzed period the groundwater depletion accounted for almost 150 mm. Furthermore, the test of the linear regression showed that the slope coefficient does significantly differ from zero, therefore the trend is not negligible, with very high confidence. Besides, the result is in line with those obtained in Figure 22 (Xanke & Liesch, 2022), providing a validation of the work.
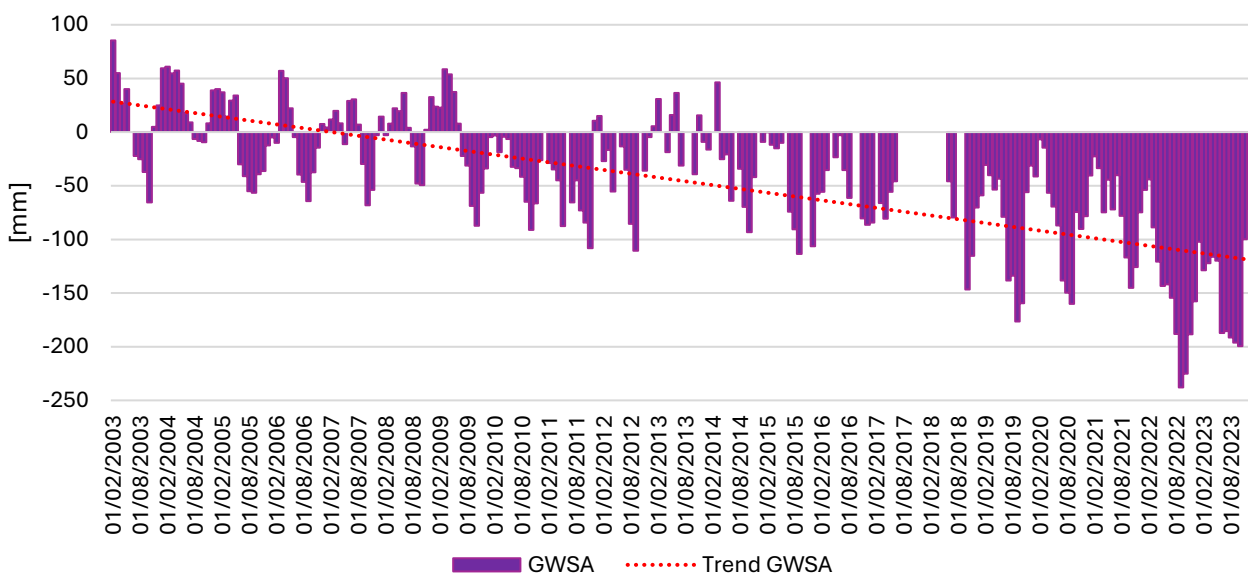
Figure 28. GWSA (2003-2023) for the cell centered in Morozzo (cell 1). Note that there are some missing values due to satellite unavailability; the trend is represented by the dotted line.

36
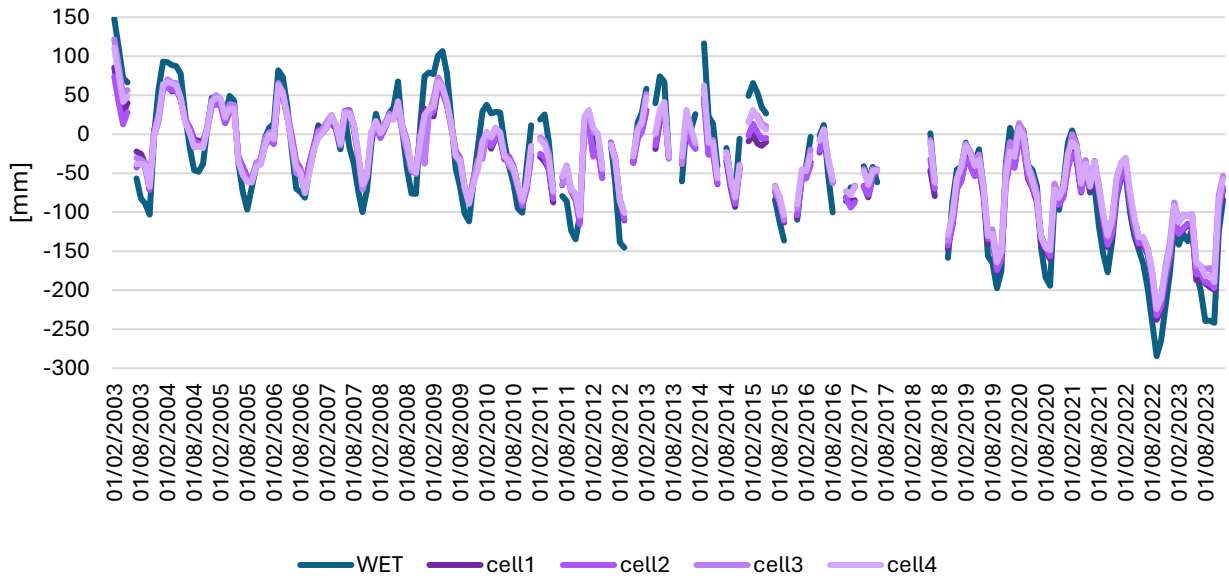
Figure 29. GWSA for the period 2003-2023 in the four adjacent cells (for their coordinates refer to Figure 23). WET is reported for reference, in blue. Note that there are some missing values due to satellite unavailability.

Step 4 – GGDI

To conclude, the GRACE Groundwater Drought Index (GGDI), which can be derived from the GWSA according to the Eq. 5, is a helpful indicator to identify and monitor hotspots of significant groundwater depletion (Han et al., 2021) . The output, represented below, highlights months of severe drought conditions: GGDI< -0.5 (Cantoni et al., 2024).

$$Eq.5: \quad GGDI = \frac{GWSA_t - \overline{GWSA}}{\sigma_{GWSA}} \qquad \text{(Rzepecka \& Birylo, 2020)}$$
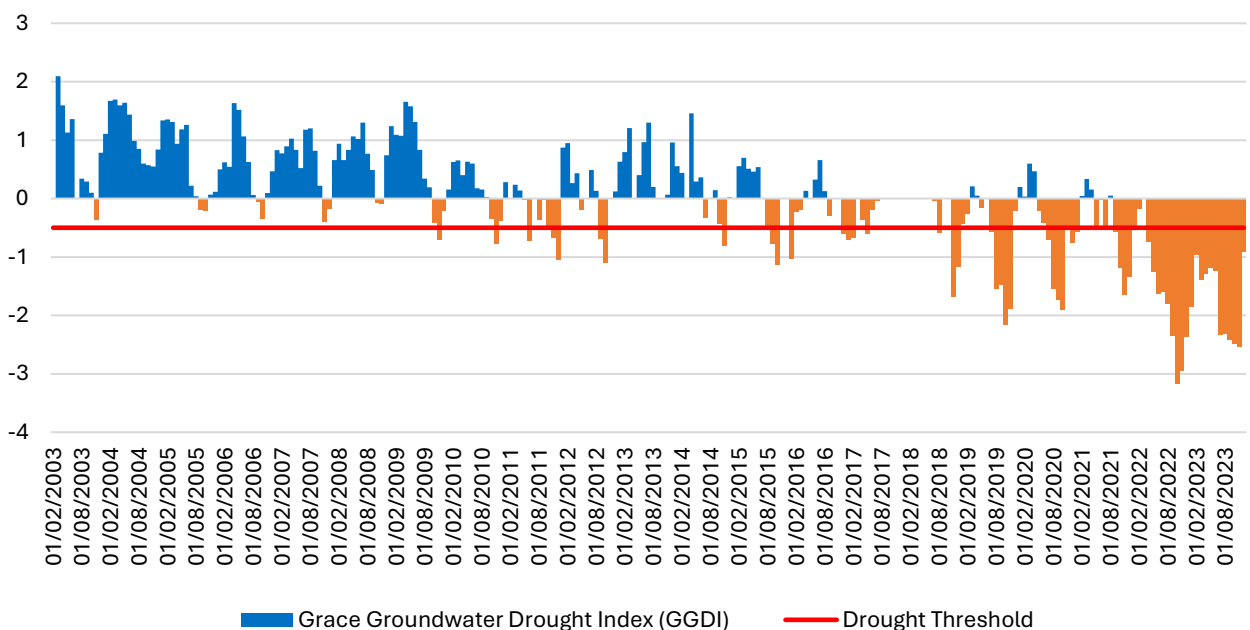
Figure 30. GRACE Groundwater Drought Index (2003-2023) for the cell centered in Morozzo (cell 1). Positive values in blue, negative values in orange, the threshold, in red, indicates severe drought conditions (GGDI<-0.5).

Validation of the results

Ultimately, it is recommended to always validate the results. For this reason, the timeseries of GWSA is compared to the Depth to Groundwater measured in Morozzo from January 2012 until June 2023. The timeseries is published by the regional agency for environmental protection (ARPA Piemonte) and it refers to the shallow unconfined aquifer GWB-S7 (see Figure 13), monitored in the well T2-Morozzo, code 00414410001. Figure 31 shows that the two variables are mostly in phase: whenever the Depth to Groundwater increases the GWSA shows more negative anomalies. As a matter of fact, they have a correlation equal to -0.48. Despite this, some misalignment can be seen in the period following the change of the pair of satellite, moving from the GRACE to the GRACE-FO mission. Indeed, another factor affecting the accuracy of the validation could be the activation of the pumps for irrigation purposes in the surroundings of the monitoring well.
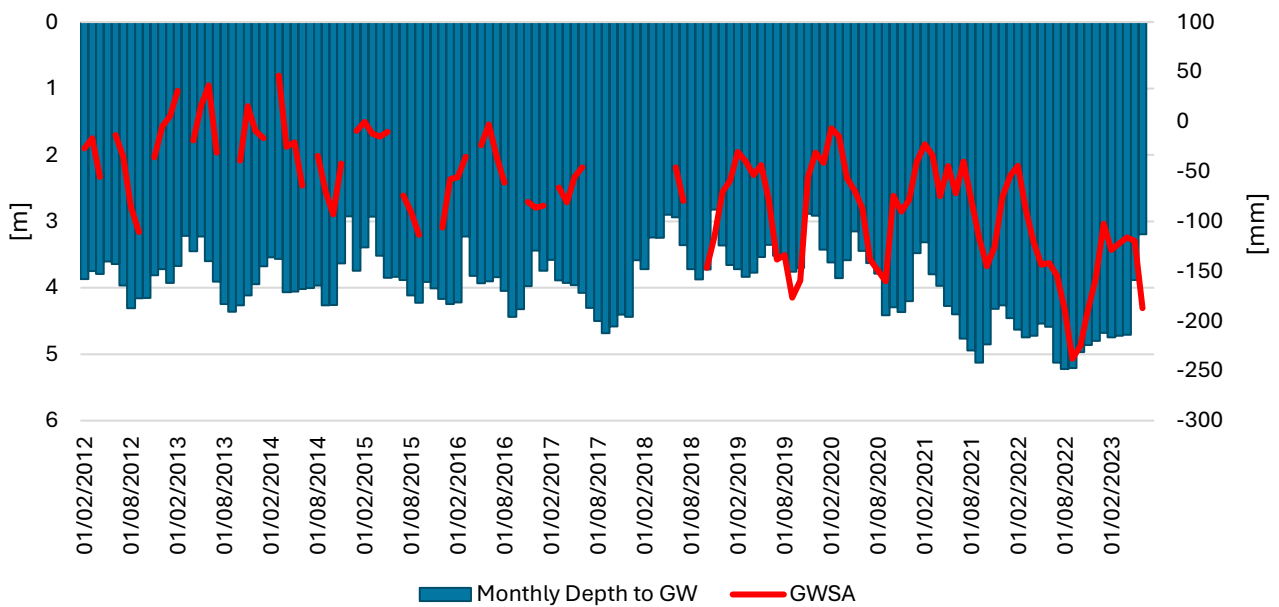
Figure 31. Comparison between Depth to GW in Morozzo and GWSA.

4 Groundwater flow modelling

4.1 Methodology

Groundwater modelling follows a multistep approach, along which complexity and quantitative description of the system gradually increase. The preliminary phase is the correct identification of the study objectives, followed by an initial recognition and collection of the data that is already available. As a result, a conceptual model is created. It consists of a basic and mostly qualitative description of the system, where the connection between different compartments of the model can be highlighted. Afterwards, a careful characterization of the site is usually planned considering field tests, aquifer tests and data analysis. Furthermore, the parameters retrieved by the interpretation of the results of the field campaign are added to the conceptual model to create the final quantitative model.

The present work is mostly based on conceptual modelling, aimed at understanding the peculiarity of the *fontanili* and MAR site and their connection to the water table. The software employed for the simulations is HYDRUS, released by PC-Progress. It allows to simulate water, heat and solute transport in variably saturated porous media. For the purpose of this study, only water flow is considered, and it is computed by solving the Richard's equation (Šimůnek & Šejna, 2022). As a matter of fact, the classical formulation of Darcy Law, which is convenient to describe flows in saturated porous media, has to be adapted in order to model the shallow subsoil and, in particular, the flow in unsaturated porous media. By combining the latter with the continuity equation, the Richard's equation is obtained:

$$Eq.\,6: \quad \frac{\partial \theta}{\partial t} = \frac{\partial}{\partial x_i}\left[K \left(K_{ij}^A \frac{\partial h}{\partial x_j} + K_{iz}^A \right) \right] - S$$

where θ is the volumetric water content [L³L⁻³], h is the pressure head [L] defined as the pressure term $h = p/\gamma$ of the hydraulic head H, S is a sink term [T⁻¹], x_i ($i = 1, 2, 3$) are the spatial coordinates [L], t is time [T], K_{ij}^A are the components of an anisotropy tensor [-], and K is the unsaturated hydraulic conductivity [LT⁻¹] (Šimůnek & Šejna, 2022). The retention curves, describing the evolution of the soil characteristics, such as hydraulic conductivity, depending on the water content are fitted by the van Genuchten model:

$$Eq.\,7: \quad K(\Theta) = K_{sat}\Theta^{\frac{1}{2}}\left[1 - \left(1 - \Theta^{\frac{1}{m}} \right)^m \right]^2$$

where K_{sat} is the saturated hydraulic conductivity [LT⁻¹], Θ is the dimensionless water content defines as $\Theta = \frac{\theta - \theta_r}{\vartheta_s - \theta_r}$ where r means residual and s the saturated water content, and m is an empirical parameter [-]; modified from (van Genuchten, 1980). Hydrus solves the water flow equation by means of the Galerkin finite element method. The spatial discretization consists of the subdivision of the domain into a network of triangular (2D) or tetrahedral (3D) elements, whose corners make up the nodes of the computational mesh. Consequently, the Neumann, flux type, and gradient boundary conditions are immediately incorporated into the numerical scheme. Instead, the time discretization involves the definition of finite intervals and the substitution of the time derivatives with finite differences. Moreover, due to the nonlinear

nature of the problem, an iterative procedure is implemented. For each iteration, a set of linearized equations is derived, the boundary conditions are incorporated, and the system is solved the Gaussian elimination method or the conjugate gradient method. These steps are replicated incorporating every time the new results until a satisfactory convergence is reached. In particular, the water content or pressure head change between two consecutive iterations must be smaller than the tolerance set. In parallel, the mass conservation equation is solved, and it allows to minimize the mass balance errors. During the solution process, the time discretization is adapted to the number of iterations used: if the previous solution was easily obtained, the time increment is reduced and vice versa. Whenever the number of iterations exceeds the predetermined threshold the computation is terminated (Šimůnek & Šejna, 2022).

The procedure to generate a numerical simulation on HYDRUS is the following:
   a) Construction of the geometry of the system by means of points, curves, surfaces and solids; but also cavities, which consist of holes in the domain and integrated objects, used when a single object lies within another one;
   b) Generation of the computational mesh with possible customized refinements;
   c) Definition of the domain properties (e.g. material associated to the geometry such as sand, loamy sand, clay etc..);
   d) Setting simulation parameters (e.g. time discretization and duration of the simulation);
   e) Setting water flow parameters (e.g. van Genuchten model, time variable conditions);
   f) Setting initial conditions;
   g) Setting boundary conditions;
   h) Calculation and display of the results.

4.2 Conceptual Model: Fontanile

First, it is necessary to present more in detail the typical structure of a drainage trench, also known as *fontanile*. On a general basis, each *fontanile* is made of three main structures: the head, the gorge and the furrow, see Figure 32. The head consists of a round depression in the ground level, usually excavated until the interception with the shallow unconfined aquifer. Here the groundwater naturally resurfaces. The head can be as large as a few decades of meters and up to 2 m deep. The gorge is a sudden narrowing, located downstream of the head, connecting the latter with the channel. The furrow is the actual trench, excavated to convey the water across the agricultural lands. It can reach a length of several hundreds of meters (De Luca et al., 2005). By the end of the IXX century, the structure of the *fontanili* was improved by means of screened boreholes, known as *tubi calandra*, located in the head and along the channels. They reach up to 10 m in length and facilitate the vertical flux of the water, towards the ground level, during times when the water table is deeper, in order to still provide water for irrigation.
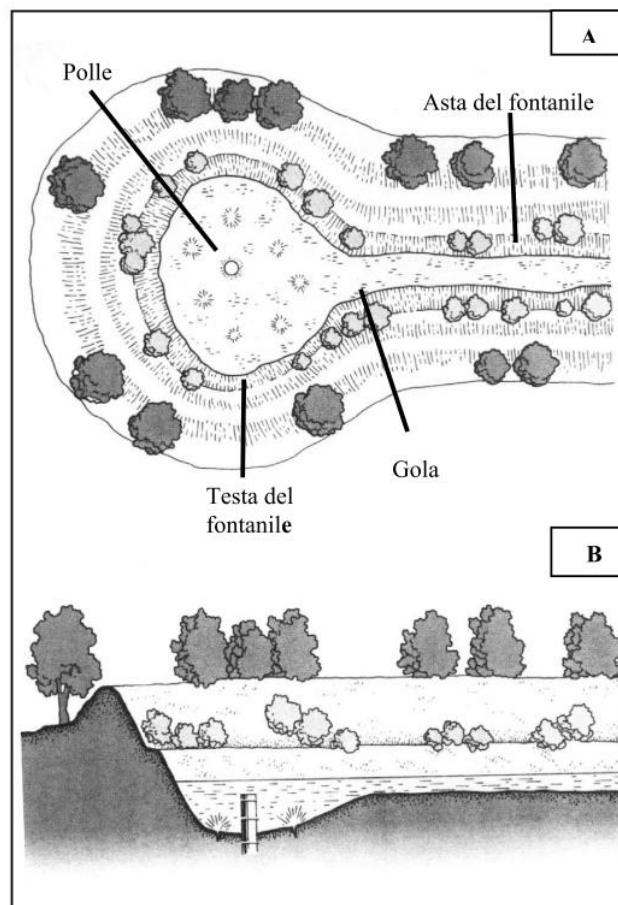
Figure 32. Scheme of a Fontanile, view from above (A) and in section (B). Source: (De Luca et al., 2005)

In the next paragraph multiple sections of a *fontanile* will be analyzed to understand the connection between the surface fluxes and the depth of the water table, as well as the contribution given by the screened boreholes. The geometries presented refer to a generic and hypothetical, but yet representative, *fontanile,* that has been recreated starting from the georeferencing campaigns conducted on the study area.

4.2.1 Section of the furrow

First, the most basic configuration is analyzed as it allows to understand the working mechanism of a drainage infrastructure. The geometry, corresponding to a furrow, is represented below, as well as the boundary conditions: atmospheric at the ground level, constant pressure head at the sides of the domain, no flux at the bottom of the aquifer and seepage face at the base of the furrow (Figure 33). The material, in agreement with the geological knowledge of the area, is set as loamy sand, refer to Table 2. The mesh for the simulation accounts for 4006 nodes and the largest dimension of the finite elements ranges from 0.12 m to 0.84 m.

Table 2. Materials for the simulations: Loamy Sand and Water. Qr and Qs are respectively residual and saturated soil water content; α and n are parameters in the soil-water retention function; Ks is the saturated hydraulic conductivity; I is a tortuosity parameter in the conductivity function.

Mat	Name	Qr [-]	Qs [-]	Alpha [1/m]	n [-]	Ks [m/hour]	I [-]
1	Loamy Sand	0.057	0.41	12.4	2.28	0.145917	0.5
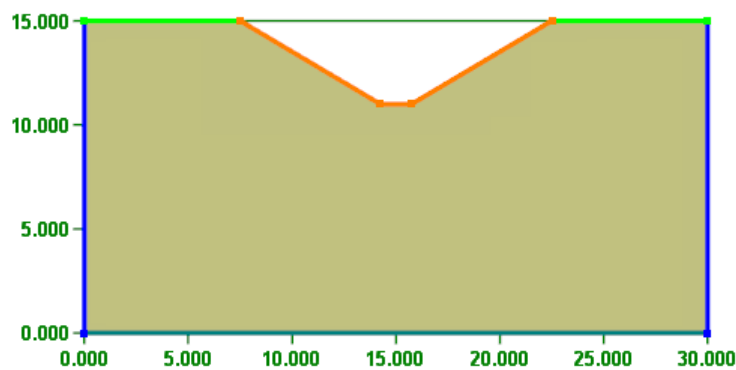
Figure 33. Geometry of a furrow. B.C.: atmospheric in green; constant pressure head (13 m) in blue; no flux in teal; seepage face in orange.

The Figure below shows the results, in terms of pressure head (h), computed at 48 hours from the beginning of the simulation, when the steady state conditions have been reached: the lowering of the ground level, at the base of the channel section, intercepts the water table. Here the water naturally resurfaces. Consequently, the equipotential lines of *h* bend down, in a configuration in which the aquifer is *feeding* the furrow, in other words, it is proving water to the channel, whose flow moves along the third dimension, draining the surroundings.
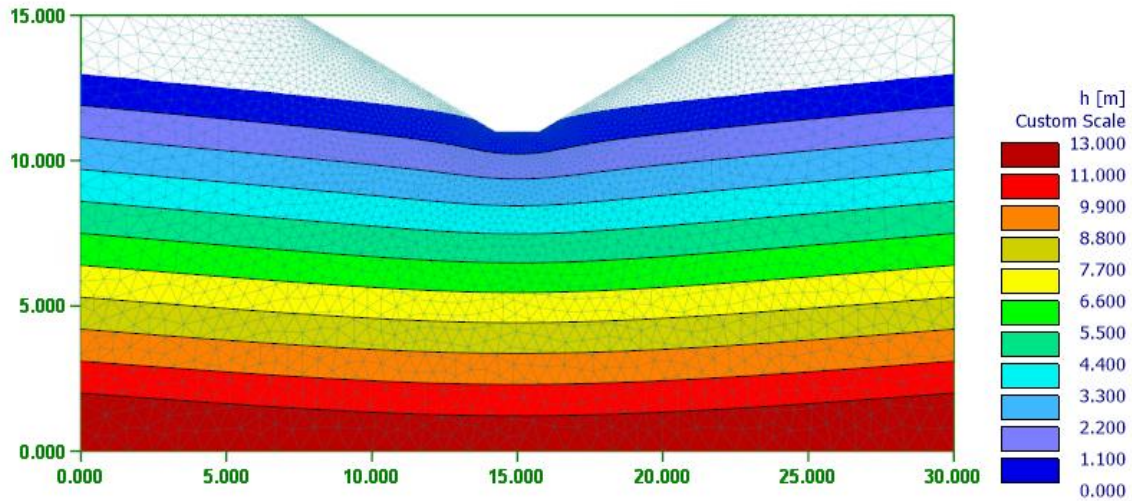
Figure 34. Section of a furrow - Results in terms of Pressure Head @48h.

Now that a basic understanding has been acquired, the geometry can be improved by introducing a second material. The soil remains set as loamy sand, but the water in the channel can be modeled by creating a fictitious material with porosity equal to 1 and extremely high hydraulic conductivity, see Table 3.

Table 3. Materials for the simulations: Loamy Sand and Water. Qr and Qs are respectively residual and saturated soil water content; α and n are parameters in the soil-water retention function; Ks is the saturated hydraulic conductivity; I is a tortuosity parameter in the conductivity function.

Mat	Name	Qr [-]	Qs [-]	Alpha [1/m]	n [-]	Ks [m/hour]	I [-]
1	Loamy Sand	0.057	0.41	12.4	2.28	0.145917	0.5
2	Water	0	1	14.5	2.68	10000	0.5

The boundary conditions (Figure 35) are: atmospheric at the ground level, no flux at the bottom and variable pressure head at the lateral ends of the domain. The schedule of the latter is reported in Table 4. The mesh for the simulation involves 7450 nodes and the largest dimension of the finite elements ranges from 0.12 m to 0.84 m.
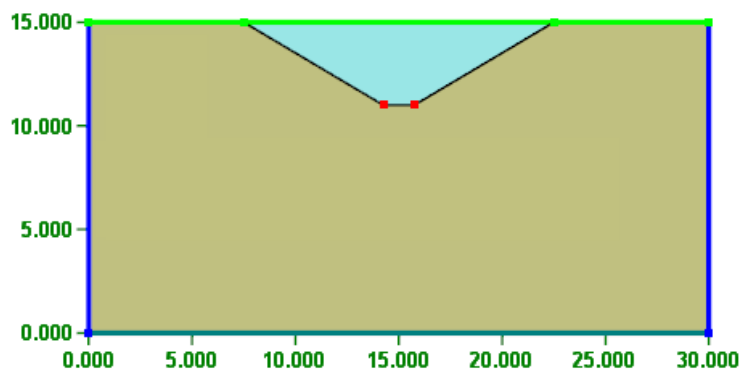
Figure 35. Geometry of a furrow with two materials. B.C.: atmospheric in green; variable pressure head in blue; no flux in teal.

43

Table 4. Section of a furrow - Variable Head B.C. Schedule.

Time [hours]	5	8	11	12	48
Var. Head [m]	10.5	11	11.5	12	13

In the following Figures the results, at 48 hours, are displayed. In particular, this frame of the simulation is showing a transient condition, whereas in the long-term the system would be in equilibrium. The pressure head isolines preserve the same behavior as before, but close to the bed of the furrow the hydraulic gradient is less pronounced due to the connection with the water height modelled in the channel. Indeed, the second material allows the solution of the water content to capture the water level in the furrow and the development of the capillary fringe in the shallow portion of unsaturated soil lying above the water table. Finally, the velocity distribution over the whole domain demonstrates that the flow is moving toward the furrow and that the velocity increases at the interface with the material representing the water, due to the sudden increase in hydraulic conductivity. Despite this, the vectors of the velocities in this configuration are concentrated below the bed of the furrow, whereas in the previous case, with the seepage face boundary condition all around the cross section, they were intensified all around the wet perimeter.
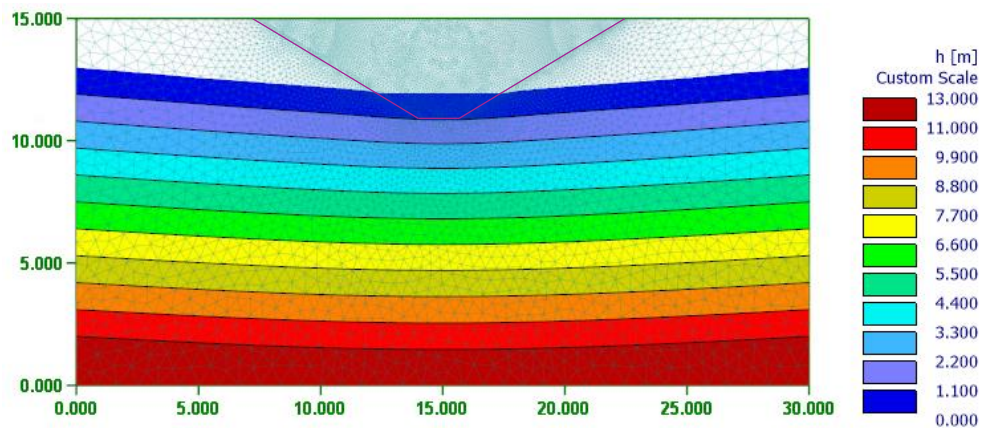
Figure 36. Section of a furrow - Results in terms of Pressure Head @48h.
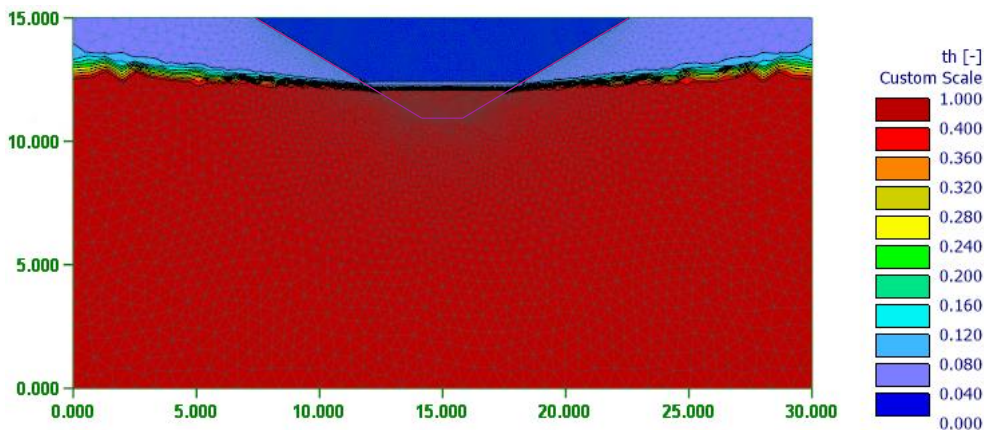
Figure 37. Section of a furrow - Results in terms of Water Content @48h.

44
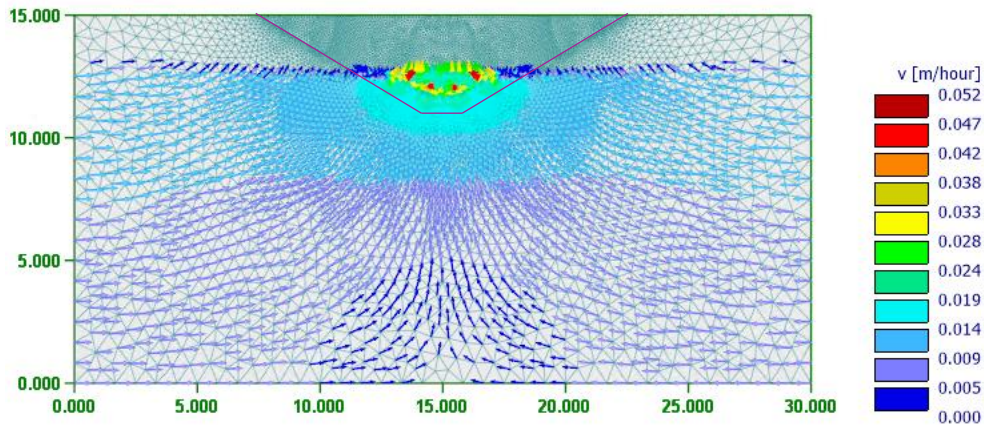
Figure 38. Section of a furrow - Results in terms of Velocity vectors @48h.

4.2.2 Section of the head

The second section explored is the head of the *fontanile*. In this case two configurations are considered: the first one representing just the excavated head of the *fontanile* (A) and the second one adding the *tubo calandra* (B) to evaluate whether its contribution is meaningful or not. After a careful evaluation, it was decided to represent the thickness of the screened structure of the *tubo calandra* by creating cavities in the domain, this way it was possible to set the no flux boundary condition at its walls to avoid any miscalculation.
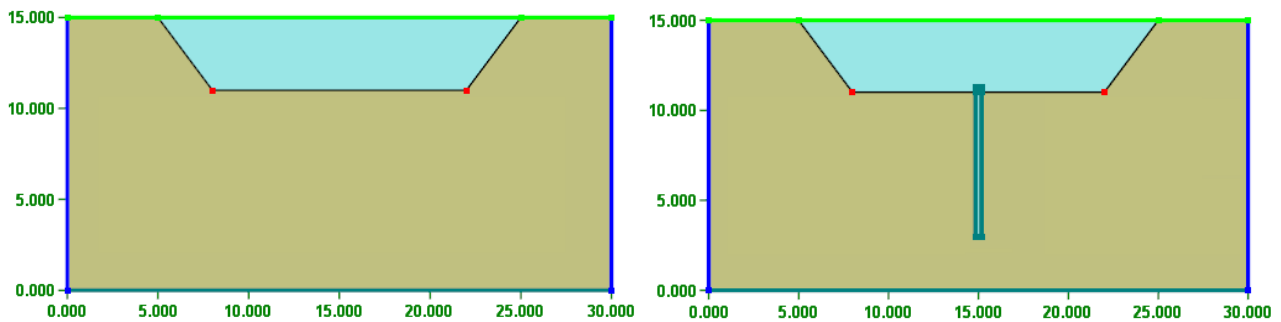
Figure 39. Geometry of the head of the fontanile in configuration (A) on the left and (B) on the right. B.C.: atmospheric in green; constant head in blue; no flux in teal.

The initial and boundary pressure head conditions at the sides of the domain for the two simulations are in common and correspond to 9 m and 11.75 m respectively. The mesh in configuration (A) has 7190 nodes, instead, case (B) has 7585 of them; instead, the largest dimension of the finite elements ranges from 0.15 m to 0.84 m in both cases. The results in transient conditions, at simulation time equal to 24 hours, are displayed below. Comparing the results of the pressure heads in the two configurations, it is clear that the use of the *tubo calandra* alters the isolines. As a matter of fact, h in the borehole is locally higher than the surroundings, see Figure 41. For this reason, the directions of the streamlines are tilted by its effect and the water flows upward along the hole and starts to fill the pond sooner than in the other scenario. Besides, the water velocities in the borehole are higher by an order of magnitude compared to the other case.
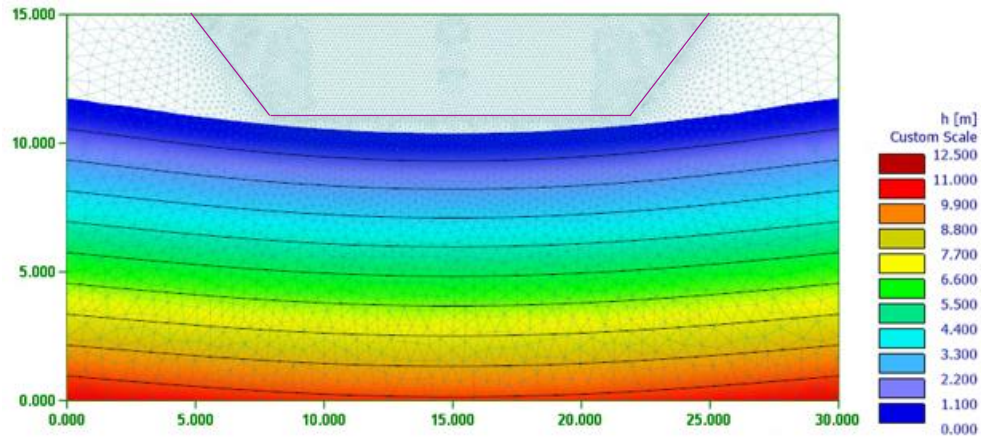
Figure 40. Section of the head (A) - Results in terms of Pressure Head @24h.
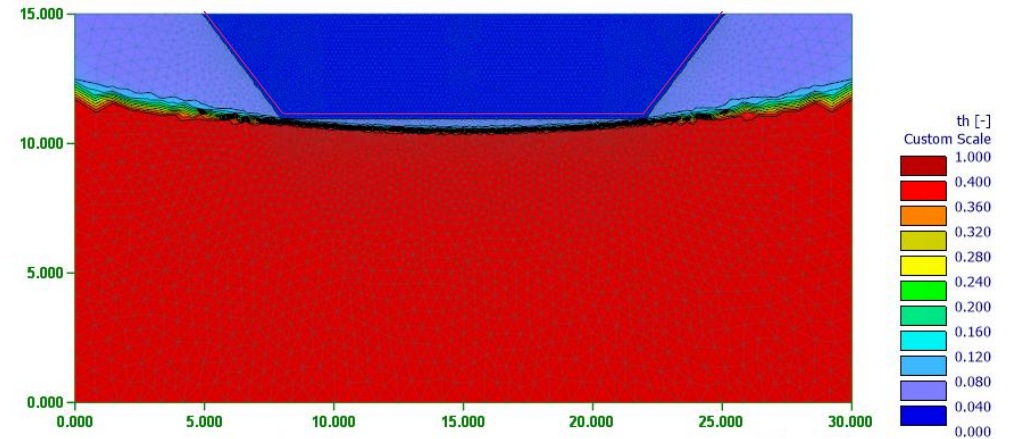
Figure 42. Section of the head (A) - Results in terms of Water Content @24h.
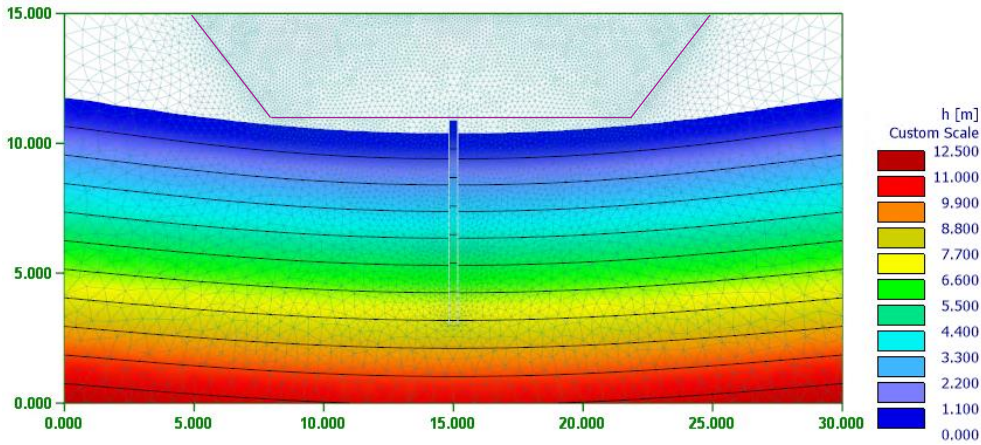
Figure 41. Section of the head (B) – Results in terms of Pressure Head @24h.
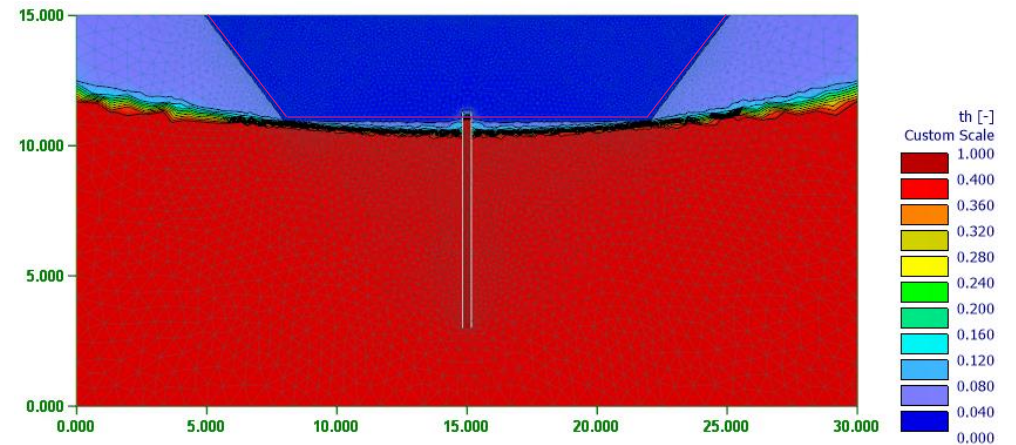
Figure 43. Section of the head (B) - Results in terms of Water Content @24h.
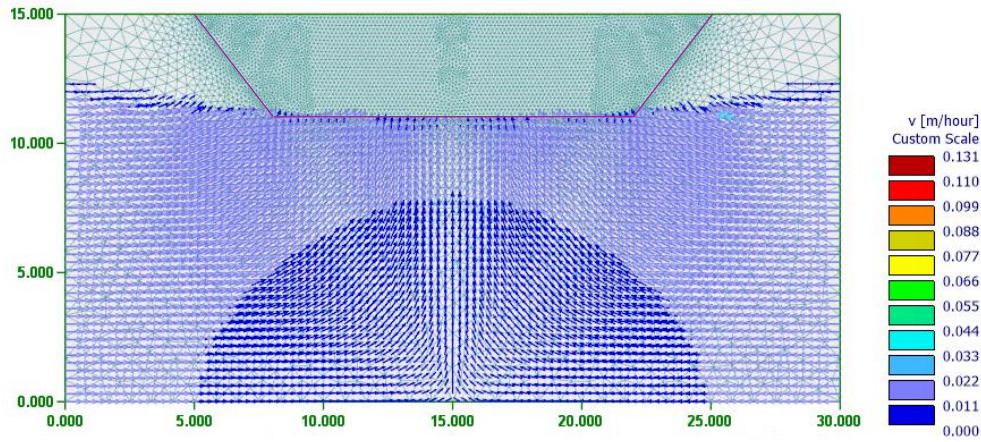
Figure 44. Section of the head (A) - Results in terms of Velocity vectors @24h.
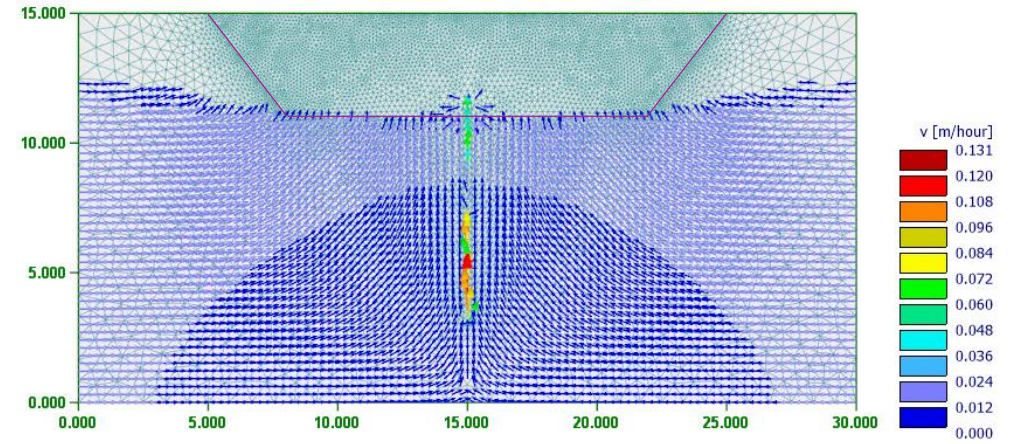
Figure 45. Section of the head (B)- Results in terms of Velocity vectors @24h.

More in detail, to investigate the contribution of the borehole, the same models were run under different values of constant head boundary condition. The length of the simulation was 168 h (7 days) to in order to allow the system to reach equilibrium in every configuration. With the help of the meshlines (represented in purple in the Figure below), the flux of water moving across the top of the borehole, if present, and at the base of the pond is evaluated.
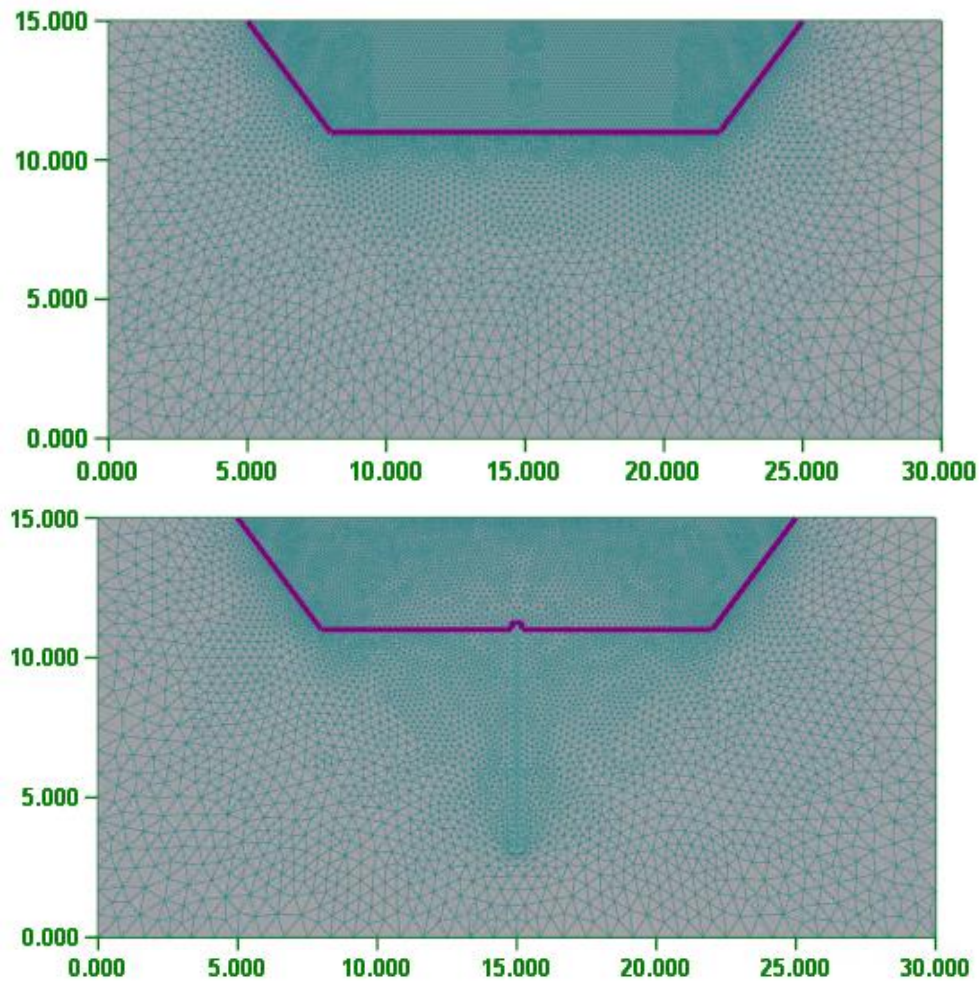
Figure 46. Meshlines for the computation of the fluxes for the geometry of the head of the fontanile in configurations A and B.

The total cumulated flux at the bottom of the furrow for each simulation, in both cases (A) and (B), is compared. It appears to be clear that the *tubo calandra* really makes the difference in those situations where the water table is lower, as it facilitates the flow, whereas, when the water table is shallower there is not a significant variation, as Figure 47 and Figure 48 show.
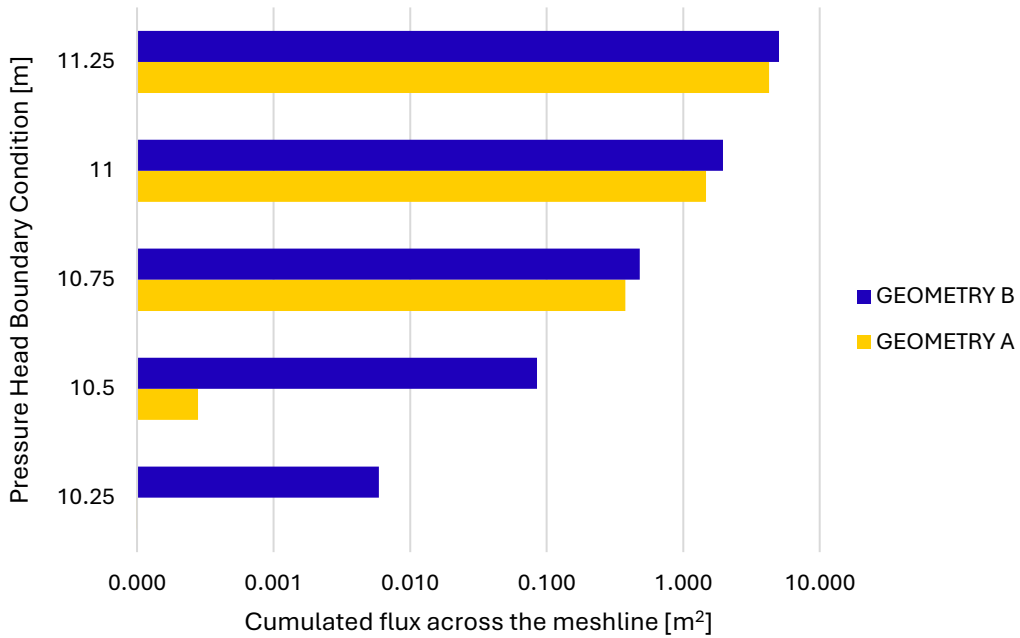
Figure 47. Comparison of the flux towards the furrow in the two configurations, with or without the borehole.
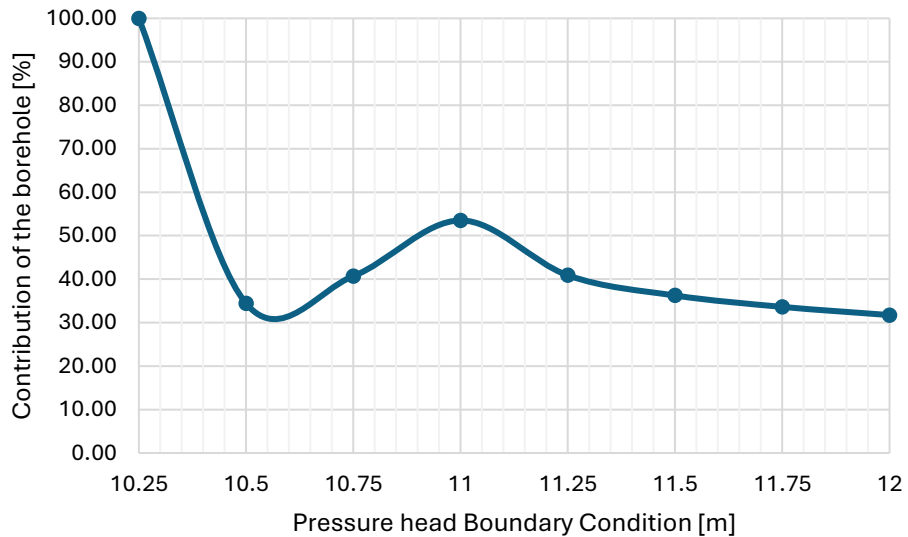
Figure 48. Contribution [%] of the borehole to the total flux toward the channel in geometry B, as function of the boundary condition. The variable is computed as the ratio of flux through the borehole with respect to the whole bottom of the furrow.

4.2.3 Sensitivity analysis

To deepen the focus on the peculiar use of the *tubo calandra,* it was decided to carry on a sensitivity analysis on the same geometry of the head of the fontanile, presented in Figure 39 b. In particular, the first aim was to assess the contribution the borehole to the total water flux toward the channel based on the grain size distribution of the soil. To this aim, the same flow simulation was performed for two different granulometric classes of the soil and the discrepancies of the two scenarios were evaluated. In this case the pressure head initial and the constant boundary conditions of the soil were set as 9 m and 11.75 m, respectively. The results in transient conditions for both loamy sand and sandy soils, at the simulation time 24 h, are presented below as water content and velocity vector fields. But the simulation time is again extended to 7 days so the system can reach equilibrium, to ease the comparison of the fluxes between the two cases.

The results show that in case of a less conductive soil, such as loamy sand, the water is encouraged to flow within the borehole, as it encounters lower hydraulic losses. Here, the water content reaches its maximum at the base of the furrow sooner compared to the surroundings. Instead, in the case of a more conductive soil, such as sand, the contribution of the borehole does not play a key role for a long time, as the whole water table is rapidly shifting upwards, see Figure 50. Accordingly, the permeability of the sand allows the *tubo calandra* to welcome a higher flux (Figure 52) but, on top of this, for the same simulation time, the vectors of the velocity are already moving around the cross-section of the pond, whereas in the case of loamy sand they are still below the bottom of the head and only a few of them are poking out of the top of the borehole.

This aspect is confirmed by the results of the water fluxes crossing the meshlines at the base of the head of the *fontanile*, represented in Figure 53 and Figure 54. As a matter of fact, in the case of a sandy soil, the flux at the meshline starts about 10 hours earlier and reaches a maximum of 0.368 m^2/h, which is almost double the amount for loamy sand. Furthermore, the contribution of the *tubo calandra,* compared to the whole flux, in the first 24 hours is on average at about 45% in the case of loamy sand and 36 % for the sandy soil, but its impact, in both cases, suddenly drops when the water table is as shallow as the bed of the furrow.

As a result, one can conclude that not only the contribution of the screened hole is negligible for shallow depth to groundwater, as stated previously, but also when the soil is highly conductive, because the pressure head difference between the top of the *tubo calandra* and its surroundings is modest.
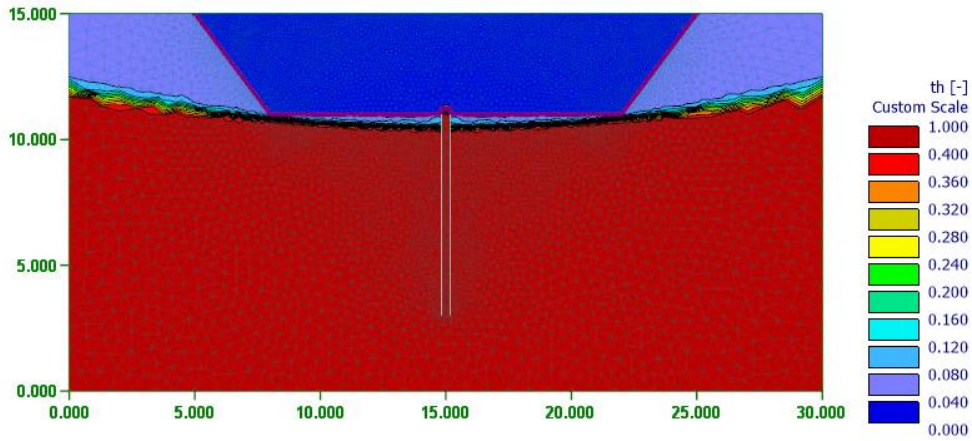
Figure 49. Sensitivity analysis - Results in terms of Water Content for loamy sand soil @24h.
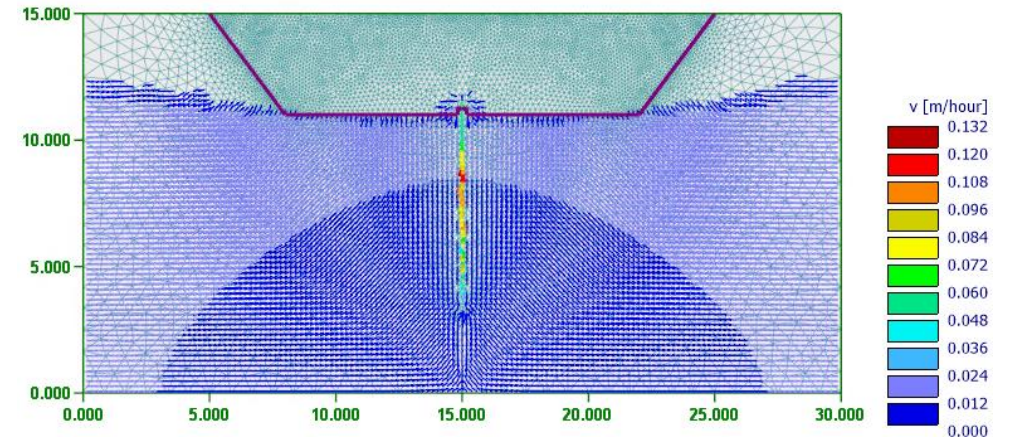
Figure 51. Sensitivity analysis - Results in terms of Velocity vectors for loamy sand soil @24h.
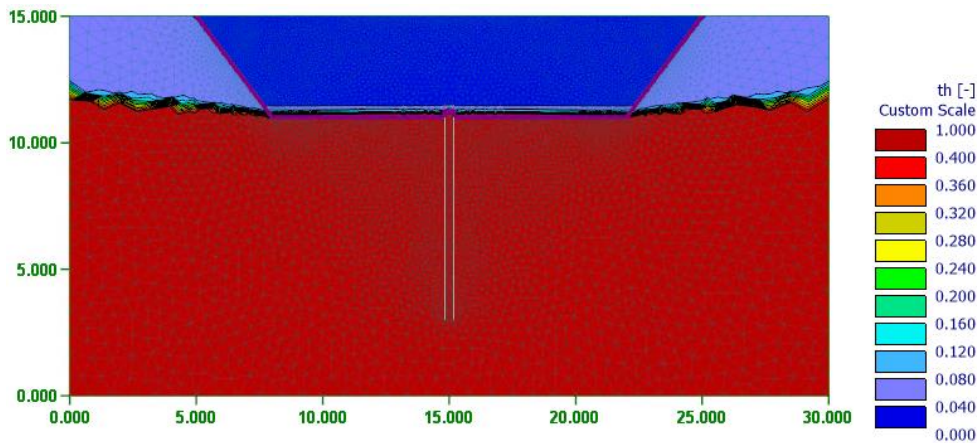
Figure 50. Sensitivity analysis - Results in terms of Water Content for sandy soil @24h.
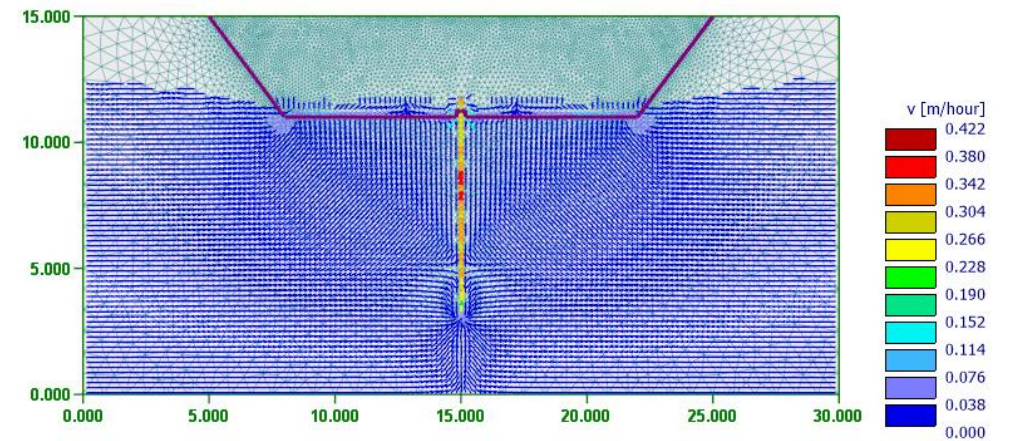
Figure 52. Sensitivity analysis - Results in terms of Velocity vectors for sandy soil @24h.
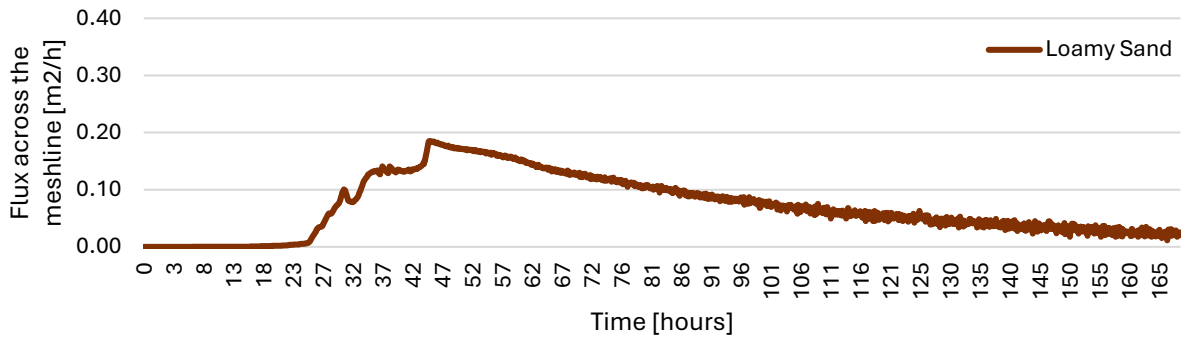
Figure 53. Sensitivity analysis - flux across the meshline for a loamy sand soil in transient conditions.
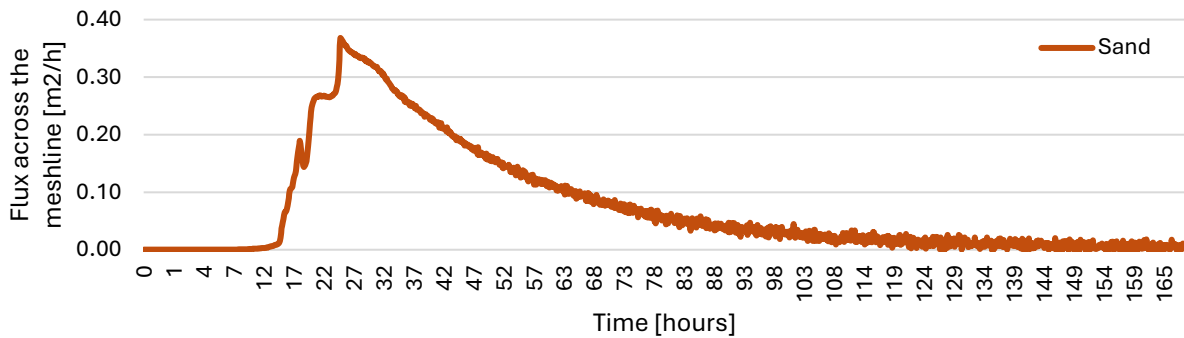
Figure 54. Sensitivity analysis - flux across the meshline for a sandy soil in transient conditions.

For the reasons cited above, the sensitivity analysis is expanded to give an idea of the pressure head field, within and outside of the *tubo calandra,* under different scenarios of porosity and hydraulic conductivity. The creation of observation points around the domain serves very well this purpose; in particular, three pairs of nodes were selected: one close to the lateral boundary of the domain, one just outside the borehole and one along its axis. Note that the observation nodes are located either at 4.5 or 7.5 m from the bottom of the aquifer, as shown in Figure 55.
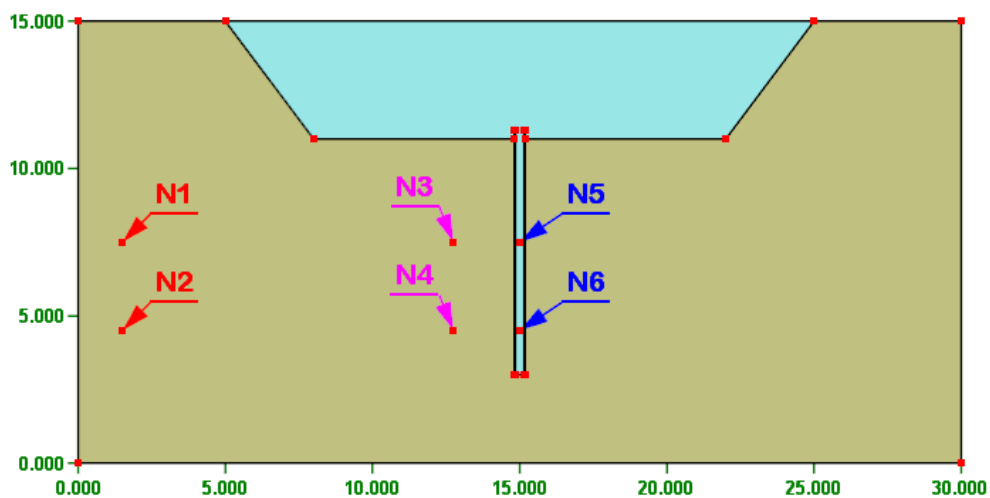
Figure 55. Observation nodes for the geometry of the head of the fontanile with the tubo calandra. The three pairs are represented with different colors.

A first simulation is run keeping the default soil hydraulic parameters of the loamy sand, refer again to Table 3, instead, the variable head boundary conditions applied at the lateral limits of the domain are listed in Table 5. It is expected that at equilibrium conditions the pressure head difference between the two nodes of each pair coincides with 3 m, but in transient conditions, as those shown above, there is a variation of this variable around the domain, causing the preferential flux through the borehole. This is demonstrated thanks to the evaluation of the pressure head difference (ΔP) for all the three pairs as function of the simulation time, displayed in Figure 56.

Table 5. Sensitivity analysis - Variable Head B.C. Schedule.

Time [hours]	3	5	8	12	17	48
Var. Head [m]	9	9.5	10	10.5	11	11.75
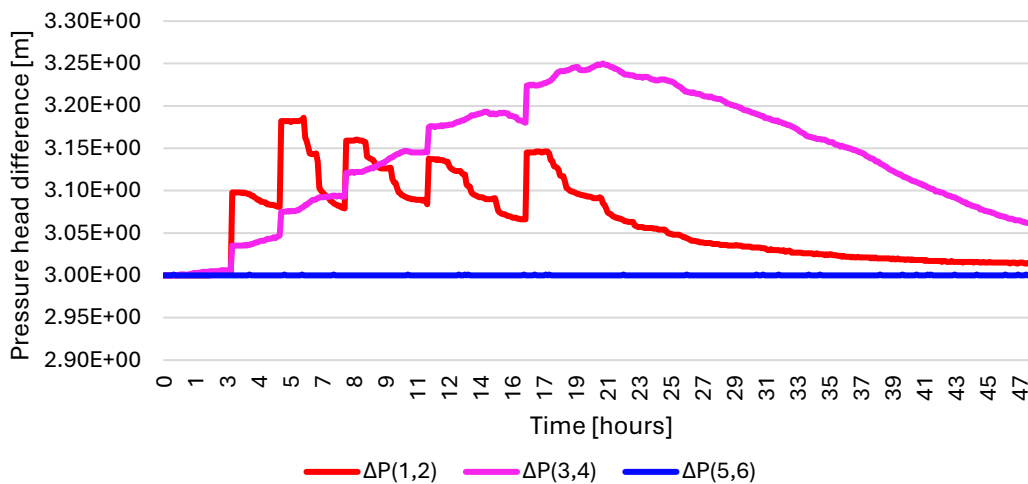
Figure 56. Sensitivity analysis - Results of the pressure head difference for the three pairs of observation nodes in transient conditions. The color scheme refers to Figure 55.

The results show that the closer the pair is to the lateral limits of the domain, where the boundary conditions are applied (Table 5), the stronger will be the alteration of the ΔP between the observation nodes. In particular, the pair of points N1 and N2 reflects strongly the B.C. schedule, instead, the N3 and N4 have a smoother response. Nodes N5 and N6, located within the borehole, are not significantly affected by this event because the connection of the *tubo calandra* to the unconfined aquifer is located at a great depth (around 3 m from the aquifer bottom), where the soil is always at saturation; therefore, the hydrostatic profile is preserved within the walls. Consequently, during transient conditions it is possible that the pressure head is higher in the *tubo calandra,* as in the previous examples. At this point, by changing the values of hydraulic conductivity and porosity it is possible to understand when this scenario is more likely to occur. The values tested during the simulations were:

- Porosity
  a. 0.30
  b. 0.35
  c. 0.41

- Saturated hydaulic conductivity (Ksat):
    d. K= 0,01459 m/h (4 10^{-6} m/s)
    e. K= 0,08025 m/h (2 10^{-5} m/s)
    f. K= 0,14592 m/h (4 10^{-5} m/s)
    g. K= 0,80254 m/h (2 10^{-4} m/s)
    h. K= 1,45917 m/h (4 10^{-4} m/s)

The values highlighted in bold correspond to the default soil hydraulic properties of the loamy sand (Table 3). The results show that the sensitivity of the pressure head response to changes in porosity is pretty much negligible, see Figure 57.
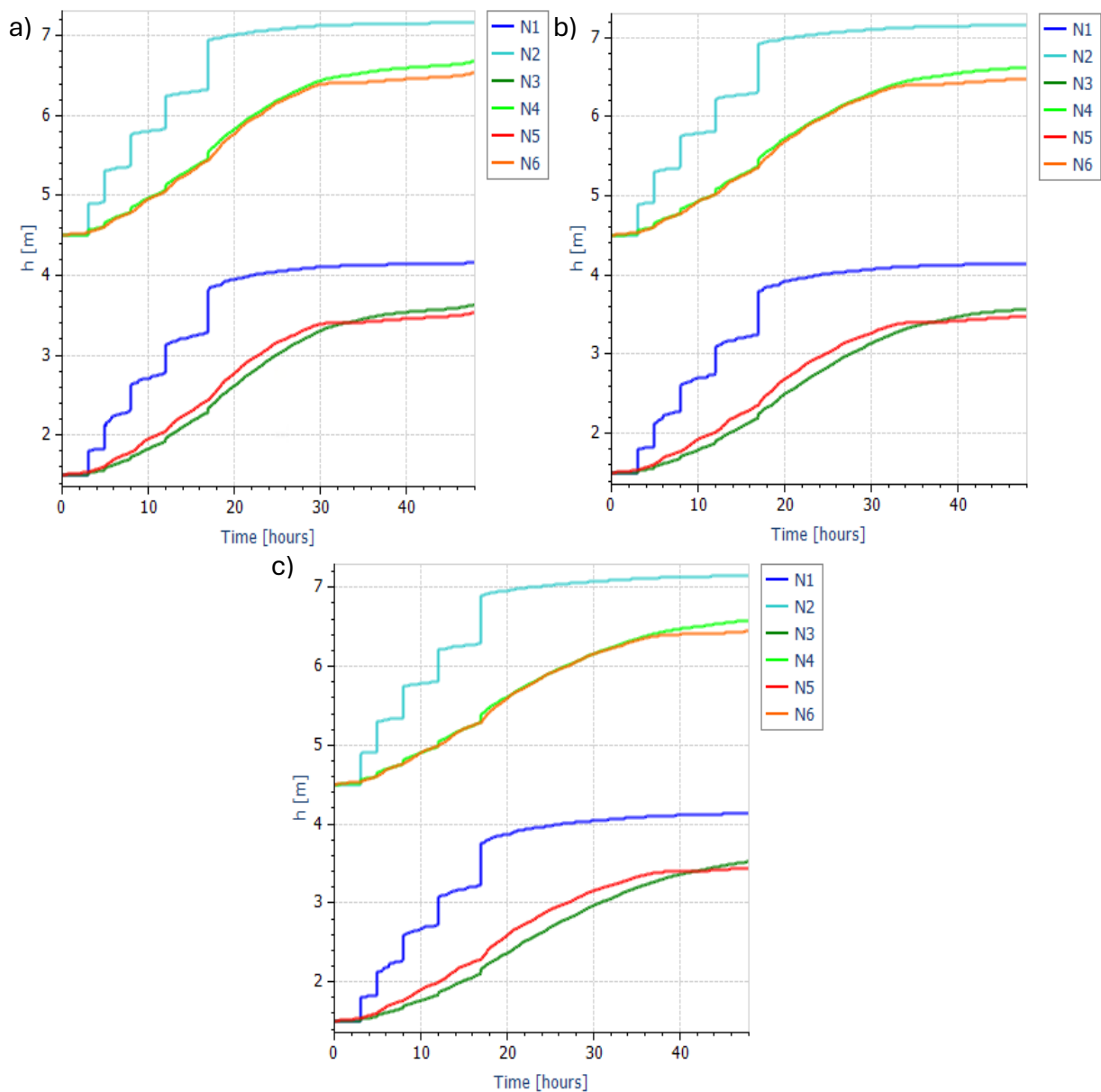
Figure 57. Sensitivity analysis - Pressure Head at the observation nodes in the 3 porosity scenarios (a-c).
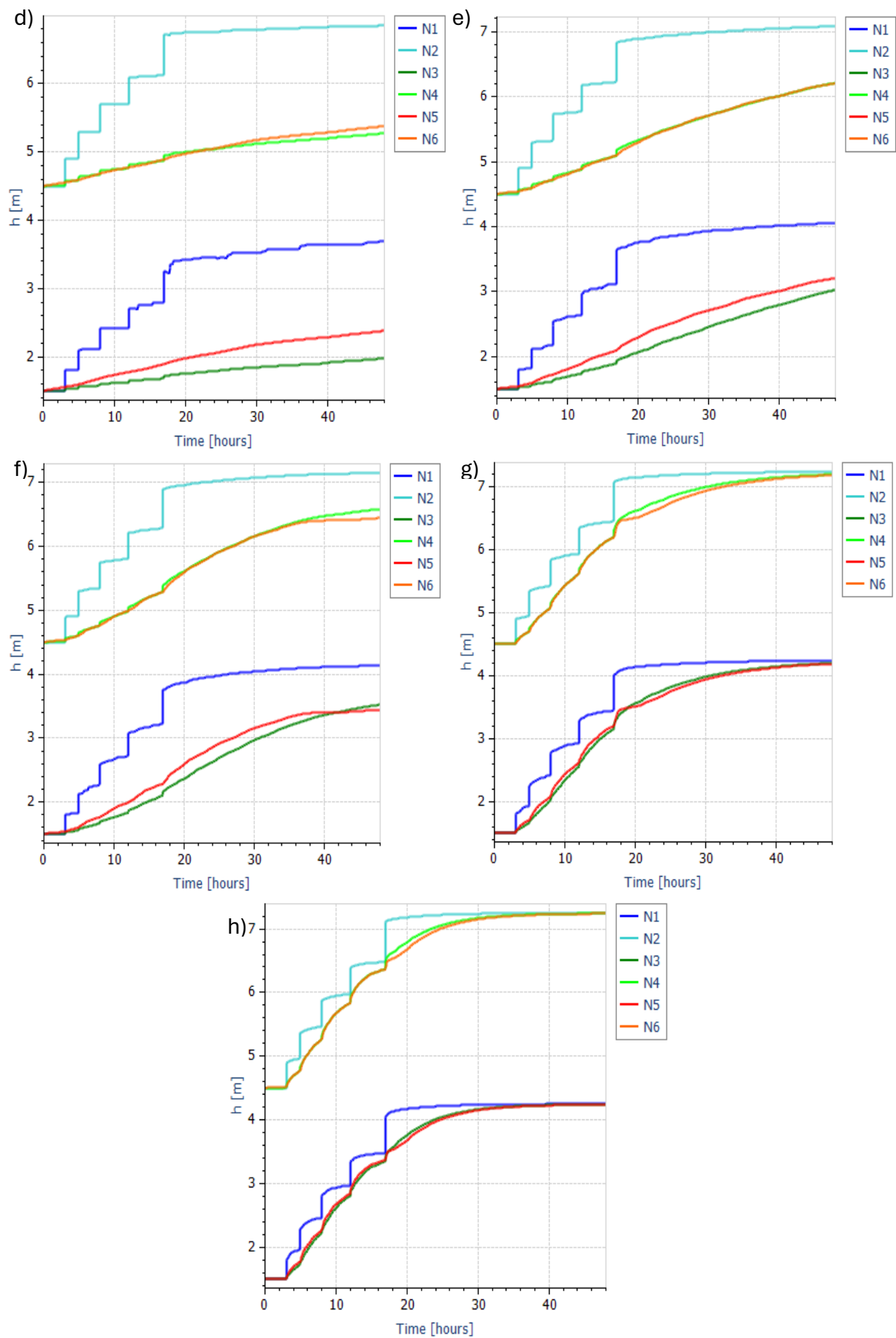
Figure 58. Sensitivity analysis – Pressure Head at the observation nodes in the 5 Ksat scenarios (d-h).

On the contrary, the results shown in Figure 58 confirm what had been previously stated: higher the conductivity of the soil, lower the pressure head difference between the nodes in the borehole and those at its outskirts, therefore lower the contribution of the *tubo calandra*. In particular, the curves of the nodes N3 to N6 in the cases g) and h), where the order of magnitude of Ksat is 10^{-4} m/s, overlap, meaning that this value of Ksat can be considered as an upper limit for the functionality of the configuration with the *tubo calandra*. In contrast, cases f), e) and d) are – in ascending order - particularly suitable for the installation of such infrastructure, as these values of Ksat, in the order of magnitude from 10^{-5} to 10^{-6} m/s, enhance the pressure head difference between the inside and outside of the borehole.

Furthermore, for each one of these simulations, also the fluxes at the meshline at the bed of the furrow were retrieved and they are displayed in the graph below. On one hand, one can notice that the cases a to c, where the sensitivity to the porosity was checked, do not show a significant variation in the magnitude of the flux at the head of the *fontanile,* indeed, only a small retardation effect is present. On the other hand, the different orders of magnitude of hydraulic conductivity (K) cause important changes: when K is reduced, the peak of the flux decreases and the whole curve is significantly shifted later in time; instead, the increase of K by an order of magnitude (case h) makes the flux peak at one order of magnitude above the reference curve of the loamy sand (curve c/f). Once again, it was proved that the key parameter in the configuration of the *fontanili* is the hydraulic conductivity.
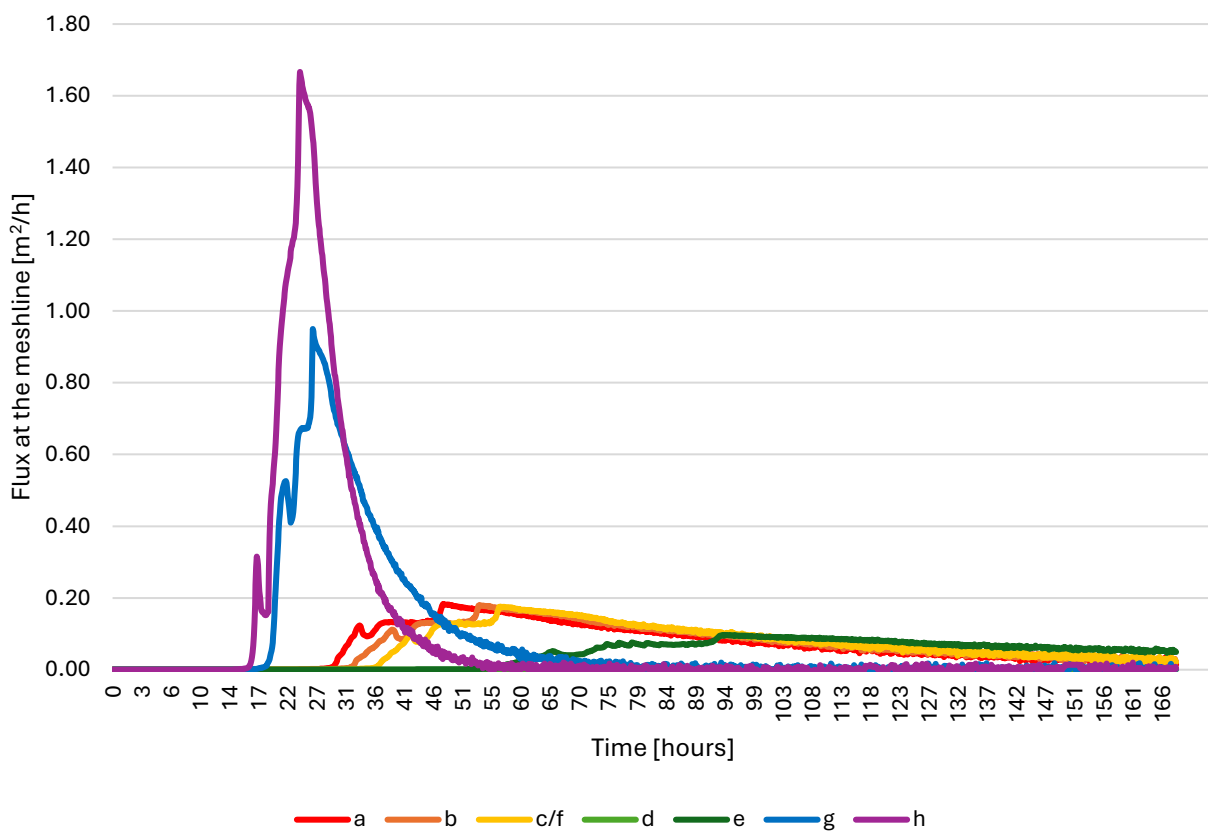
Figure 59. Fluxes at the meshline at the bed of the furrow in configurations (a-h)

4.2.4 Profile of the fontanile

Finally, one last 2D section of the *fontanile* is presented: the longitudinal profile. The geometry includes both the head and the channel, as well as multiple *tubi calandra* located along the furrow. The mesh involves 15161 nodes and the finite elements range from 0.2 m to 1.3 m in width. The atmospheric boundary condition is imposed above the channel, no flux is assigned to the bottom of the aquifer and at the walls of the boreholes; the head boundary conditions are set upstream and downstream, instead, the cross-sections of the furrow are represented as seepage faces to allow the modelling of the surface flow at the lateral boundaries of the domain.
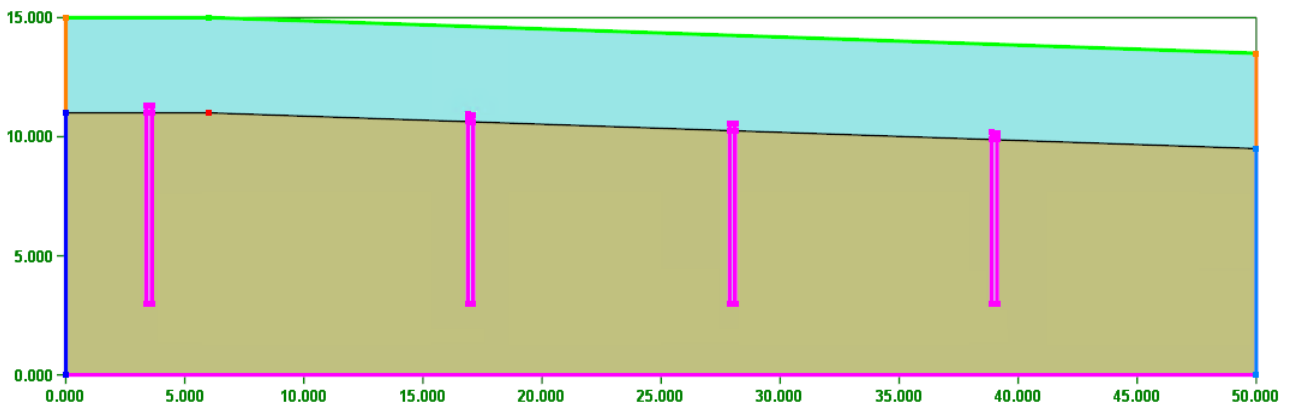
Figure 60. Geometry of the longitudinal profile of the fontanile. B.C.: atmospheric (in green); seepage face (in orange); pressure head (in dark and light blue); no flux (in magenta).
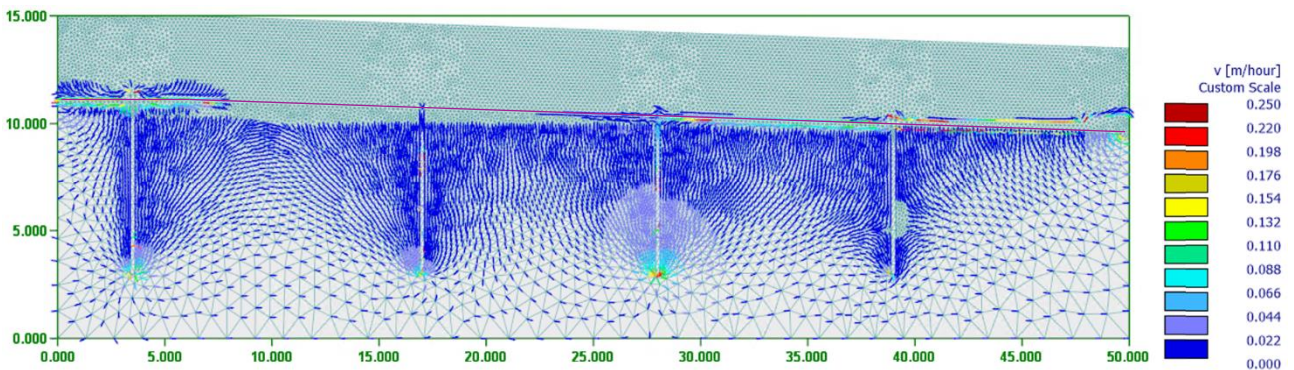
Figure 61. Profile section of the fontanile - Results in terms of Velocity vectors

The results in terms of velocity vectors are represented above. From this simulation it is clear that this geometry is suitable to represent the general behavior of the *fontanile* but not to model the effect of the *tubo calandra,* which does not stand out because of the lack of constraints coming from the third dimension. Consequently, the numerical modelling is further developed using a 3D geometry.

4.2.5 3D Portion of the furrow

The 3D geometry modelled represents a portion of the furrow with a *tubo calandra* centered along the channel. For strictly computational reasons the domain is confined to 15 m in depth, 10 m in length along the furrow and 30 m in width. In order to get a valuable representation, along the flow direction, both the ground level and the base of the furrow experience a lowering of about 1 m, whereas, the water table experiences a lowering of about 0.25 m of pressure head (Figure 62). The mesh includes over 380000 discretization solids with a homogeneous width of 0.3 m. Also in this configuration the two materials, sandy soil and water are used but, due to the difficulty in the creation of hollow cylinders to represent the walls of the borehole, a third one had to be introduced. The latter mimics an impermeable material by imposing a hydraulic conductivity that tends to zero (refer to Table 6).
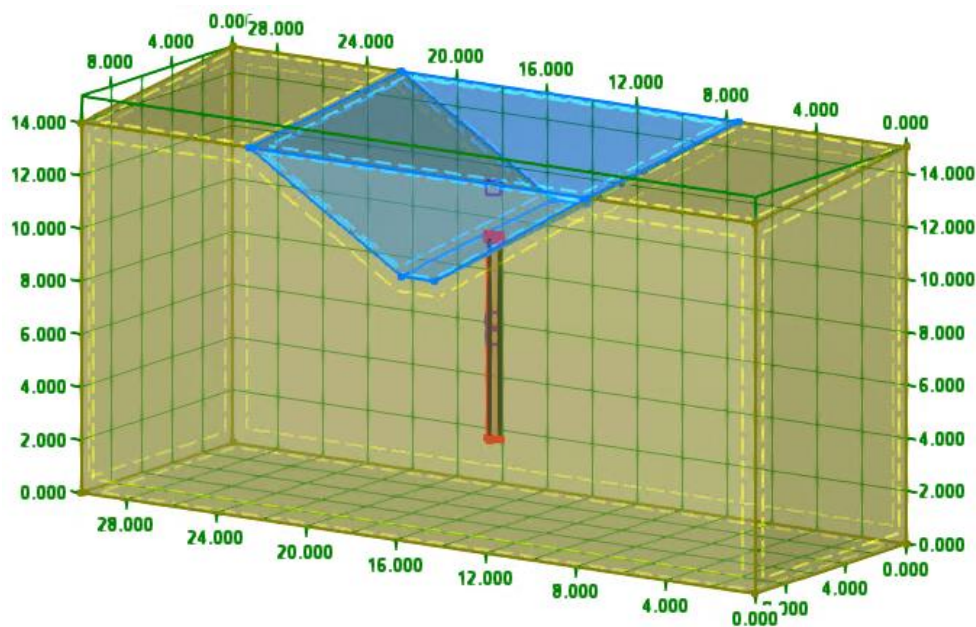
Figure 62. Geometry of the 3D portion of the furrow (fontanile). The loamy sand soil is represented in beige, the water in blue and the impermeable holes of the borehole in red.

Table 6. Materials for the simulations: Loamy Sand, Water and Impermeable material for the walls of the borehole. Qr and Qs are respectively residual and saturated soil water content; α and n are parameters in the soil-water retention function; Ks is the saturated hydraulic conductivity; I is a tortuosity parameter in the conductivity function.

Mat	Name	Qr [-]	Qs [-]	Alpha [1/m]	n [-]	Ks [m/hour]	I [-]
1	Loamy Sand	0.057	0.41	12.4	2.28	0.145917	0.5
2	Water	0	1	14.5	2.68	1e+06	0.5
3	Impermeable walls	0	0	14.5	2.68	1e-06	0.5

The boundary conditions in this case are applied not to segments of the edged of the domain, instead, they are assigned to surfaces, see Figure 63. The ground level and the top of the channel have an atmospheric b.c.; the downstream cross-section of the furrow is a seepage face to allow the flow to pass through; pressure head b.c. are set at the upstream and

downstream surfaces of the soil; finally, a no flux b.c. constraints the bottom of the aquifer and the lateral surfaces, as these can be considered parallel to the main water flow direction.
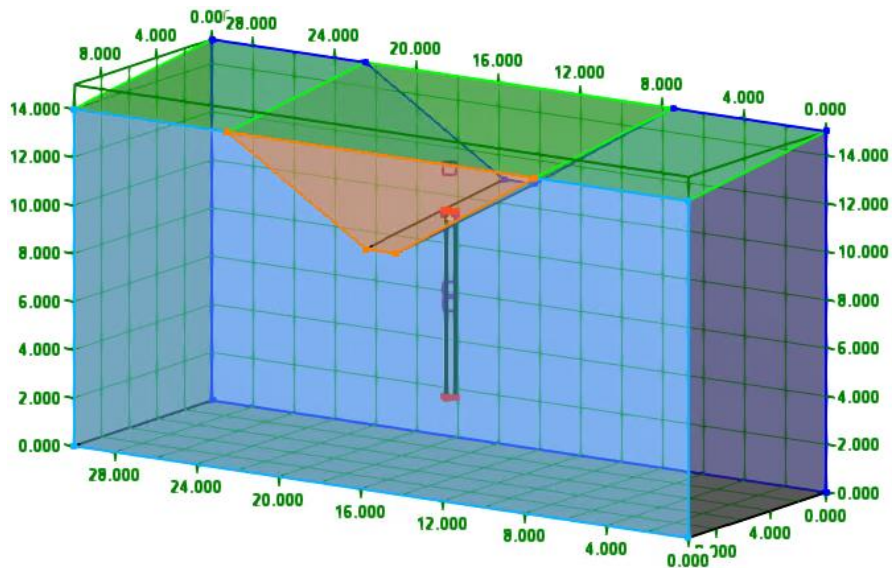
Figure 63. Boundary Conditions for the 3D portion of the furrow: atmospheric (in green), seepage face (in orange), pressure head b.c. (in dark and light blue), no flux (in black).

The simulation was launched in several scenarios of pressure head boundary conditions and the flux [m³/h] at the seepage face was retrieved. The simulation time was calibrated each time to allow the system to reach a steady state flow. With this information, a relationship between the level of the water table and the steady state flux at the cross-section of the furrow was established by fitting the graph below: $Q(h) = 10^{-5}\exp{(1.007h_{b.c.})}$, with $R^2 = 0.9016$.
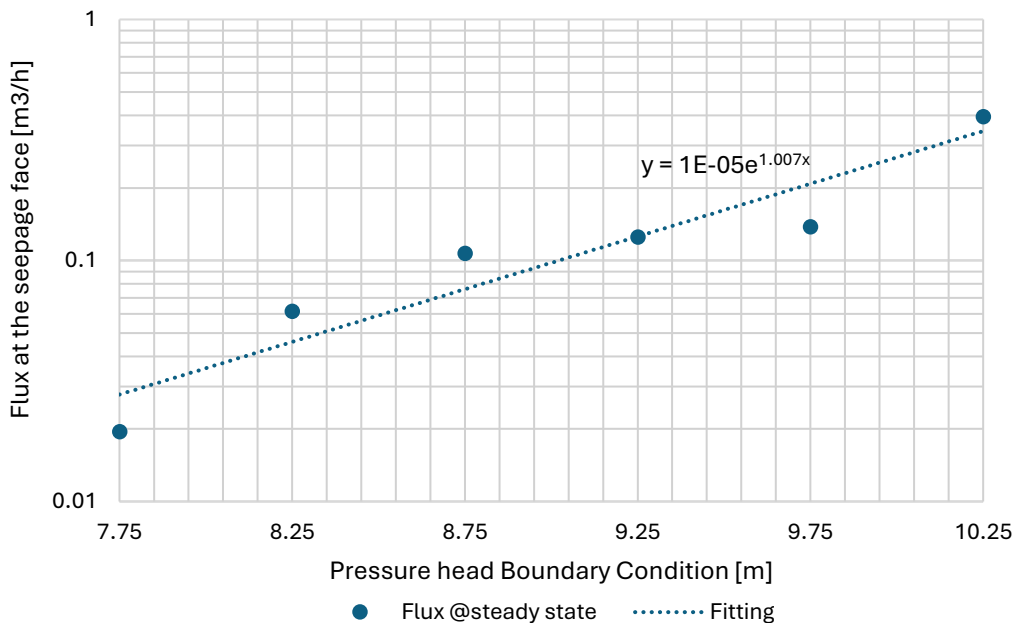
Figure 64. Steady state flux at the seepage face (cross-section of the furrow) as a function of the pressure head boundary conditions.

In the next images, the results in terms of velocity vectors are displayed.
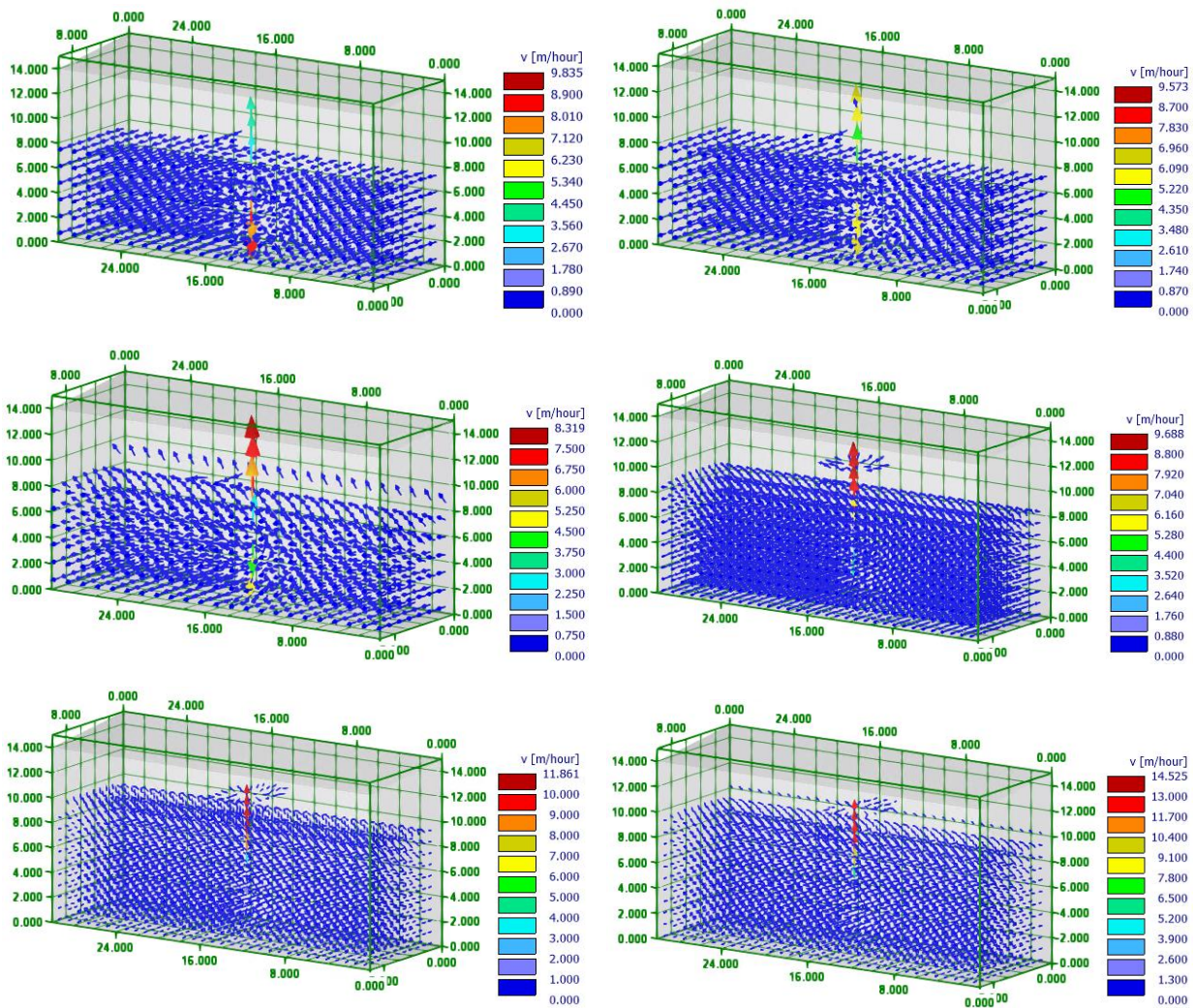
Figure 65. 3D Portion of the furrow - Results in terms of velocity vectors. From the upper left corner to the bottom right the pressure head b.c. was set as: 7.75 m; 8.25 m; 8.75 m; 9.25 m; 9.75 m; 10.25 m. Notice that the color scale is adapted to the maximum velocities reached in each configuration.

Figure 65 allows to compare the flow distribution in the different configurations. It is clear that by increasing the value of the pressure head boundary condition the velocity in the *tubo calandra* grows, as a matter of fact it ranges form about 9 m/hour to over 14 m/hour. Moreover, in transient conditions, the flux coming from the borehole starts to fill the channel progressively with the lowering of the depth to groundwater. In the last three configurations the water fills the furrow and flows downstream along the third dimension, in agreement with the slope of the ground level.

4.3 Conceptual Model: MAR

Since the resilience of water systems is particularly challenging and often requires a holistic approach where multiple strategies, such as the conjunctive management of surface and groundwater, are integrated (Scanlon et al., 2023) a possible adaptation solution is represented by Managed Aquifer Recharge. MAR is the purposeful injection of water into aquifers for subsequent recovery or for mere environmental benefit, such as sustaining ecosystems or contrasting salt-water intrusion in coastal areas. The water eventually recovered can be, then, used for civil or industrial purposes, as well as irrigation. MAR offers a tool to decrease the anthropic pressure on the subsurface systems by restoring part of the uptakes during seasons of higher water abundance or lower water demand. As a matter of fact, aquifer systems can potentially store significant volumes as the flow velocities in aquifers are much smaller compared to those of the surface water bodies. Moreover, their connections to surface streams, such as the *fontanili* in Morozzo, can simplify the creation of a synergic network where water is injected and recovered in the proximity of agricultural fields, exploiting the existing infrastructure. Hence, this technology is particularly suitable for the study case presented. The benefits coming from MAR are acknowledged also by the EU, that in the WFD provides guidelines for its implementation; Article 11 (3f) states: "The water used may be derived from any surface water or groundwater, provided that the use of the source does not compromise the achievement of the environmental objectives established for the source or the recharged or augmented body of groundwater. These controls shall be periodically reviewed and, where necessary, updated" (*Water Framework Directive (WFD) 2000/60/EC*, 2000). The injection method in MAR sites is either infiltration or direct injection. In the first case, the water flow is gravity-driven towards the shallow unconfined aquifer and usually ponds, basins or dams are used to collect the water. This method is usually of easier implementation and the low velocities allow for an increase in water quality, as this gets treated along its path, but, on the other hand, the basins increase the land consumption. In the second case, wells are employed and the water is pumped down the borehole, facilitating the injection in less conductive soils Figure 66.
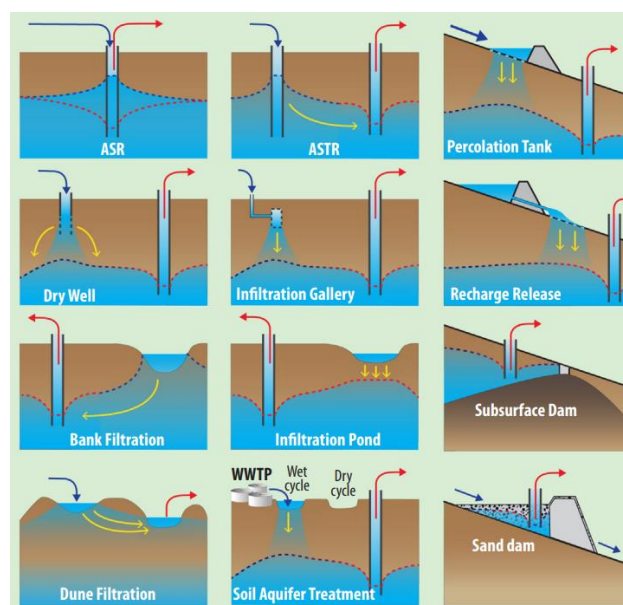
Figure 66. Representation of different MAR injection methods. Source: (Alam et al., 2021).

The pilot MAR site in the study area is going to be located in Tetti Pesio, within the municipality of Cuneo, upstream of the *fontanili* in Morozzo. Here the soil is highly conductive (K=$10^{-3} \div 10^{-4}$ m/s) and an irrigation channel is already available, so the water dedicated to the injection site can be diverted from it. The MAR infrastructure consists of a gravity driven infiltration trench, constituted by a screened pipe and fed by the discharge coming from the diversion. The project involves also a backup lamination tank that, in case of saturation of the system, will fill up and return the water back to the main irrigation channel, see Figure 67.
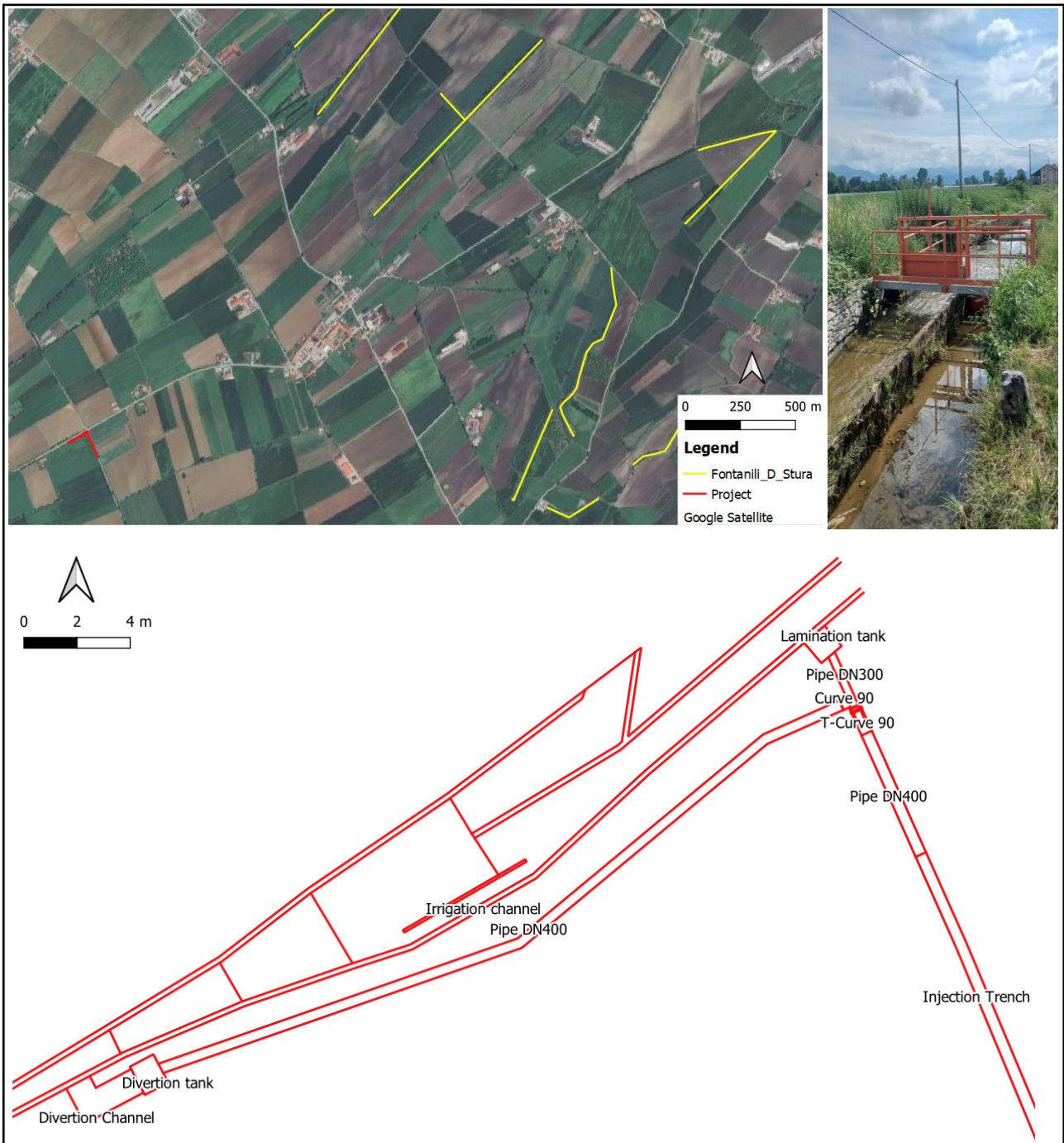
Figure 67. Project of the MAR site. On top a map of the area including the location of the MAR site (in red) and multiple fontanili (in yellow); on the right a picture of the existing irrigation channel from where the water will be diverted; at the bottom the design of the injection trench. Credits: Studio Pellerito Acqui Terme (Studio PD s.r.l.).

4.3.1 Injection Trench 2D

To begin with, the influence of the injection trench on the shallow unconfined aquifer is investigated. The geometry involves a homogeneous soil 1000 meters wide and 15 meters deep, see Figure 68. The trench is assimilated as a 100 m long segment forced by a flux boundary condition and is located at the top of the domain. The impermeable boundary condition is attributed to the bottom of the aquifer and the lateral edges of the domain, instead, the interface with the ground level is expressed as an atmospheric boundary. The mesh involves 25271 nodes, with the mesh elements being more refined towards the injection segment, indeed they range from 0.5 m to 1 m in width. Initially the depth to groundwater is set at 7 m below the ground level. Each simulation lasts 48 hours.
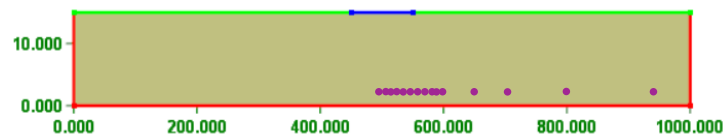
Figure 68. Injection Trench 2D - Geometry and B.C.: no flux in red, atmospheric in green and variable flux in blue. Note that the view is stretched to help the visualization. The purple dots are the observation nodes.

In particular, three configurations are simulated using different values of saturated hydraulic conductivity in the soil, leading to the cases:

    A) $K=10^{-3}$ m/s
    B) $K=10^{-4}$ m/s
    C) $K=10^{-5}$ m/s

In particular, the retention curves of hydraulic conductivity as a function of water content for the three cases (A, B, C) are made available by the software. M1 and M2 are gravel and sand, respectively. It is clear that the behavior is preserved but the curves are shifted: the lowering of Ksat by an order of magnitude translates downward the curves.
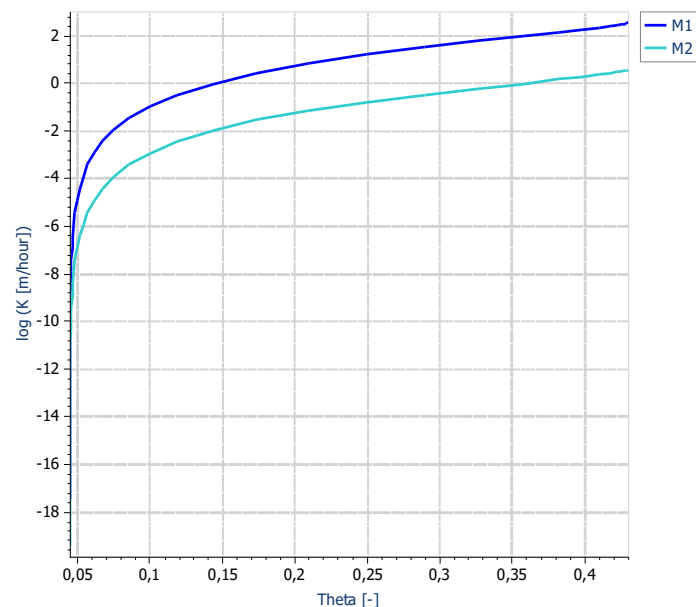
Figure 69. Injection Trench 3D - Retention curve with Ksat = 10^{-3} m/s.
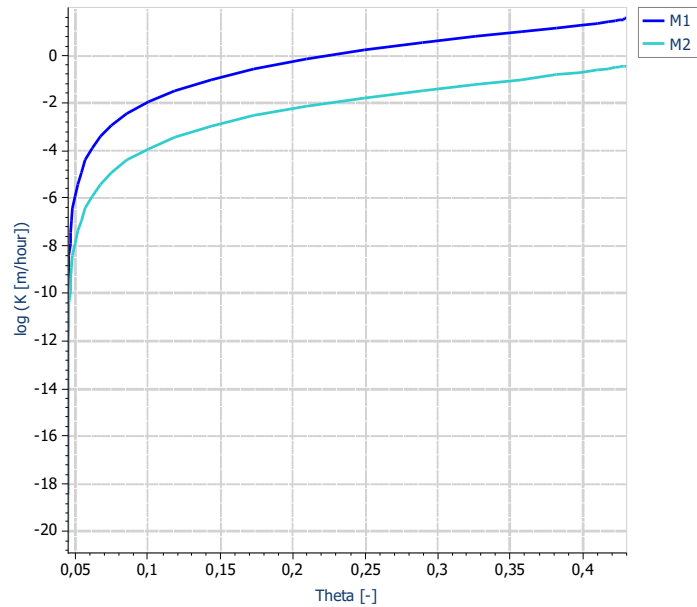
Figure 70. Injection Trench 3D - Retention curve with Ksat = 10^{-4} m/s
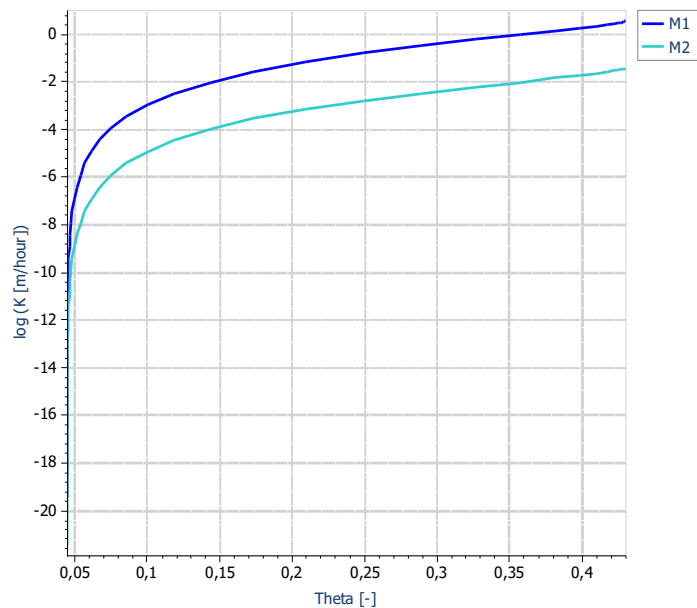
Figure 71. Injection Trench 3D - Retention curve with Ksat = 10^{-5} m/s

Instead, as far as the variable flux boundary condition is concerned, two scenarios are considered: the first corresponding to an infiltration discharge in the MAR site in the order of magnitude of 10^0 l/s, the second of 10^1 l/s. By means of a simple dimensional analysis and indicative orders of magnitude of the variables, the flux boundary conditions are retrieved in [mm/h], as required by the software. They correspond to 10^1 mm/hour and 10^2 mm/hour. Besides, these values are in agreement with those reported by FAO, which suggest an infiltration capacity in sandy soils in the order of $10^1 \div 10^2$ mm/h (FAO et al., 1990).

Starting from here, for numerical reasons, the flux boundary condition has to be built up gradually, as shown in Table 7.

	Case 1					Case 2				
Time [hours]	1	3	5	6	48	1	3	5	6	48
Flux [m/h]	-0.005	-0.010	-0.025	-0.050	-0.050	-0.010	-0.025	-0.05	-0.1	-0.1

Therefore, from the combination of the three values of conductivity and two scenarios of variable flux boundary conditions 6 cases are analyzed. Furthermore, 15 observation nodes were placed along the mesh to retrieve the increase in pressure head along the horizontal direction. The graphical results in terms of water content are displayed below.
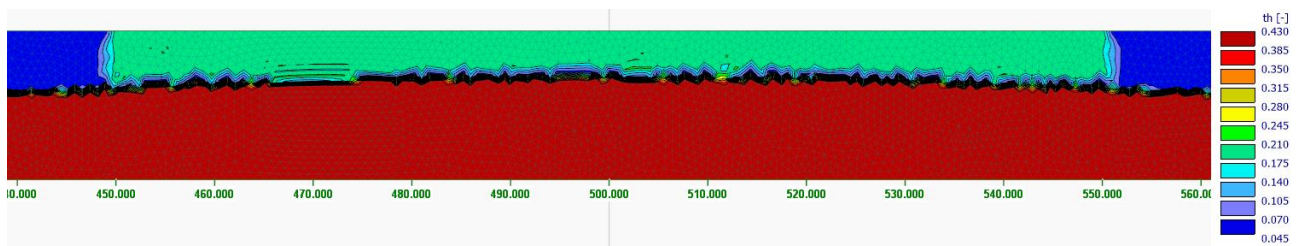
Figure 72. Injection Trench 2D - Case A1 Results (Water Content) @48h.
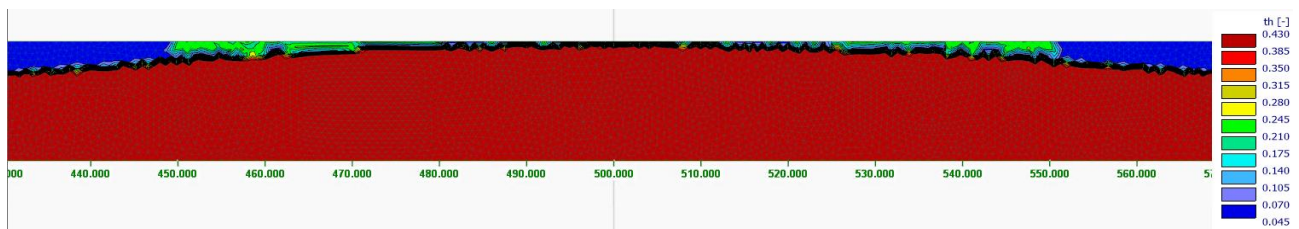
Figure 73. Injection Trench 2D - Case A2 Results (Water Content) @48h.
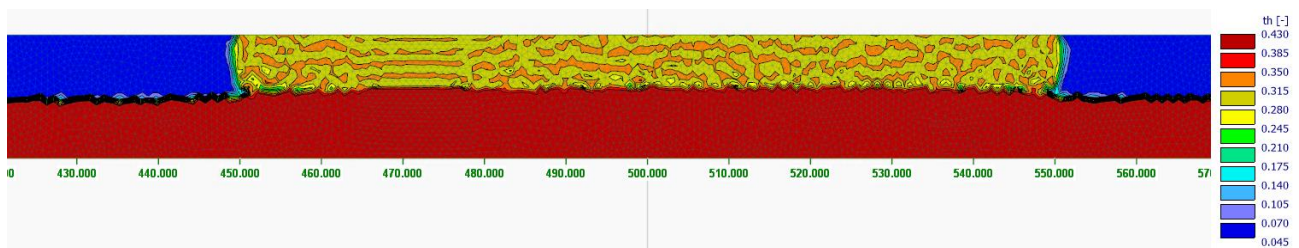
Figure 74. Injection Trench 2D - Case B1 Results (Water Content) @48h.

Figure 75. Injection Trench 2D - Case B2 Results (Water Content) @48h.
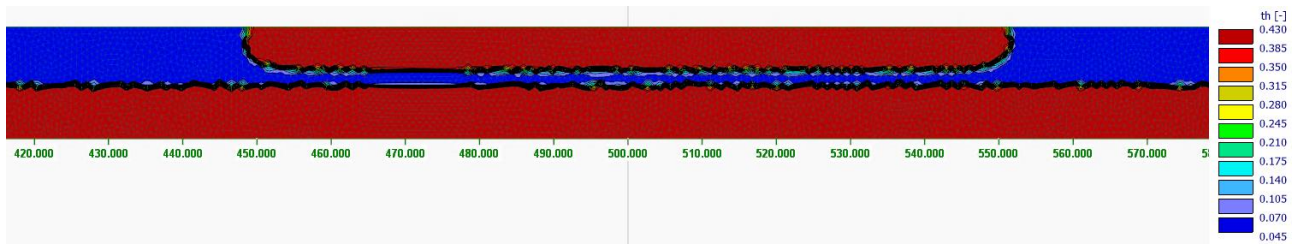
Figure 76. Injection Trench 2D - Case C1 Results (Water Content) @48h. Note that in this case the system does not reach steady state conditions.
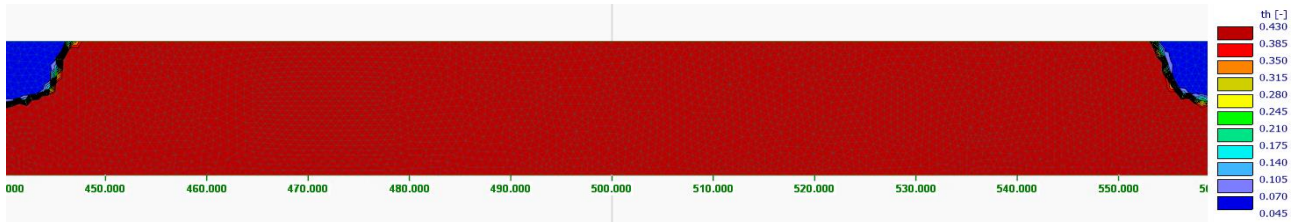
Figure 77. Injection Trench 2D - Case C2 Results (Water Content) @38h. Note that the numerical solution is interrupted because the system does not converge after 38 hours.

A few considerations can be derived from the figures above. The highest conductivity, Cases A, allow to have a stronger horizontal flux, with the consequent rise of a larger portion of the water table. Case B1, instead, having lower conductivity and the lowest flux, presents an incomplete saturation of the soil above the water table, but increasing the value of the B.C. is enough to saturate the soil. Notwithstanding, the lateral influence is much limited and most of the increase in pressure head is registered right below the trench. Finally, in case C1, having both the lowest conductivity and flux, the drainage flow does not reach the water table within 48 hours due to the very small velocities. Instead, case C2 does not reach convergence after 38 h because its conductivity is incompatible with the injection flux and generates very high overpressures.

For this reason, only cases A and B are further investigated by assessing the pressure head increase at the steady state at the end of the 48 hours. This variable can be simply interpreted as the water table rise [m] over the simulation time and is computed at every observation node. The results are reported in Figure 78; note that the curve referring to case B2 shows unrealistic values, most probably they reflect the overpressures created by the higher flux in presence of low hydraulic conductivity. On the opposite note, cases A1 and A2 are those corresponding to a larger influence on the unconfined aquifer, as they show a significant increase in pressure head until respectively 50 m and 100 m away from the edge of the trench. Case A2, being associated with the higher flux, obviously shows higher values: up to about 7 m, more than double of case A1. Case B1, instead, shows a very limited horizontal effect and, on top of this, causes a smaller rise compared to the other two, because of the lower conductivity.

	0	10	20	30	40	50	60	70	80	90	100	150	200	300	450
A1	3.17	3.12	3.00	2.80	2.48	2.08	1.65	1.26	0.93	0.68	0.49	0.05	0.01	0.00	0.00
A2	7.24	7.17	6.98	6.64	6.14	5.45	4.66	3.89	3.16	2.50	1.95	0.43	0.05	0.00	0.00
B1	1.63	1.64	1.64	1.53	1.32	0.75	0.28	0.09	0.02	0.00	0.00	0.00	0.00	0.00	0.00
B2	35.82	34.89	32.18	27.66	21.29	14.11	8.18	3.94	1.51	0.43	0.14	0.00	0.00	0.00	0.00
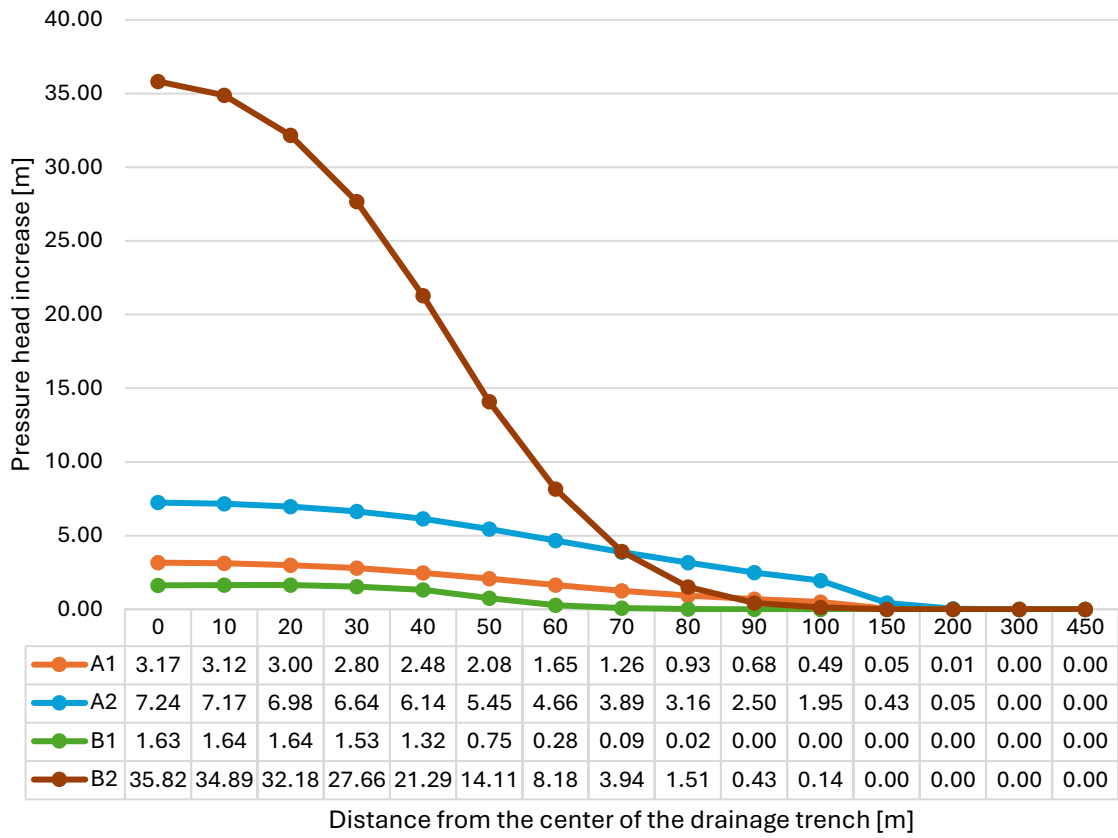
Figure 78. Injection Trench 2D - Pressure Head increase over 48h at the observation nodes.

One last 2D geometry is generated, starting from case A2. A simplified approach is used to investigate, for mere qualitative interpretation, the effect of the injection trench on a drainage infrastructure located in the surroundings. Due to the absence of the third dimension the geometry is not completely realistic and the *fontanile* is placed laterally. Indeed, the furrow with the *tubo calandra* is added at the ground level at a distance of 100 m from the edge of the injection trench. A seepage face boundary condition is applied to the furrow and to the bottom of the borehole to see whether the injection contributes to its outgoing flux, Figure 79. The variable flux boundary condition is the same as case A2, but the simulation time is extended to 4 days, to evaluate the evolution of the system after 48 hours of injection. The steady state condition is temporarily reached after the injection, but it stops later on because of the interruption of the injection flux boundary condition, The results are displayed below.

Figure 79. MAR 2D and Fontanile - Zoom on the Geometry and B.C.: no flux (red), atmospheric (green), variable flux (blue), seepage face (orange). The furrow is located at 100 m from the end of the injection trench.
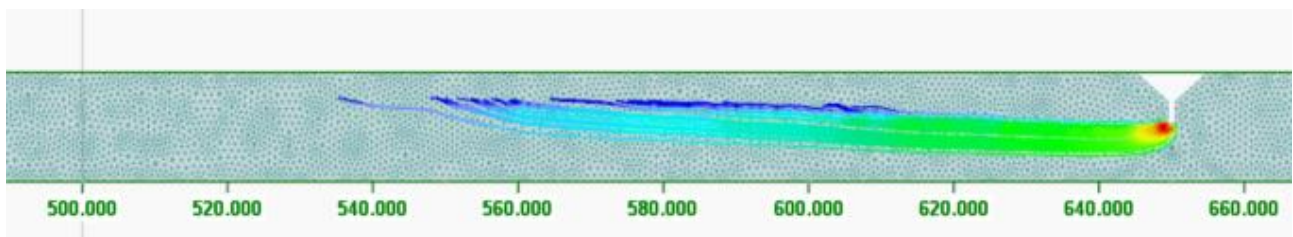
Figure 80. MAR 2D and Fontanile – Results in terms of streamlines. The furrow is located at 100 m from the end of the injection trench.

Figure 80 shows that, during the injection, the water table rises enough so that the *tubo calandra* starts affecting the streamlines and feeds the furrow. After the 48 hours, the water table deepens again and the flux is mostly horizontal, towards the *fontanile*. The same configuration but without the *tubo calandra* would require a way greater injected flux before the *fontanile* could start draining the system.

4.3.2 Injection Trench 3D

Moving to the third dimension, the screened pipe can be represented more accurately. The domain is 120 m long and represents a sandy soil interrupted by a thin layer of gravel that is going to be deposited all around the injection trench to facilitate the flow. The following Figure shows the geometry, as well as the boundary conditions, under different points of view.
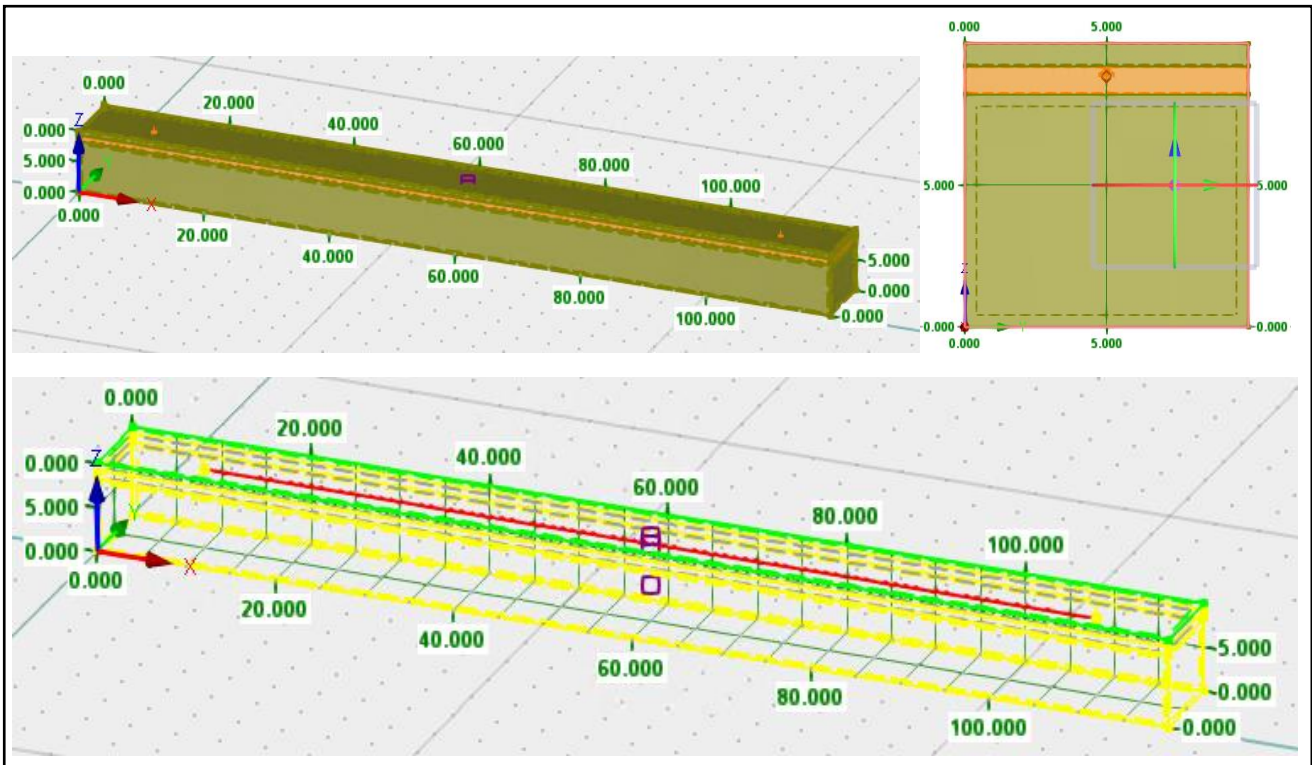
Figure 81. Injection Trench 3D - Geometry in isometric view (left) and transverse section (right); sandy soil in green and gravel in oramge. B.C. (at the bottom): no flux in yellow; atmospheric in green; variable flux in red.

The 3D mesh includes 43932 nodes and the simulation refers to the same cases, A1 to C2, as in the previous paragraph. The graphical results in terms of velocity vectors are reported below from Figure 82 to 87, note that the scale of the velocity vectors is adapted each time to facilitate the interpretation of the figures.

Intuitively, the velocities increase proportionally with the hydraulic conductivity, the magnitude of the injection flux, and with the proximity to the screened injection pipe. The direction of the vectors is initially oriented toward the bottom of the aquifer, but once the saturated area around the trench comes in contact with the water table, they tend to distribute the water around the domain, both, in the horizontal and vertical direction, causing the water table rise. The highest velocities, recorded close to the injection trench, almost double when the flux boundary condition is changed from configuration 1 to 2. As a matter of fact, with the lowest flux the maximum velocities recorded are 0.15 m/hour, 0.07 m/hour and 0.02 m/hour in cases A, B, C respectively. Instead, with the highest flux, the maxima correspond to 0.34 m/hour, 0.15 m/hour and 0.10 m/hour.
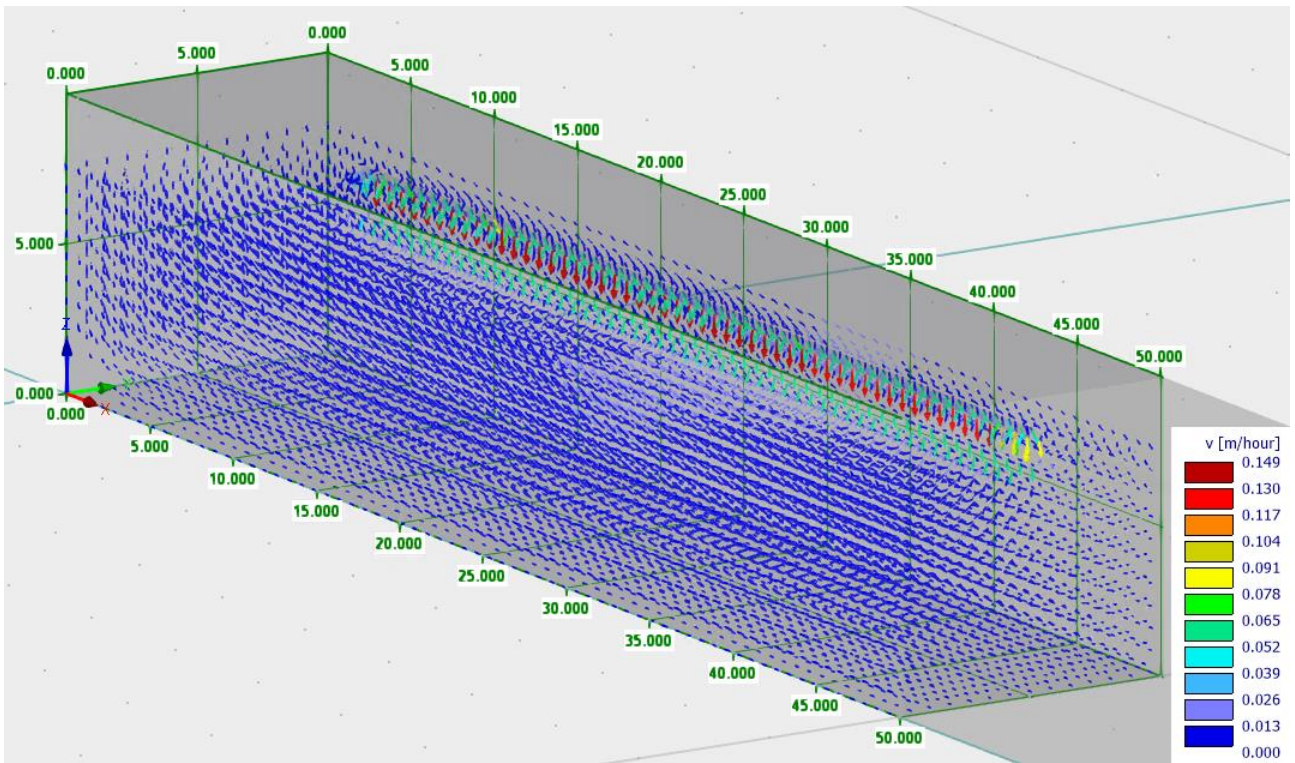
Figure 82. Injection Trench 3D - Case A1 Results (Velocity Vectors) @48h
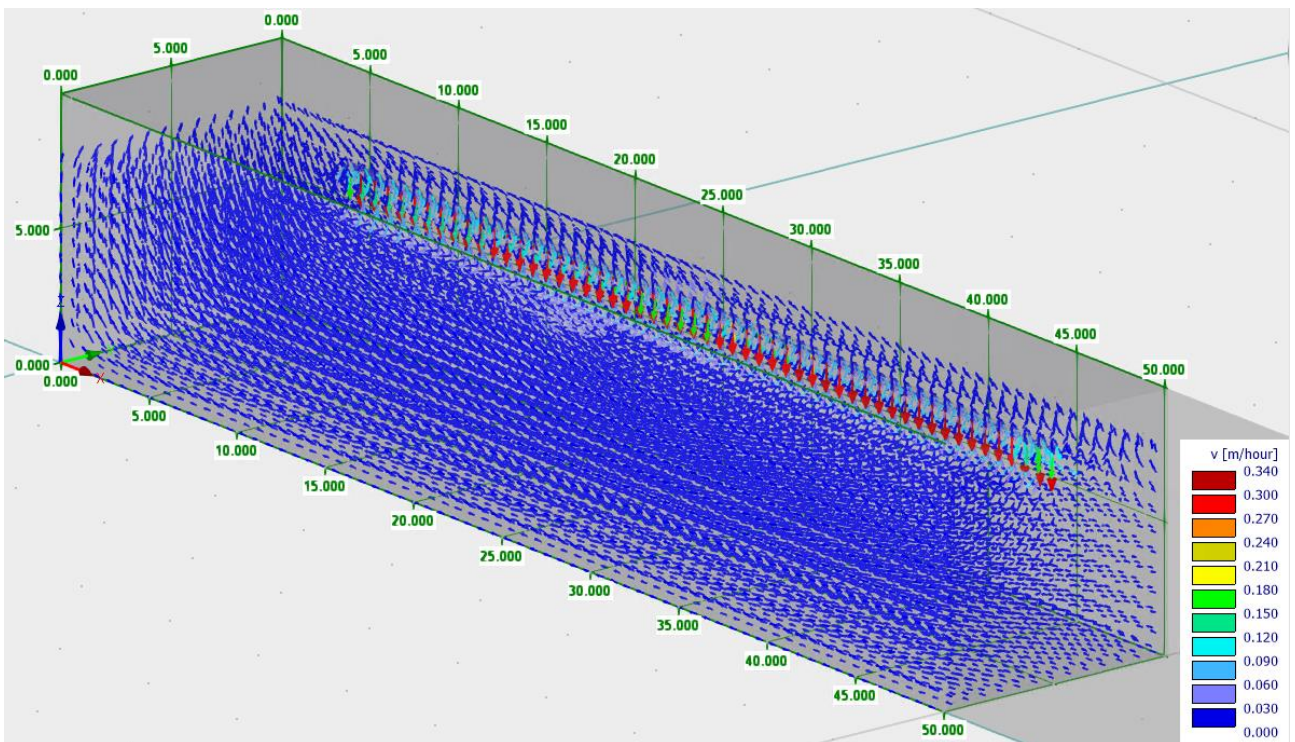
Figure 83. Injection Trench 3D - Case A2 Results (Velocity Vectors) @48h

70
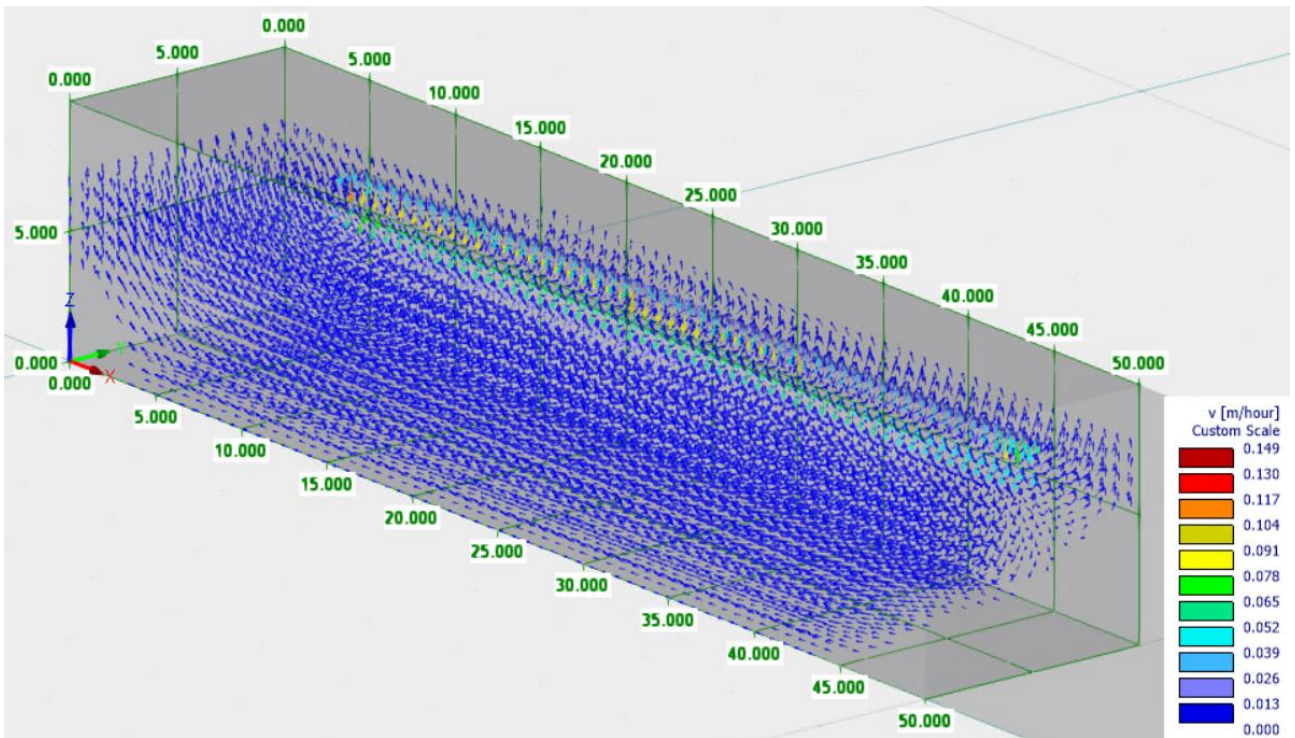
Figure 84. Injection Trench 3D - Case B1 Results (Velocity Vectors) @48h
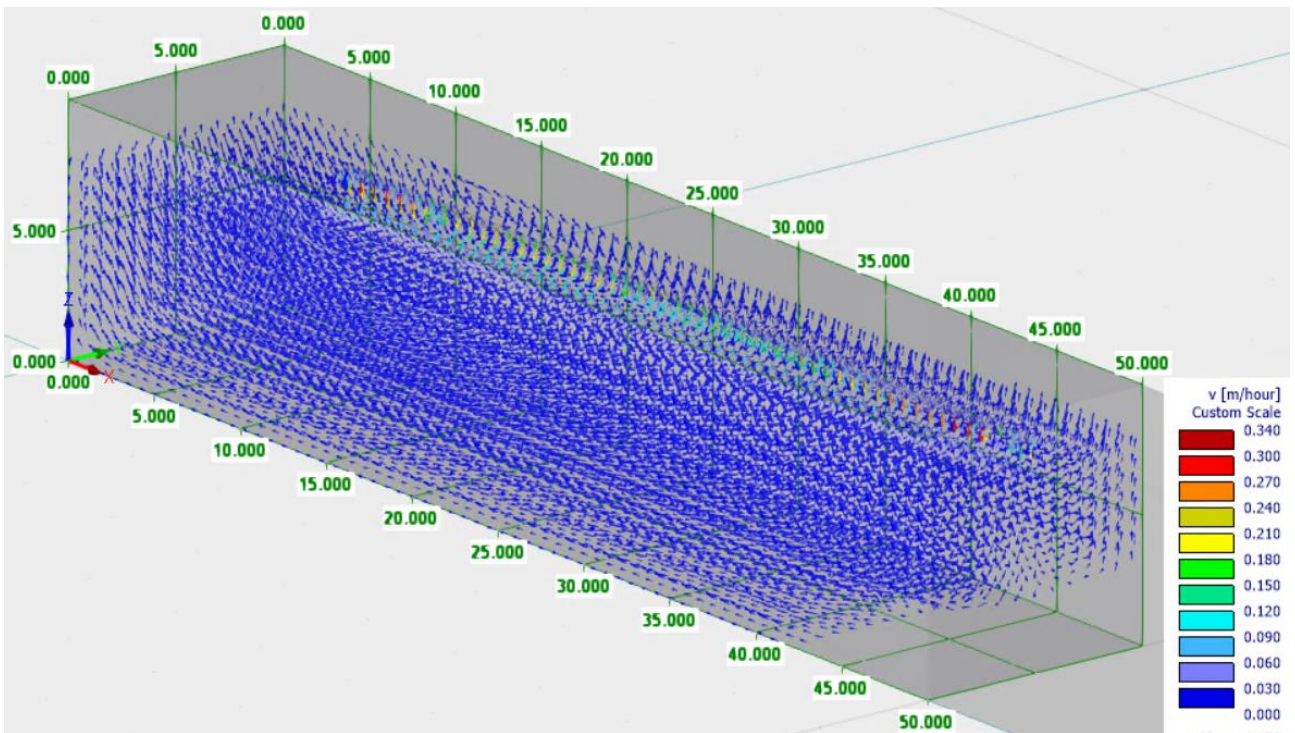
Figure 85. Injection Trench 3D - Case B2 Results (Velocity Vectors) @48h
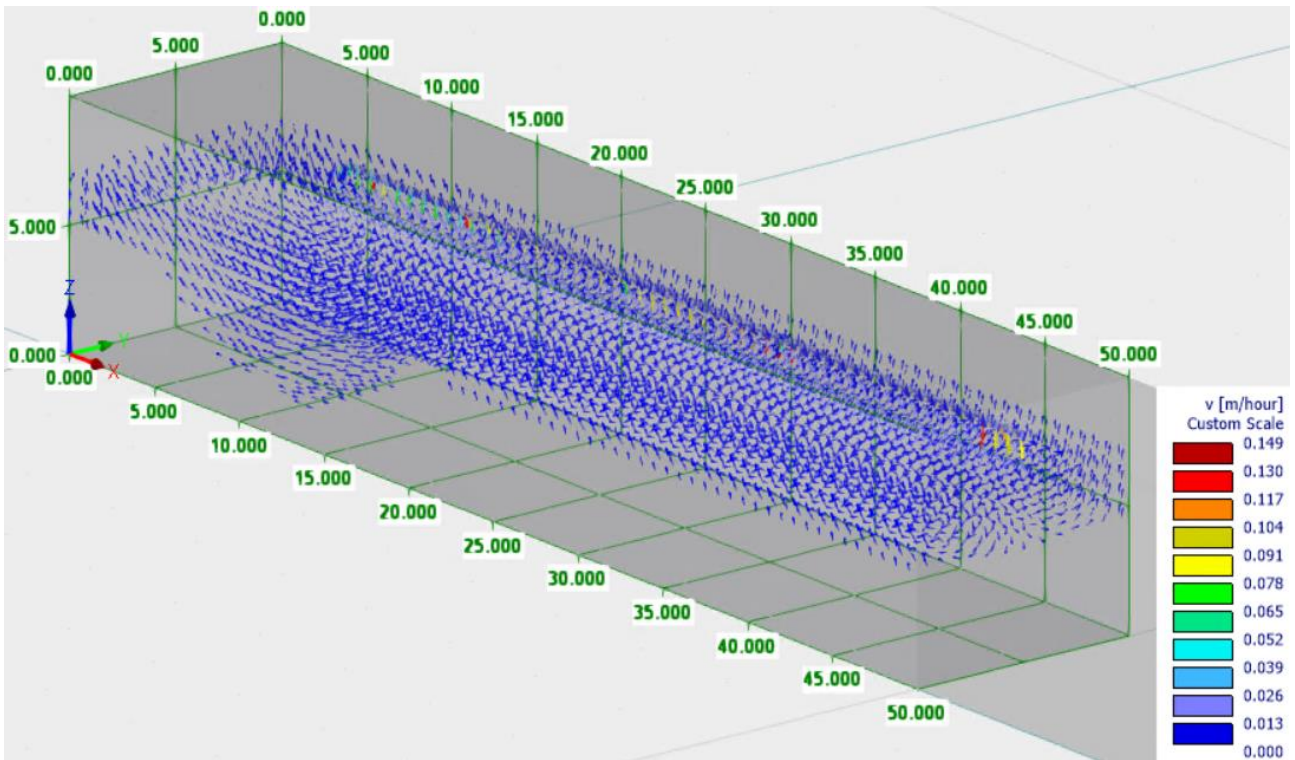
Figure 86. Injection Trench 3D - Case C1 Results (Velocity Vectors) @48h
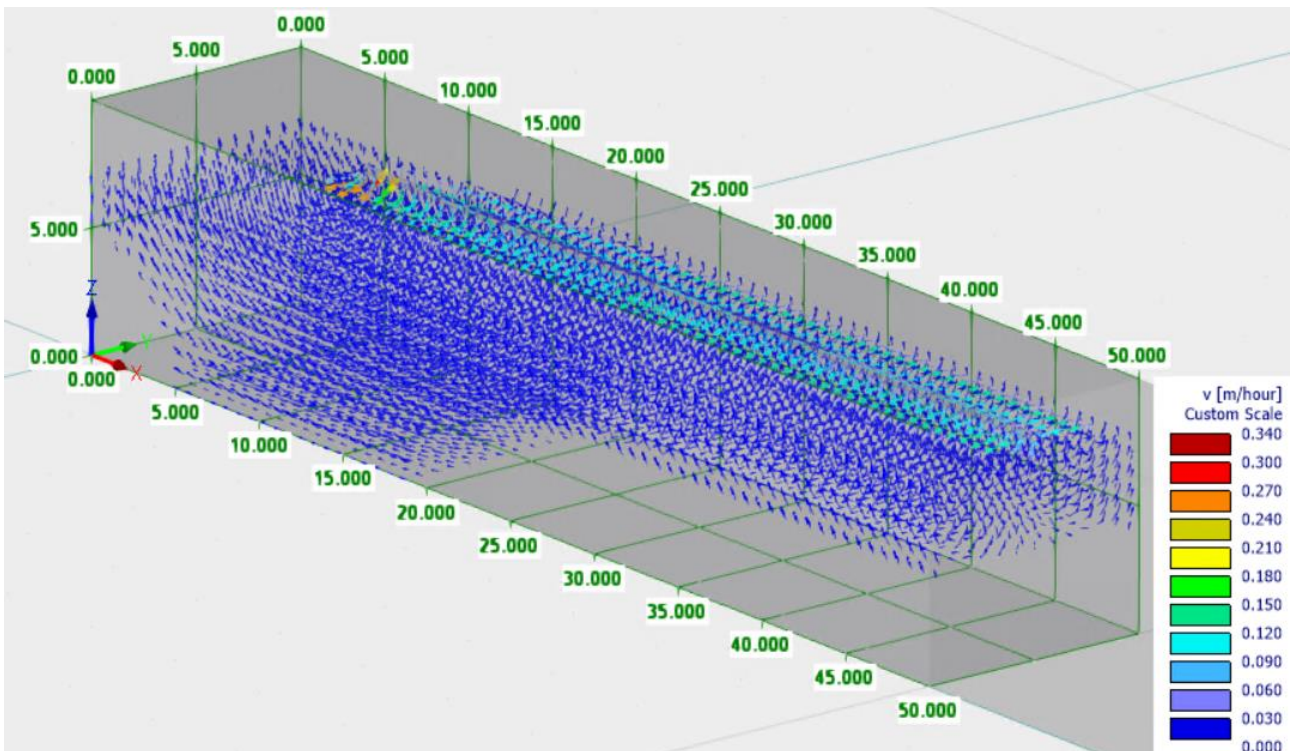
Figure 87. Injection Trench 3D - Case C2 Results (Velocity Vectors) @48h

4.4 Future development

As stated in the methodology for groundwater modelling, in order to take further the conceptual model, the next step is the detailed characterization of the site by means of field tests. For this reason, new monitoring wells are being drilled in the study area to allow the realization of multi-well aquifer tests. The perforation of a new monitoring well is presented below along with a single LeFranc Test.

The new monitoring well was excavated in the locality of Trucchi, which lies under the municipality of Morozzo (CN). Its exact location was determined starting from a pre-existing pumping well and various obstacles found on site; in particular, the distance between the two wells was set equal to 10 m as, compared to the radius of the pumping well, it is in the suitable range for multi-well tests. The drilling technique used was Direct Rotary Drilling but, since the recovery of the cores was considered particularly interesting, the use of water was restricted only to those particular moments during which the friction between the drilling bit and the soil was too high. The diameter of the drilling bit was 101 mm, whereas that of the casing was of 127 mm; their tips are made out of tungsten carbide (Figure below). During the rotation, the tips excavate the soil, which enters the drilling bit for its recovery at the surface, but if they encounter strongly resisting large clasts a jackhammer is activated to break the obstacle.

Figure 88. Drilling machine (left) and drilling bits (right) for the excavation of a new monitoring well in Trucchi (CN).

Such type of well excavation allows to perform a field test, known as LeFranc test. Its peculiarity is the possibility to discretize the soil investigation along the vertical direction. By doing so, the estimated hydraulic conductivity is expressed as a function of depth. To this test is usually associated high uncertainty due to the particular conditions it requires; for example, the test should be carried out in saturated conditions and laminar flow, which is not always the case.

Moreover, the LeFranc test can be conducted in two different configurations: falling head or constant head. In the first case one injects water in the borehole and measures the evolution of the water level in time as the water dissipates. In the second case, one monitors the discharge injected in the borehole in order to keep the water level constant. Later, starting from the measurements taken on site and with the use of Darcy Law, the hydraulic conductivity can be estimated.

In Morozzo, it was decided to perform a single LeFranc test for the range 1.5 to 3 m. More in detail, the first 1.5 m were drilled and the casing was placed. Afterwards, the next 1.5 m were drilled but the casing was not installed, in order to allow the connection to the surrounding soil. At this point, water was injected into the borehole to guarantee, locally, the saturated conditions. A few minutes later, the LeFranc test in falling head mode was immediately discarded as the velocity of the water dissipation was too high to allow a detailed monitoring of the water level. Therefore, a water pipe connected to a water meter was brought to the excavation point (Figure 89), the flow was monitored every 30 seconds and an average value of the discharge was computed.

Figure 89. LeFranc Test: the pipe at the top of the excavation ready to inject the water (left) and the water meter for the measurement of Q (right).

According to (Hvorslev, 1951), the results are interpreted by means of the following equation, where Q is the discharge [L³/T], F is a shape factor [L] equal to 2.75 times the drilled diameter and Δh is the head difference between the water in the borehole and that on the ground level.

$$Eq.\,10\; K = \frac{Q}{F * \Delta h} = \frac{23\;l/min}{2.75 * 0.127m * 3.1m} = 3.54\;10^{-4}\frac{m}{s}$$

The final excavation depth was 25 m and some of the cores collected are reported below. Finally, a granulometric analysis is being planned to investigate the material retrieved on site.

Figure 90. Cores retrieved from the drilling bit during the excavation of the new monitoring well. Every box contains 5 m of cores.

5 Conclusions

This work successfully contributed to the deeper investigation of the study area and allowed to gain an improved understanding of the current situation, as well as to sharpen the range of possibilities for adaptation solutions to the drought risk.

As a matter of fact, the assessment of the state of the groundwater in the Monregalese was fundamental to give an overview of the vulnerability of the traditional agricultural activities. The computation of the groundwater storage anomaly, through satellites measurements of gravimetry, validated with timeseries of the level of the water table, acquired by leveloggers, highlighted a strong significant decreasing trend over the area of investigation.

The numerical modelling, instead, allowed to have a clearer picture of the mechanisms controlling the discharge in the *fontanili*, both in terms of their connection directly to the water table, as well as the contribution of the *tubi calandra*. In particular, for the latter a suitable range of granulometry and conductivity of the soil was identified to maximize their performance. Having gathered all this information, the simulations of the pilot MAR site, to be located in Tetti Pesio (CN), were run under different scenarios. The results show that the highly conductive soil present on site is suitable for the construction of an injection trench, but its efficacy could be probably limited, by the infiltration capacity, to the injection of just 10^1 l/s. Moreover, the distance of a few hundreds of meters should allow a long enough storing of the resource before this resurfaces in the *fontanili* downstream.

Coming to the conclusions, the work could certainly be developed further. For instance, the computation of the groundwater storage anomaly could be enlarged to cover a wider area and the new monitoring wells, equipped with leveloggers, could provide new source of data for the validation process. Furthermore, the simulations have proved that the sensitivity of the system is high towards the parameters of the soil, especially hydraulic conductivity, therefore the need for accurate site-specific estimates rises. Indeed, the field campaigns that have just begun will surely provide more precise and reliable estimates of the hydraulic conductivity and its spatial variability around the aquifer. Consequently, a more detailed and quantitative numerical model should be created, using a dedicated software for large scale applications such as *Modflow*, to better represent the network of streams, *fontanili*, irrigation channels and new pilot MAR sites, as well as their effects on the seasonal availability of, both, surface and groundwater.

6 References

Alam, S., Borthakur, A., Ravi, S., Gebremichael, M., & Mohanty, S. K. (2021). Managed aquifer recharge implementation criteria to achieve water sustainability. *Science of the Total Environment*, *768*, 144992. https://doi.org/10.1016/j.scitotenv.2021.144992

Amendola, A. (2022). *Lo Studio dei Poli Terrestri attraverso Metodi Geofisici*. Politecnico di Torino.

Ansaldi, G., & Maffeo, B. (1979). *Quaderno 26 - Carta idrogeologica provincia Cuneo*.

Arpa Piemonte. (2023). *Il 2022 è stato caldo e secco dal principio alla fine*. https://www.arpa.piemonte.it/notizia/2022-stato-caldo-secco-dal-principio-alla-fine#:~:text=L'anno 2022 si era,il primo giorno dell'anno.

Cantoni, È., Revilla-romero, B., Paltán, H., Rodriguez, D. J., & Paganini, M. (2024). Building Drought Resilience : Earth Observation for Groundwater Management in Botswana. *EGU*, *May 2024*.

Civita, M. V., Vigna, B., De Maio, M., Fiorucci, A., Pizzo, S., Gandolfo, M., Banzato, C., Menegatti, S., Offi, M., & Moitre, B. (2011). *Le acque sotterranee della Pianura e della Collina Cuneese*.

Cooley, S. S., & Landerer, F. W. (2020). Gravity Recovery and Climate Follow-on (GRACE-FO), Experiment Level-3 Data Product User Handbook. *Jet Propulsion Laboratory,California Institute of Technology*, 1–58.

Daqiq, M. T., Sharma, R., Karunakalage, A., & Kannaujiya, S. (2023). Determination of Groundwater Storage Variation, Deficit, and Abstraction in Afghanistan and the Assessment of the Evolution of Vadose Zone in Kabul City. *IEEE Transactions on Geoscience and Remote Sensing*, *61*, 1–18. https://doi.org/10.1109/TGRS.2023.3326164

De Luca, D. A., Ghione, R., & Lasagna, M. (2005). Studio idrogeologico dei Fontanili della Pianura Piemontese. *Giornale Di Geologia Applicata*, *2*.

EEA. (2017). *Annual average water stress indicator WEI on river basin level for baseline and 2050 period with SCENES scenario Economy First (EcF)*. https://www.eea.europa.eu/data-and-maps/figures/precipitation-deficit-in-summer-jja-1

EEA. (2023). *Water scarcity conditions in Europe (Water exploitation index plus)*. https://www.eea.europa.eu/en/analysis/indicators/use-of-freshwater-resources-in-europe-1?activeAccordion=546a7c35-9188-4d23-94ee-005d97c26f2b

EO Portal. (2013). *GRACE-FO (Gravity Recovery And Climate Experiment - Follow-On)*. https://www.eoportal.org/satellite-missions/grace-fo#the-gravity-of-water

ESA. (2020). *Introducing the Newest ESA Third Party Missions*. https://earth.esa.int/eogateway/news/introducing-the-newest-esa-third-party-missions

FAO, Brouwer, C., Prins, K., Kay, M., & Heibloem, M. (1990). *Irrigation water management : irrigation methods, training manual*. 5, 140. http://www.fao.org/docrep/s8684e/s8684e00.HTM

GEAM. (2000). *Le risorse idriche sotterranee del territorio cuneese* (pp. 225–242). CNR-GNDCI.

Han, Z., Huang, S., Huang, Q., Leng, G., Liu, Y., Bai, Q., He, P., Liang, H., & Shi, W. (2021). GRACE-based high-resolution propagation threshold from meteorological to groundwater drought. *Agricultural and Forest Meteorology*, *307*(January), 108476. https://doi.org/10.1016/j.agrformet.2021.108476

Hussain, D., Khan, A. A., Hassan, S. N. U., Naqvi, S. A. A., & Jamil, A. (2021). A time series assessment of terrestrial water storage and its relationship with hydro-meteorological factors in Gilgit-Baltistan region using GRACE observation and GLDAS-Noah model. *SN Applied Sciences*, *3*(5), 1–11. https://doi.org/10.1007/s42452-021-04525-4

Hvorslev, M. J. (1951). Time Lag and Soil Permeability in Ground-Water Observations. *Bulletin n. 36*, *36*, 53.

ISPRA, Braca, G., Lastoria, B., Mariani, S., Piva, F., & Tropeano, R. (2023). *WATER EXPLOITATION INDEX PLUS*. https://indicatoriambientali.isprambiente.it/it/risorse-idriche-e-bilancio/wei-water-exploitation-index-plus

Lasagna, M., Mancini, S., & De Luca, D. A. (2020). Groundwater hydrodynamic behaviours based on water table levels to identify natural and anthropic controlling factors in the Piedmont Plain (Italy). *Science of the Total Environment*, *716*, 137051. https://doi.org/10.1016/j.scitotenv.2020.137051

Lin, H., Cheng, X., Zheng, L., Peng, X., Feng, W., & Peng, F. (2022). Recent Changes in Groundwater and Surface Water in Large Pan-Arctic River Basins. *Remote Sensing*, *14*(3). https://doi.org/10.3390/rs14030607

NASA. (2020). *High Spatial and Temporal Resolution Continental Water Mass Anomaly Fields from GRACE*. https://www.earthdata.nasa.gov/esds/competitive-programs/access/grace

NASA JPL | Podaac. (2017). *Gravity Recovery and Climate Experiment (GRACE)*. https://podaac.jpl.nasa.gov/grace

Rui, H. L., & Beaudoing, H. (2020). README Document for NASA GLDAS Version 2 Data Products. *Goddard Earth Sciences Data and Information Services Center (GES DISC)*, *16*(1), 1–32. https://hydro1.gesdisc.eosdis.nasa.gov/data/GLDAS/README_GLDAS2.pdf

Rzepecka, Z., & Birylo, M. (2020). Groundwater storage changes derived from GRACE and GLDAS on smaller river basins—a case study in Poland. *Geosciences (Switzerland)*, *10*(4). https://doi.org/10.3390/geosciences10040124

Scanlon, B. R., Fakhreddine, S., Rateb, A., de Graaf, I., Famiglietti, J., Gleeson, T., Grafton, R. Q., Jobbagy, E., Kebede, S., Kolusu, S. R., Konikow, L. F., Long, D., Mekonnen, M., Schmied, H. M., Mukherjee, A., MacDonald, A., Reedy, R. C., Shamsudduha, M., Simmons, C. T., … Zheng, C. (2023). Global water resources and the role of groundwater in a resilient water future. *Nature Reviews Earth and Environment*, *4*(2), 87–101. https://doi.org/10.1038/s43017-022-00378-6

Segobye, M., Motlogelwa, L. K., Nkwae, B., Ouma, Y. O., Maphale, L., & Manisa, B. M. (2023). Comparison of GRACE Gravity Anomaly Solutions for Terrestrial Water Storage Variability in Arid and Semi-arid Botswana. *South African Journal of Geomatics*, *12*(1), 56–72.

https://doi.org/10.4314/sajg.v12i1.4

SeTe: Siccità e Territorio. (n.d.). 2021. Retrieved August 21, 2024, from https://www.interreg-alcotra.eu/it/sete-siccita-e-territorio

Sethi, R., & Di Molfetta, A. (2019). Mechanisms of Contaminant Transport in Aquifers. In *Springer Tracts in Civil Engineering*. https://doi.org/10.1007/978-3-030-20516-4_10

Šimůnek, J., & Šejna, M. (2022). *HYDRUS 2D/3D v.5 Technical Manual II*.

Thomas, B. F., & Famiglietti, J. S. (2019). Identifying Climate-Induced Groundwater Depletion in GRACE Observations. *Scientific Reports*, *9*(1), 1–9. https://doi.org/10.1038/s41598-019-40155-y

UN-Water. (2013). What is Water Security? *UN Publications*, *October 2013*. http://www.unwater.org/publications/water-security-infographic/

UNESCO, & Koncagül, Engin , Connor, Richard , Abete, V. (2024). The United Nations World Water Development Report 2024 Executive Summary. *UNESCO World Water Assessment Programme*.

van Genuchten, M. T. (1980). A Closed-form Equation for Predicting the Hydraulic Conductivity of Unsaturated Soils. In *Soil Science Society of America Journal* (Vol. 44, Issue 5, pp. 892–898). https://doi.org/10.2136/sssaj1980.03615995004400050002x

Water Framework Directive (WFD) 2000/60/EC. (2000).

WISE. (2024). *Water resources of Europe*. https://water.europa.eu/freshwater/europe-freshwater/freshwater-themes/water-resources-europe#:~:text=In Europe%2C most water is,%25) and households (10%25).

Xanke, J., & Liesch, T. (2022). Quantification and possible causes of declining groundwater resources in the Euro-Mediterranean region from 2003 to 2020. *Hydrogeology Journal*, *30*(2), 379–400. https://doi.org/10.1007/s10040-021-02448-3

IPCC - Caretta, M.A., A. Mukherji, M. Arfanuzzaman, R.A. Betts, A. Gelfan, Y. Hirabayashi, T.K. Lissner, J. Liu, E. Lopez Gunn, R. Morgan, S. Mwanga, and S. Supratid, 2022: Water. In: Climate Change 2022: Impacts, Adaptation and Vulnerability. Contribution of Working Group II to the Sixth Assessment Report of the Intergovernmental Panel on Climate Change [H.-O. Pörtner, D.C. Roberts, M. Tignor, E.S. Poloczanska, K. Mintenbeck, A. Alegría, M. Craig, S. Langsdorf, S. Löschke, V. Möller, A. Okem, B. Rama (eds.)]. Cambridge University Press, Cambridge, UK and New York, NY, USA, pp. 551–712, doi:10.1017/9781009325844.006.

DATA SOURCES:

1) GRECE WET @1°resolution.
   Available at :https://grace.jpl.nasa.gov/data/data-analysis-tool/
2) GRACE/GRACE-FO: NASA | PODAAC - JPL GRACE and GRACE-FO Mascon Ocean, Ice, and Hydrology Equivalent Water Height Coastal Resolution Improvement (CRI) Filtered Release 06.1 Version 03. (TELLUS_GRAC-GRFO_MASCON_CRI_GRID_RL06.1_V3).
   Available at: https://podaac.jpl.nasa.gov/dataset/TELLUS_GRAC-GRFO_MASCON_CRI_GRID_RL06.1_V3
3) GLDAS-2.2: Global Land Data Assimilation System. Available at: https://developers.google.com/earth-engine/datasets/catalog/NASA_GLDAS_V022_CLSM_G025_DA1D